



# Differential Ultra-Wideband Microwave Imaging for Medical Applications

Dissertation

zur Erlangung des akademischen Grades

Doktor-Ingenieur  
(Dr.-Ing.)

vorgelegt der  
Fakultät für Informatik und Automatisierung der  
Technischen Universität Ilmenau

von  
Dipl.-Ing. Sebastian Ley

Gutachter: 1. Prof. Dr.-Ing. habil. Peter Husar  
2. Prof. Dr.-Ing. Silvio Dutz (JP)  
3. apl. Prof. Dr. rer. biol. hum. Ingrid Hilger

Datum der Einreichung: 19.04.2022  
Datum der wissenschaftlichen Aussprache: 11.11.2022

DOI: 10.22032/dbt.55224  
URN: urn:nbn:de:gbv:ilm1-2022000494

Auch eine Reise von tausend Meilen muss mit einem einzigen Schritt beginnen.

*Laotse*

# Acknowledgments - Danksagung

Die vorliegende Arbeit entstand im Rahmen meiner Tätigkeit als wissenschaftlicher Mitarbeiter am Institut für Biomedizinische Technik und Informatik im Fachgebiet Biosignalverarbeitung. An dieser Stelle möchte ich all jenen danken, die mich in dieser Zeit begleitet und zur Fertigstellung dieser Arbeit beigetragen haben.

Ich danke Prof. Dr.-Ing. habil. Peter Husar für die wissenschaftliche Betreuung dieser Arbeit, die langjährige Unterstützung sowie das stets entgegengebrachte Vertrauen.

Großer Dank gebührt meinem Mentor Dr.-Ing. Marko Helbig für die kompetente fachliche Betreuung sowie insbesondere auch die persönliche Begleitung und das außerordentliche Engagement seit Beginn meiner wissenschaftlichen Tätigkeit im Bereich der Mikrowellensensorik. Diese Arbeit würde ohne die vielen konstruktiven Diskussionen, wertvollen Hinweise und Denkanstöße in dieser Form nicht existieren.

Ich möchte Dr.-Ing. Jürgen Sachs für die hilfreichen Anregungen und Ratschläge im Rahmen der gemeinsamen Forschungstätigkeit herzlich danken. Dr.-Ing. Marc Schalles danke ich für die Mühe und die Zeit, die er beim Korrekturlesen investiert hat.

Weiterhin bin ich allen Kollegen und Kolleginnen am Institut für die angenehme Zusammenarbeit, die vielen guten Gespräche auch über die Arbeitszeit hinaus sowie die Hilfsbereitschaft sehr verbunden.

Nicht zuletzt danke ich meiner Familie und meinen Freunden für ihr Verständnis und ihre Ermutigung. Vor allem danke ich meinen Eltern für ihren Rückhalt und ihre ständige Unterstützung. Dies hat mir den Weg zur Promotion erst ermöglicht und mich trotz schwieriger Phasen nicht davon abbringen lassen. Ein ganz besonderer Dank gilt meiner Frau Sabrina für das fleißige Korrekturlesen während meiner gesamten wissenschaftlichen Tätigkeit, ihrem moralischen Beistand und die unermüdliche Unterstützung, um diese Dissertation zum Abschluss zu bringen.

# Abstract

Electromagnetic ultra-wideband sensing and imaging provide promising perspectives in various biomedical applications as these waves can penetrate biological tissue. The use of low-power and nonionizing electromagnetic waves in the microwave frequency range offers an examination method that is harmless to health. One of the challenges in the field of ultra-wideband microwave sensor technology is the extraction of diagnostically relevant information from the measurement data, since the complex wave propagation in tissue usually requires computationally intensive methods. This problem is simplified when the scattering properties of the object under observation change with time. Such a time variance of the scattering properties can be exploited by means of a differential measurement over a certain time interval. In this work, a differential approach using ultra-wideband sensing is considered for two medical applications. The measurement systems used in this work are based on the M-sequence technology developed at the Technische Universität Ilmenau.

The first application relates to noninvasive temperature monitoring using ultra-wideband technology during hyperthermia treatment. Hyperthermia is a thermal therapy to support oncological treatments (e.g. chemotherapy or radiotherapy). During such a treatment, the tumor tissue is heated by 4 °C to 8 °C, whereby it is important that the temperature does not exceed the upper limit of 45 °C. In this context, differential ultra-wideband monitoring offers a promising technique for continuous and noninvasive temperature monitoring inside the body. The approach is based on the temperature-dependent dielectric properties of biological tissue. In this method, low power electromagnetic waves are emitted into the medium under investigation. These waves propagate according to the dielectric properties of tissue. If a target region (e.g. tumor) is heated, its dielectric properties will change, which leads to a changing scattering behavior of the electromagnetic wave. These changes can be detected in the measured reflection signals using ultra-wideband microwave technology. To evaluate the measured changes in the radar signal, it is necessary to know the temperature-dependent dielectric properties of tissue in the microwave frequency range.

Due to the lack of knowledge of temperature-dependent dielectric properties of tissues over a wide microwave frequency range, the dielectric properties for liver, muscle, fat and



---

blood in the temperature range between 30 °C and 50 °C from 500 MHz to 7 GHz are acquired in this work. For this purpose, a measurement setup for the temperature-dependent dielectric spectroscopy of tissue, tissue substitutes and fluids is presented. Furthermore, the main influences on measuring the temperature-dependent dielectric properties are analyzed. The measured data are modeled using a temperature-dependent Cole-Cole model in order to calculate the dielectric properties for arbitrary values in the investigated temperature and frequency range. In a further experiment, the noninvasive detection of temperature changes using ultra-wideband microwave technology is demonstrated in an experimental measurement setup. The results show that a temperature change of 1 °C results in differential signals that are detectable by means of ultra-wideband pseudo-noise sensing (M-sequence).

The second application is dealing with contrast enhanced microwave breast cancer imaging. Due to the physiologically given low dielectric contrast between glandular and tumor tissue, the use of contrast agents, specifically magnetic nanoparticles, can improve the diagnostic reliability. The approach is based on the assumption that functionalized magnetic nanoparticles are able to selectively accumulate in tumor tissue after intravenous administration. Provided that a sufficient amount of nanoparticles has accumulated in the tumor, they can be modulated by an external polarizing magnetic field. Due to the modulation, the scattering behavior of the magnetic nanoparticles changes, which results a changing backscattering behavior. This change can be detected using low-power electromagnetic waves.

In this work, the detectability and imaging of magnetic nanoparticles by means of ultra-wideband pseudo-noise sensing in the microwave frequency range is considered with respect to breast cancer detection. First, various influencing factors on the detectability of the magnetic nanoparticles are investigated, such as the mass of the magnetic nanoparticles, the magnetic field strength of the external polarizing magnetic field and the viscosity of the surrounding medium in which the nanoparticles are embedded. The results reveal a linear dependence between the measured radar signal and the mass of the magnetic nanoparticles as well as a nonlinear relationship between the response signal of the magnetic nanoparticles and the magnetic field intensity of the external magnetic field. Furthermore, the magnetic nanoparticles can be successfully detected in all investigated viscosities of the surrounding medium. Based on these preliminary investigations, a realistic measurement setup for contrast enhanced microwave breast cancer imaging is presented. The evaluation of the measurement setup is performed by phantom measurements, where the used phantom materials mimic the dielectric properties of biological tissue to obtain significance of the results with respect to a practical measurement scenario. In this context,

---

the detectability and imaging of the magnetic nanoparticles are analyzed depending on the tumor position and penetration depth, respectively. The results show that the magnetic nanoparticles can be successfully detected. However, the magnetic poles of the electromagnet limit the space for the transmitting and receiving antennas, resulting in an inhomogeneous microwave illumination of the medium under test, which leads to a location-dependent magnetic nanoparticle response. Furthermore, the intensity of the response signal caused by the magnetic nanoparticles in the three-dimensional image depends on their position due to the path-dependent attenuation and the inhomogeneous magnetic field within the investigated medium. Regarding the last point, the external polarizing magnetic field is measured in the investigation area and an approach to compensate for the inhomogeneity of the magnetic field is presented. In addition, the disturbing influences of the polarizing magnetic field on the measurement setup are analyzed. In this context, two different modulation types (a two-state and a periodic modulation) of the external polarizing magnetic field are investigated. It is shown that both modulations can be used to image the magnetic nanoparticles. Finally, the results are discussed with respect to the spurious effects as well as a practical application scenario.

# Zusammenfassung

Elektromagnetische Ultrabreitband-Sensorik und -Bildgebung bieten vielversprechende Perspektiven für verschiedene biomedizinische Anwendungen, da diese Wellen biologisches Gewebe durchdringen können. Dabei stellt der Einsatz von leistungsarmen und nichtionisierenden Mikrowellen eine gesundheitlich unbedenkliche Untersuchungsmethode dar. Eine der Herausforderungen im Bereich der ultrabreitbandigen Mikrowellensensorik ist dabei die Extraktion der diagnostisch relevanten Informationen aus den Messdaten, da aufgrund der komplexen Wellenausbreitung im Gewebe meist rechenaufwändige Methoden notwendig sind. Dieses Problem wird wesentlich vereinfacht, wenn sich die Streueigenschaften des zu untersuchenden Objektes zeitlich ändern. Diese zeitliche Varianz der Streueigenschaften kann mit Hilfe einer Differenzmessung über ein bestimmtes Zeitintervall ausgenutzt werden. Im Rahmen dieser Arbeit wird der differentielle Ansatz mittels Ultrabreitband-Sensorik für zwei medizinische Anwendungsszenarien betrachtet. Die dabei genutzten Messsysteme basieren auf dem M-Sequenzverfahren, welches an der Technischen Universität Ilmenau entwickelt wurde.

Die erste Anwendung bezieht sich auf das nicht-invasive Temperaturmonitoring mittels Ultrabreitband-Technologie während einer Hyperthermiebehandlung. Hyperthermie ist eine Wärmetherapie zur Unterstützung onkologischer Behandlungen (z. B. Chemo- oder Strahlentherapie). Während einer solchen Behandlung wird das Tumorgewebe um 4 °C bis 8 °C erhöht. Dabei ist es wichtig, dass die Temperatur die obere Grenze von 45 °C nicht überschreitet. In diesem Zusammenhang bietet das differentielle Ultrabreitband-Monitoring eine vielversprechende Technik zur kontinuierlichen und nicht-invasiven Messung der Temperatur im Körperinneren. Der Ansatz basiert auf den temperaturabhängigen dielektrischen Eigenschaften von biologischem Gewebe. Dabei werden elektromagnetische Wellen mit einer geringen Leistung in das Untersuchungsmedium eingebracht, die sich gemäß den dielektrischen Eigenschaften von Gewebe ausbreiten. Wird eine Zielregion (bspw. Tumor) erwärmt, so ändern sich dessen dielektrische Eigenschaften, was zu einem sich ändernden Streuverhalten der elektromagnetischen Welle führt. Diese Änderungen können mittels Ultrabreitband-Sensorik erfasst werden. Für die Evaluierung der gemessenen Änderungen im Radarsignal ist es notwendig, die temperaturabhängigen dielektrischen Eigenschaften von Gewebe im Mikrowellenfrequenzbereich zu kennen.

---

Aufgrund der wenigen in der Literatur vorhandenen temperaturabhängigen dielektrischen Eigenschaften von Gewebe über einen breiten Mikrowellenfrequenzbereich werden in dieser Arbeit die dielektrischen Eigenschaften für Leber, Muskel, Fett und Blut im Temperaturbereich zwischen 30 °C und 50 °C von 500 MHz bis 7 GHz erfasst. Hierzu wird zunächst ein Messaufbau für die temperaturabhängige dielektrische Spektroskopie von Gewebe, Gewebeersatz und Flüssigkeiten vorgestellt und die wesentlichen Einflussfaktoren auf die Messungen analysiert. Die Messdaten werden mit Hilfe eines temperaturabhängigen Cole-Cole Models modelliert, um die dielektrischen Eigenschaften für beliebige Werte im untersuchten Temperatur- und Frequenzbereich berechnen zu können. In einem weiteren Experiment wird die nicht-invasive Erfassung von Temperaturänderungen mittels Ultrabreitband-Technologie in einem experimentellen Messaufbau nachgewiesen. Die Ergebnisse zeigen, dass eine Temperaturänderung von 1 °C zu Differenzsignalen führt, welche mit der genutzten Ultrabreitband-Sensorik (M-Sequenz) detektierbar sind.

Die zweite Anwendung befasst sich mit der kontrastbasierten Mikrowellen-Brustkrebsbildgebung. Aufgrund des physiologisch gegebenen geringen dielektrischen Kontrastes zwischen Drüsen- und Tumorgewebe kann durch den Einsatz von Kontrastmitteln, im Speziellen magnetischen Nanopartikeln, die Zuverlässigkeit einer Diagnose verbessert werden. Der Ansatz beruht darauf, dass funktionalisierte magnetische Nanopartikel in der Lage sind, sich selektiv im Tumorgewebe zu akkumulieren, nachdem diese intravenös verabreicht wurden. Unter der Bedingung, dass sich eine ausreichende Menge der Nanopartikel im Tumor angesammelt hat, können diese durch ein äußeres polarisierendes Magnetfeld moduliert werden. Aufgrund der Modulation ändert sich das Streuverhalten der magnetischen Nanopartikel, was wiederum zu einem sich ändernden Rückstreuverhalten führt. Diese Änderungen können mittels leistungsarmen elektromagnetischen Wellen detektiert werden.

In dieser Arbeit wird die Detektierbarkeit und Bildgebung von magnetischen Nanopartikeln mittels Ultrabreitband-Sensorik im Mikrowellenfrequenzbereich in Hinblick auf die Brustkrebsdetektion betrachtet. Dabei werden zunächst verschiedene Einflussfaktoren, wie die Abhängigkeit der Masse der magnetischen Nanopartikel, die Magnetfeldstärke des äußeren Magnetfeldes sowie die Viskosität des Umgebungsmediums, in das die Nanopartikel eingebettet sind, auf die Detektierbarkeit der magnetischen Nanopartikel untersucht. Die Ergebnisse zeigen eine lineare Abhängigkeit zwischen dem gemessenen Radarsignal und der Masse der magnetischen Nanopartikel sowie einen nichtlinearen Zusammenhang zwischen der Antwort der magnetischen Nanopartikel und der Feldstärke des äußeren Magnetfeldes. Darüber hinaus konnten die magnetischen Nanopartikel für alle untersuchten Viskositäten erfolgreich detektiert werden. Basierend auf diesen Voruntersuchungen wird

---

ein realistischer Messaufbau für die kontrastbasierte Brustkrebsbildgebung vorgestellt. Die Evaluierung des Messaufbaus erfolgt mittels Phantommessungen, wobei die verwendeten Phantommaterialien die dielektrischen Eigenschaften von biologischem Gewebe imitieren, um eine möglichst hohe Aussagekraft der Ergebnisse hinsichtlich eines praktischen Messszenarios zu erhalten. Dabei wird die Detektierbarkeit und Bildgebung der magnetischen Nanopartikel in Abhängigkeit der Tumortiefe analysiert. Die Ergebnisse zeigen, dass die magnetischen Nanopartikel erfolgreich detektiert werden können. Dabei hängt im dreidimensionalen Bild die Intensität des Messsignals, hervorgerufen durch die magnetischen Nanopartikel, von deren Position ab. Die Ursachen hierfür sind die pfadabhängige Dämpfung der elektromagnetischen Wellen, die inhomogene Ausleuchtung des Mediums mittels Mikrowellen, da eine gleichmäßige Anordnung der Antennen aufgrund der Magnetpole des Elektromagneten nicht möglich ist, sowie das inhomogene polarisierende Magnetfeld innerhalb des Untersuchungsmediums. In Bezug auf den letzten Aspekt wird das Magnetfeld im Untersuchungsbereich ausgemessen und ein Ansatz präsentiert, mit dem die Inhomogenität des Magnetfeldes kompensiert werden kann. Weiterhin wurden die Störeinflüsse des polarisierenden Magnetfeldes auf das Messsystem untersucht. In diesem Zusammenhang werden zwei verschiedene Modulationsarten (eine Modulation mit den zwei Zuständen AN/AUS und eine periodische Modulation) des äußeren polarisierenden Magnetfeldes analysiert. Es wird gezeigt, dass mit beiden Modulationen die magnetischen Nanopartikel bildgebend dargestellt werden können. Abschließend werden die Ergebnisse in Hinblick auf die Störeinflüsse sowie ein praktisches Anwendungsszenario diskutiert.

# Table of Contents

<b>1</b>	<b>Introduction</b>	<b>1</b>
1.1	Motivation and Background . . . . .	1
1.2	Structure and Contribution of the Thesis . . . . .	3
<b>2</b>	<b>Basics</b>	<b>5</b>
2.1	Ultra-Wideband Technology . . . . .	5
2.2	UWB M-sequence Network Analyzer . . . . .	7
2.3	Differential Ultra-Wideband Microwave Imaging . . . . .	10
2.4	Dielectric Permittivity of Biological Tissue in the Microwave Frequency Range	13
2.5	Magnetic Susceptibility of MNPs in the Microwave Frequency Range . . . .	16
<b>3</b>	<b>State of the Art</b>	<b>21</b>
3.1	Temperature Monitoring during Thermal Treatment . . . . .	21
3.2	Magnetic Nanoparticles in Medical Applications . . . . .	24
<b>4</b>	<b>UWB Microwave Temperature Monitoring</b>	<b>26</b>
4.1	UWB Temperature-Dependent Dielectric Spectroscopy of Porcine Tissue and Blood . . . . .	27
4.1.1	Measurement Setup . . . . .	27
4.1.2	Influences on the Acquisition of Temperature-Dependent Dielectric Properties . . . . .	29
4.1.3	Temperature-Dependent Cole-Cole Model . . . . .	36
4.1.4	Results of Temperature-Dependent Dielectric Spectroscopy . . . . .	38
4.2	Noninvasive Detection of Temperature Changes by Means of UWB Mi- crowave Radar . . . . .	47
4.3	Discussion . . . . .	51
<b>5</b>	<b>MNP Detection and Imaging by Means of UWB Microwave Sensing</b>	<b>55</b>
5.1	Influence of the Magnetic Permeability on the UWB Signal . . . . .	56
5.2	Clutter Removal and Signal Processing . . . . .	60
5.3	Influences on the Detectability of MNPs . . . . .	62
5.3.1	Mass Dependency of the MNPs . . . . .	63

5.3.2	Influence of the Viscosity of the Target and the Magnetic Field Intensity of an External PMF on the MNP Response . . . . .	65
5.4	MNP Imaging . . . . .	68
5.4.1	Measurement Setup . . . . .	69
5.4.2	MNP Imaging via DAS-Beamforming . . . . .	71
5.4.3	MNP Imaging Depending on the Target Position and the Penetration Depth . . . . .	72
5.4.4	Magnetic Field Influence . . . . .	75
5.4.5	MNP Imaging Depending on the PMF Modulation . . . . .	77
5.5	Discussion . . . . .	79
<b>6</b>	<b>Summary</b>	<b>85</b>
	<b>Bibliography</b>	<b>xiv</b>
	<b>List of Figures</b>	<b>xvii</b>
	<b>List of Tables</b>	<b>xviii</b>
	<b>List of Symbols, Operators and Abbreviations</b>	<b>xix</b>
	<b>Erklärung</b>	

# 1 Introduction

## 1.1 Motivation and Background

Electromagnetic waves in the microwave frequency range offer the opportunity to examine an optically non-transparent medium under test (MUT). They are able to penetrate a variety of materials, including biological tissue, without ionization. In recent years, this has led to increasing interest in the field of microwave technologies in medical applications such as breast cancer imaging as investigated by Fear et al. [2013], Scapaticci et al. [2014], Preece et al. [2016], Wörtge et al. [2018], O’Loughlin et al. [2018], Helbig et al. [2012a], brain stroke detection corresponding to Scapaticci et al. [2018], Merunka et al. [2019] and temperature monitoring during thermal treatments as shown by Meaney et al. [2008], Haynes et al. [2014], Scapaticci et al. [2017], Ley et al. [2018b]. This thesis addresses two of these approaches applying a differential measurement technique based on ultra-wideband (UWB) technology, namely temperature monitoring during thermal treatments (e.g. hyperthermia) as well as contrast enhanced breast cancer imaging by means of magnetic nanoparticles (MNPs).

UWB differential temperature monitoring provides an approach to measure the temperature noninvasively during a hyperthermia application. Hyperthermia is a thermal procedure that supports oncological treatments (e.g. chemotherapy or radiotherapy). During this thermal treatment, the temperature is increased to 41-45 °C in the tumor region as indicated by Vrbova and Vrba [2012], Hilger [2013], whereby the temperature increase leads to an increased sensitivity to ionizing radiation. The treatment period ranges between 40 and 90 minutes as described by Paulides et al. [2014]. The heating is typically induced by radio frequency, ultrasound or microwaves. During thermal treatment it is necessary to monitor the temperature continuously to ensure that the temperature limits are not exceeded and the surrounding healthy tissue remains widely unaffected. In contrast to the commonly used invasive fiber optic catheters as summarized by Schena et al. [2016], microwave temperature monitoring offers a noninvasive and painless technique. The approach is based on the temperature dependent dielectric properties of tissue. Due to the high water content of tumorous tissue, the relative permittivity changes with increasing temperature. This results in a changing scattering behavior of the irradiated electromag-



netic waves, which can be measured by UWB differential measurement technique.

The detection and imaging of breast cancer by means of microwaves represent a promising alternative to the established methods such as X-Ray mammography or magnetic resonance imaging (MRI) (see Rieke and Butts Pauly [2008], Lüdemann et al. [2010]). Compared to X-Ray mammography, microwave imaging (MWI) uses non-ionizing radiation and offers higher patient comfort because a compression of the breast is not necessary. In contrast to MRI, MWI is much more cost-effective and has the potential to be used as a widespread screening method. MWI exploits the increased dielectric contrast between healthy and malignant tissue. However, extensive studies show that the dielectric contrast between fibroglandular and tumorous tissue is about 10 percent in the microwave frequency range as indicated by Lazebnik et al. [2007a], which might be insufficient to detect tumors reliably. The application of biocompatible MNPs functionalized with biological molecules, which are able to bind selectively with cancerous tissue, may enhance the detectability. Assuming that a sufficient amount of functionalized MNPs accumulate in the tumor, their magnetic properties can be modulated using an external polarizing magnetic field (PMF), while the surrounding tissue is not affected due to the nonmagnetic properties of tissue. This results in a changing scattering behavior at the boundary between MNP-loaded tumor and healthy surrounding tissue, which can be measured by means of microwave technology as shown in numerical studies (see Bucci et al. [2014]) as well as in experimental measurements (see Bellizzi et al. [2018], Ley et al. [2021]).

The aims of the thesis are:

- I. Implementation of a measurement setup for reliable temperature dependent UWB dielectric spectroscopy (DSP) of tissues and tissue-mimicking phantom materials.
- II. Characterization and modeling of the temperature dependent dielectric properties of tissue in the microwave frequency range.
- III. Evaluation of noninvasive temperature change detection by means of UWB microwave sensing.
- IV. Implementation of a measurement setup for MNP detection by means of UWB M-sequence technology.
- V. Investigation of influences (e.g. MNP mass, viscosity of the MNP-loaded target, magnetic field intensity of the PMF) on the detectability of MNPs.
- VI. Development of a measurement setup for contrast enhanced MNP breast cancer imaging by means of UWB pseudo-noise sensing.

## 1.2 Structure and Contribution of the Thesis

Chapter 2 describes the fundamentals of the thesis in more detail. In particular, the working principal of the M-sequence radar and the M-sequence network analyzer (NWA) are presented in Sections 2.1 and 2.2. The differential UWB imaging approach based on the Delay-and-Sum (DAS) beamforming algorithm is introduced in Section 2.3. The following Section 2.4 describes the dielectric properties of biological tissue and reviews the studies that have investigated the dielectric properties of tissue over a wide frequency range and as a function of temperature. Further, the magnetic properties of MNPs in the microwave frequency range are presented in Section 2.5.

Chapter 3 gives an overview over the current temperature monitoring techniques (see Section 3.1) as well as the MNP imaging technologies (see Section 3.2).

Chapter 4 addresses the aims I. to III. of this thesis. Section 4.1 deals with reliable measurements of the temperature dependent relative permittivity and the efficient conductivity of tissues in the microwave frequency range. The implemented measurement setup for temperature dependent DSP is presented in Section 4.1.1 and has been published in Ley et al. [2018a]. In Section 4.1.2, various influences on the DSP measurement of tissue are investigated to derive the optimal measurement procedure. In addition, a temperature-dependent Cole-Cole model is introduced, with which the measurement data can be efficiently summarized with a low number of parameters (see Section 4.1.3). Section 4.1.4 contains the results of the temperature dependent DSP measurements for liver, muscle, fat and blood in the temperature range between 30 °C and 50 °C and in the frequency range of 0.5 GHz up to 7 GHz. The results of the temperature dependent dielectric properties are fundamental regarding UWB temperature monitoring and have been published in Ley et al. [2019b,c,a]. Furthermore, Section 4.2 contains investigations on the detectability of temperature changes by means of M-sequence UWB technology. The content of this section is based on the contribution of Ley et al. [2018b].

Chapter 4 addresses the aims IV to VI of this work, whereby in Section 5.1 the relationship between the magnetic susceptibility and the UWB signal is explained theoretically. Section 5.2 presents the signal processing of the measured signals in order to remove the clutter and undesired signal components, respectively. Section 5.3 contains the experimental investigations of the different influences on the detectability of MNPs. Section 5.3.1 presents the experimental measurement setup and the results of MNP detection as a function of MNP mass, whereby the MNPs are diluted in distilled water as well as embedded in a tissue-mimicking medium. The methods and results of this section are published in Ley et al. [2015, 2020b]. Section 5.3.2 presents the measurement setup and the results of MNP detection at varied magnetic field strength of the external PMF. Furthermore, the setup is used to investigate the influence of the viscosity and the medium in which the MNPs

are embedded, respectively. Parts of this section are published in Ley et al. [2020b, 2021]. Section 5.4 deals with 3D UWB imaging of MNPs in a realistic measurement scenario for breast cancer imaging. The measurement setup is presented in Section 5.4.1. Furthermore, this section describes a setup in order to acquire the distribution of magnetic field intensity within the region of interest (air gap of the electromagnet). Section 5.4.2 introduces the imaging procedure and Section 5.4.3 presents the 3D imaging results for different target positions and penetration depths, respectively. Further, Section 5.4.4 shows the results of the magnetic field distribution and introduces a correction factor to compensate the magnetic field inhomogeneity. In Section 5.4.5, the influence of the modulation type of the external PMF on the MNP response is investigated. The development of the MWI setup over the last years as well as the methods and results of MNP imaging have been published in Ley et al. [2016, 2017, 2020a, 2021].

## 2 Basics

### 2.1 Ultra-Wideband Technology

Ultra-wideband (UWB) microwave technique has been extensively investigated in the context of medical applications during the last two decades as shown by Fear et al. [2002], Hilger et al. [2013], Brovoll et al. [2014], Preece et al. [2016], Sachs et al. [2018]. Typically, the medium under test (MUT) is illuminated with an UWB pulse, whereby the term UWB relates to a normalized bandwidth, which can be defined by the  $-10$  dB fractional bandwidth

$$b_f = 2 \cdot \frac{f_u - f_l}{f_u + f_l} \geq 0.2 \quad (2.1)$$

where  $f_u$  and  $f_l$  are the upper and the lower cut-off frequencies in relation to the center frequency  $f_m = (f_u + f_l)/2$  as illustrated in Figure 2.1. Furthermore, UWB systems require an absolute bandwidth

$$b_a = f_u - f_l \geq 500 \text{ MHz} \quad (2.2)$$

to avoid ambiguities with acoustic systems (e.g. audio devices, ultrasound or sonar sensors) as described by Sachs [2012].

The UWB systems in this work are based on M-sequence technology developed at Technische Universität Ilmenau. This technique is a correlation measurement approach with the objective to determine the impulse response function (IRF) of the MUT. Figure 2.2 shows the measurement principle of an UWB M-sequence radar. The stimulus signal  $a(t)$  (M-sequence) is generated by a binary high-speed shift register, which is pushed by a sin-

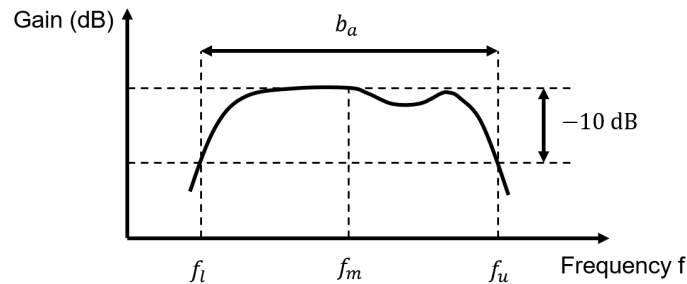


**Figure 2.1:** Example of a power spectrum of an UWB system according to Sachs [2012].

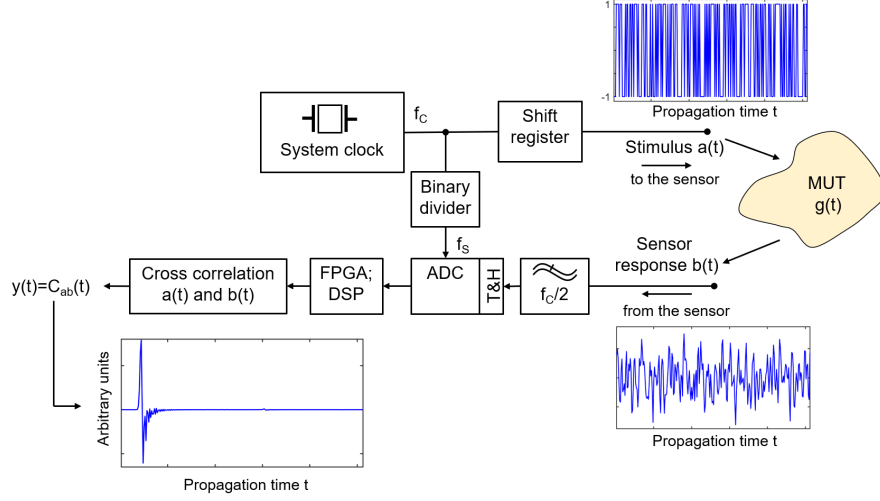


**Figure 2.2:** Schematic diagram of the M-sequence measurement corresponding to Sachs [2012]. The MUT is stimulated by an UWB pseudo-noise signal (M-sequence). The IRF is computed by the cross-correlation of the stimulus signal  $a(t)$  and the measured signal  $b(t)$ .

gle tone RF-clock of the repetition rate  $f_c$ . Each M-sequence consists of  $N_s$  elementary pulses (so-called chips) with values of 1 or -1, whereby the number chips with a value of 1 is one higher than the of number of chips with a value of -1. The length of an M-sequence is given by  $N_s = 2^{n_s} - 1$ , where  $n_s$  indicates the order of the shift register. Considering a time-invariant system for the measurement of an IRF of the MUT, the measured signal  $b(t)$  is given by

$$b(t) = \int a(\tau_s)g(t - \tau_s)d\tau_s = \int a(t - \tau_s)g(\tau_s)d\tau_s = a(t) * g(t) \quad (2.3)$$

where  $\tau_s$  is the time shift,  $a(t)$  the M-sequence,  $g(t)$  the IRF of the MUT and  $*$  represents the convolution operator. Convolving both sides of Equation (2.3) with the time inverted stimulus signal  $a(-t)$  yields

$$b(t) * a(-t) = g(t) * a(t) * a(-t). \quad (2.4)$$

This equation can be rewritten according to

$$C_{ab}(t) = g(t) * C_{aa}(t) \quad (2.5)$$

where  $C_{ab}(t)$  is the cross-correlation between the stimulus signal and the received radar signal and  $C_{aa}(t)$  corresponds to the autocorrelation of the stimulus signal. The auto-correlation  $C_{aa}(t)$  approaches a Dirac delta  $\delta(t)$  for a sufficient high RF clock rate  $f_c$  and

thus simplifies Equation (2.5) to

$$C_{ab}(t) = y(t) \sim g(t) \quad \text{for} \quad C_{aa}(t) \approx \delta(t) \quad (2.6)$$

where  $y(t)$  also represents the measured IRF and will be used in the further course of this work instead of  $C_{ab}(t)$ . The recorded sensor signal  $b(t)$  is filtered by an anti-aliasing filter and subsequently converted into the digital domain. Due to the fact that M-sequence signals are periodic, sub-sampling can be applied in order to reduce the technical effort (sampling rate of the analog-to-digital converter (ADC)) and to meet the Nyquist theorem. It has to be noticed that a high sub-sampling factor results in an increased recording time, because the data are distributed over several periods and captured with the lower sampling rate  $f_s$ . This reduces the required sampling rate of the ADC as well as the effort for data handling and the power consumption of the circuits. For more details on the M-sequence technology, please refer to Sachs [2012].

## 2.2 UWB M-sequence Network Analyzer

The UWB M-sequence technology is suitable to measure the dielectric properties of liquids, soft phantom materials as well as tissues as demonstrated by Sachs et al. [2007], Ley et al. [2018a, 2019a]. Here, the measurements are performed by using a network analyzer (NWA) based on the M-sequence technology developed at Technische Universität Ilmenau. Figure 2.3 shows the schematic of the UWB M-sequence NWA for a one-port measurement ( $S_{11}$ ). The stimulus signal (M-sequence) is generated by a digital shift register and

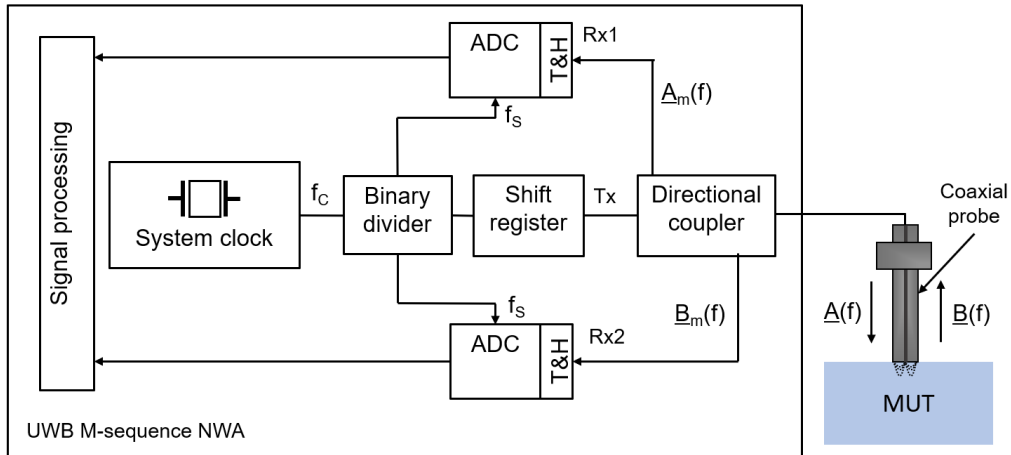


**Figure 2.3:** Schematic diagram of the UWB M-sequence NWA.

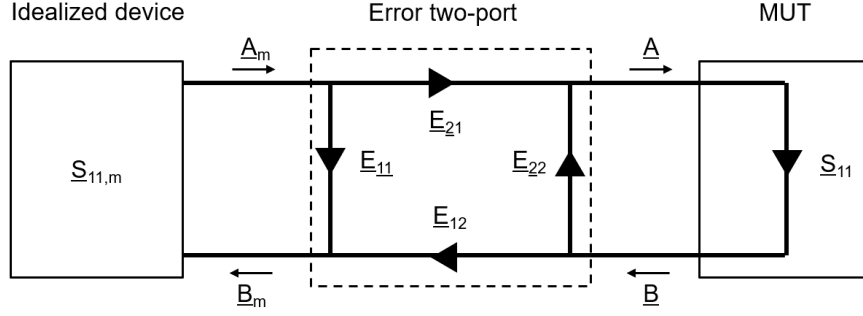


**Figure 2.4:** Error model of an one-port measurement according to Sachs et al. [2007].

transmitted to a directional coupler. The stimulus signal is then captured as reference signal  $\underline{A}_m$  at the receiving port Rx1 and is fed to a coaxial probe, which is in contact with the MUT. The reflected signal  $\underline{B}_m$  is captured at the receiving port Rx2. Both measured signals are needed to compute the reflection coefficient  $\underline{S}_{11}$  of the MUT. However, the reflection coefficient is affected by measurement errors, which can be described by error terms  $(\underline{E}_{11}, \underline{E}_{12}, \underline{E}_{21}, \underline{E}_{22})$  with an appropriate error model as described by Sachs et al. [2007] and shown in Figure 2.4. The measured reflection coefficient can be formulated as follows:

$$\underline{S}_{11m} = \frac{\underline{B}_m}{\underline{A}_m} = \underline{E}_{11} + \frac{\underline{E}_{21}\underline{E}_{12}\underline{S}_{11}}{1 - \underline{S}_{11}\underline{E}_{22}}. \quad (2.7)$$

Here, the expressions refer to the frequency domain, but for clarity, the frequency dependence is omitted in the equations. From Equation (2.7), the corrected reflection coefficient can be computed by

$$\underline{S}_{11} = \frac{\underline{S}_{11m} - \underline{E}_{11}}{\underline{S}_{11m}\underline{E}_{22} - \det \underline{E}} \quad (2.8)$$

with the determinant  $\det \underline{E} = \underline{E}_{22}\underline{E}_{11} - \underline{E}_{12}\underline{E}_{21}$ . Considering Equations (2.7) and (2.8), it is obvious that three independent error terms remain. Since the error terms are unknown, at least three calibration measurements must be performed. A common calibration method is the OSM-calibration with three calibration standards OPEN, SHORT and MATCH, whose behavior  $\underline{S}_{11}$  is known. In order to solve Equation (2.8), the three calibration measurements and the error terms can be summarized according to

$$\begin{bmatrix} 1 & -\underline{S}_{11}^O & \underline{S}_{11}^O \cdot \underline{S}_{11m}^O \\ 1 & -\underline{S}_{11}^S & \underline{S}_{11}^S \cdot \underline{S}_{11m}^S \\ 1 & -\underline{S}_{11}^M & \underline{S}_{11}^M \cdot \underline{S}_{11m}^M \end{bmatrix} \cdot \begin{bmatrix} \underline{E}_{11} \\ \det \underline{E} \\ \underline{E}_{22} \end{bmatrix} = \begin{bmatrix} \underline{S}_{11m}^O \\ \underline{S}_{11m}^S \\ \underline{S}_{11m}^M \end{bmatrix}. \quad (2.9)$$

The corresponding short form can be written by

$$\underline{\mathbf{A}} \cdot \underline{\mathbf{E}} = \underline{\mathbf{S}}_{11m} \quad (2.10)$$

where  $\underline{\mathbf{A}}$  represents the  $3 \times 3$  matrix on the left hand side,  $\underline{\mathbf{E}}$  summarizes the three error terms and  $\underline{\mathbf{S}}_{11m}$  contains the three reflection coefficients of the calibration measurements. Based on Equation (2.9), respectively (2.10), the error terms can be computed by the inversion of  $\underline{\mathbf{A}}$  according to

$$\underline{\mathbf{E}} = \underline{\mathbf{A}}^{-1} \cdot \underline{\mathbf{S}}_{11m}. \quad (2.11)$$

In order to determine the error term  $\underline{\mathbf{E}}$ , the reflection coefficients are computed by

$$\underline{S}_{11}^O = \frac{Y_P - \underline{Y}_O}{Y_P + \underline{Y}_O} \quad (2.12)$$

$$\underline{S}_{11}^S = \frac{Y_P - \underline{Y}_S}{Y_P + \underline{Y}_S} = -1 \quad (2.13)$$

$$\underline{S}_{11}^M = \frac{Y_P - \underline{Y}_M}{Y_P + \underline{Y}_M} \quad (2.14)$$

with the probe admittance  $Y_P = 1/50 \Omega$ . The further admittances are given as follows:

$$\underline{Y}_O = i2\pi f C_P \quad (2.15)$$

$$\underline{Y}_S = \infty \quad (2.16)$$

$$\underline{Y}_M = i2\pi f \underline{\varepsilon}_M C_P \quad (2.17)$$

where  $C_P \approx 20 \text{ fF}$  is the probe capacity. Considering Equation (2.16), it is obvious that  $\underline{S}_{11}^S = -1$  as given by Equation (2.13). The complex relative permittivity  $\underline{\varepsilon}_M$  of the matching liquid can be defined by the Debye-Model

$$\underline{\varepsilon}_M(f) = \varepsilon_\infty + \frac{\varepsilon_s - \varepsilon_\infty}{1 + i2\pi f \tau} + \frac{\sigma_s}{i2\pi f \varepsilon_0} \quad (2.18)$$

where  $\varepsilon_\infty$  is the permittivity at very high frequencies,  $\varepsilon_s$  the static permittivity,  $\tau$  the relaxation time,  $\sigma_s$  the static conductivity,  $\varepsilon_0$  the permittivity of free space and  $f$  is the frequency. If distilled water is used as matching liquid, the last term is omitted due to the lack of free charge carriers ( $\sigma_s = 0$ ). The further parameters ( $\varepsilon_\infty, \varepsilon_s, \tau$ ) are given by Kaatz [1989] or Ellison [2007]. Finally, the complex relative permittivity of the MUT can be calculated by its impedance corresponding to

$$\underline{Z}(f) = Z_P \cdot \frac{1 + \underline{S}_{11}}{1 - \underline{S}_{11}} \quad (2.19)$$



where  $Z_P$  is the probe impedance ( $50\ \Omega$ ) and  $\underline{S}_{11}$  is the corrected reflection coefficient according to Equation (2.8). With Equation (2.19) and the probe capacity  $C_P$ , the complex relative permittivity of the MUT is given by

$$\underline{\varepsilon}(f) = \frac{1}{C_P \cdot i2\pi f \cdot \underline{Z}(f)}. \quad (2.20)$$

## 2.3 Differential Ultra-Wideband Microwave Imaging

Differential microwave imaging is an electromagnetic sounding method to detect and image changes of permittivity and permeability within a MUT, making it attractive for a variety of medical applications. In Figure 2.5 a general scenario is illustrated, where a transmitting antenna (Tx) emits low power electromagnetic waves into the MUT (e.g. breast). The propagation of the electromagnetic waves (reflection, absorption, transmission and dispersion) inside of the MUT is determined by the tissue specific complex permittivity and permeability. It should be noted that the permeability of tissue is  $\underline{\mu} = 1$  due to its nonmagnetic behavior, but if we consider a scenario with the use of contrast agents (e.g.

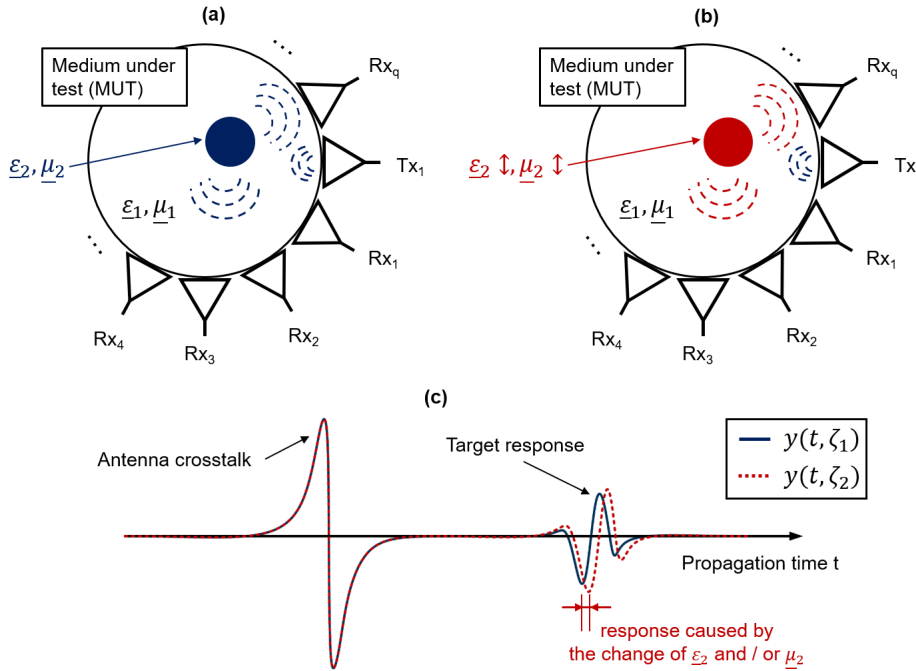


**Figure 2.5:** General scenario of microwave differential imaging; (a,b) Schematic of the measurement setup with a contrast induced by changing the permittivity ( $\underline{\varepsilon}_2 \downarrow$ ) and/or permeability ( $\underline{\mu}_2 \downarrow$ ) in the target region; (c) Schematic of the corresponding IRFs exemplarily for one channel.

use of magnetic nanoparticles), the magnetic properties also have to be taken into account. The electromagnetic waves are reflected at each boundary between different types of tissues due to their specific dielectric and magnetic properties. The receiving antennas (Rx) record the scattered electromagnetic waves and the IRF of the MUT is determined as described in Section 2.1.

Under some idealized conditions (no noise, no drift, omitting angular dependencies) the received signal  $y(t, \zeta)$  can be formulated as follows:

$$y(t, \zeta) = y_{cl}(t) + y_{tar}(t, \zeta) \quad (2.21)$$

where  $y_{cl}(t)$  is the static clutter (e.g. antenna crosstalk),  $y_{tar}(t, \zeta)$  represents the target reflection,  $t$  is the propagation time and  $\zeta$  refers to the contrast, for example a change in the dielectric properties caused by heating the target region. Considering a practical measurement scenario, the clutter is much stronger than the target reflection and both components overlap in time, which makes it difficult to separate them. Under the conditions mentioned above, the target response can be written as

$$\begin{aligned} y_{tar}(t, \zeta) &= x(t) * \frac{1}{r_{p,q}} * T(t) * \delta(t - \frac{r_{p,q}}{c}) * \Gamma_{\zeta}(t, \zeta) * A(t, r_{p,q}) * R(t) \\ &= y_0(t) * \Gamma_{\zeta}(t, \zeta) \end{aligned} \quad (2.22)$$

where  $*$  refers to the convolution,  $x(t)$  is the stimulus signal,  $R(t)$  and  $T(t)$  are the transmission IRFs of the receiving and transmitting antenna, respectively,  $\delta(t - r_{p,q}/c)$  represents the propagation time with the propagation velocity of the electromagnetic wave in the medium  $c$ ,  $\Gamma_{\zeta}(t, \zeta)$  is the contrast-dependent reflection coefficient and  $A(t, r_{p,q})$  the path-dependent attenuation of the electromagnetic wave corresponding to the distance  $r_{p,q}$  (path from  $\text{Tx}_p$  to the target and back to  $\text{Rx}_q$ ). The denominator  $r_{p,q}$  corresponds to the target reflection assuming that the target is a point scatterer. Due to the fact that the investigations are focused on the contrast induced changes, the contrast-independent components of the target reflection can be summarized to  $y_0(t)$ . Assuming that the environmental conditions are constant and a change of  $\underline{\varepsilon}$  or  $\underline{\mu}$  is only induced in the target region, the static clutter  $y_{cl}(t)$  can be eliminated by a differential measurement according to

$$\begin{aligned} \Delta y(t, \Delta\zeta_{1,2}) &= y(t, \zeta_1) - y(t, \zeta_2) \\ &= y_0(t) * [\Gamma_{\zeta}(t, \zeta_1) - \Gamma_{\zeta}(t, \zeta_2)] = y_0(t) * \Delta\Gamma_{\zeta}(t, \Delta\zeta_{1,2}). \end{aligned} \quad (2.23)$$

Considering Equation (2.23), it is obvious that the differential signal only depends on the difference of the induced contrast, which is also illustrated in Figure 2.5(c).

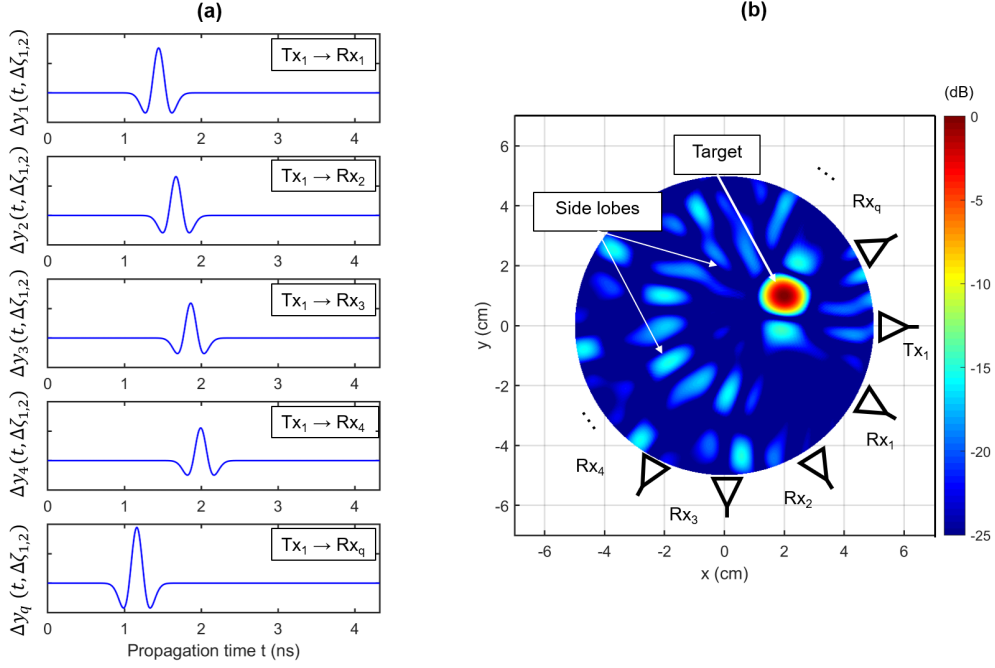


**Figure 2.6:** DAS imaging for a simulated scenario; **(a)** Differential target responses  $\Delta y_{ch}(t, \Delta\zeta_{1,2})$  exemplarily illustrated for five channels; **(b)** Two-dimensional intensity plot in decibels (dB) according to  $10 \cdot \log_{10}(I_0^2(\mathbf{r}_0))$  for a point scatterer at the position  $[x, y] = [2; 1]$  cm.

The target can be localized by applying an imaging algorithm, e.g. the Delay-and-Sum (DAS) beamforming algorithm, which is appropriate for UWB imaging. The principle is based on the coherent summation of the backscattered radar signals after clutter removal. The signal processing is performed in time domain as described in the literature (e.g. Fear et al. [2002]). In the case of microwave differential imaging, the input signals of the DAS beamformer are the differential signals  $\Delta y_{ch}(t, \Delta\zeta_{1,2})$ , where  $ch$  indicates the channel number. Figure 2.6(a) shows the differential signals of five channels corresponding to a simulated measurement scenario with a point scatterer at the position  $[x, y] = [2; 1]$  cm. For the purpose of target reconstruction, the propagation velocity within the MUT is supposed to be known. The DAS is a qualitative imaging algorithm and can be applied to reconstruct two dimensional as well as three dimensional images of the MUT. The volume of interest is subdivided into a grid of pixels (for a 2D scenario) or voxels (for a 3D scenario). In order to obtain the intensity value  $I_0$  of the pixel or voxel located at position  $\mathbf{r}_0$ , the signal components received from all antennas are superimposed with the propagation times according to the related transmitting antenna-voxel (or pixel)-receiving

antenna distance. Finally, the intensity of each pixel or voxel is computed by

$$I_0(\mathbf{r}_0) = \sum_{ch=1}^{N_{ch}} \Delta y_{ch}(\tau_{ch}(\mathbf{r}_0), \Delta\zeta_{1,2}) \quad (2.24)$$

where  $N_{ch}$  is the number of channels,  $\mathbf{r}_0$  represents the coordinates of the focal point and  $\tau_{ch}(\mathbf{r}_0)$  is the focal point-dependent time delay corresponding to the distance  $\text{Tx} \rightarrow \mathbf{r}_0 \rightarrow \text{Rx}$  of channel  $ch$ . Figure 2.6(b) shows the intensity distribution in decibels (dB) for a two-dimensional scenario with a circular antenna array (one Tx and eleven Rx) resulting in a total number of eleven channels. The image shows the main peak in the target region as well as additional side lobes. The influence of these lobes can be reduced by increasing the number of channels.

## 2.4 Dielectric Permittivity of Biological Tissue in the Microwave Frequency Range

The propagation of electromagnetic waves in biological tissue is determined by their specific dielectric properties as mentioned in the previous section. They are well known for various tissues over a wide frequency range as shown by a large number of studies (e.g. Gabriel et al. [1996b], Lazebnik et al. [2007a], Fornes-Leal et al. [2016], Farrugia et al. [2016], Porter et al. [2018]). The dielectric properties are characterized in terms of their complex relative permittivity

$$\underline{\varepsilon}(f) = \varepsilon'(f) - i\varepsilon''(f) \quad (2.25)$$

and the effective conductivity

$$\sigma(f) = i2\pi f\varepsilon_0\varepsilon''(f) \quad (2.26)$$

where the real part  $\varepsilon'$  represents the relative permittivity, the imaginary part  $\varepsilon''$  refers to the relative dielectric loss,  $\varepsilon_0$  is the permittivity of free space and  $f$  is the frequency. The dielectric properties of tissue are mainly determined by three dispersions ( $\alpha$ ,  $\beta$  and  $\gamma$ ).

The corresponding relaxation frequencies are in the range from kHz to GHz as described by Schwan [1957], Michaelson and Lin [1987], Gabriel et al. [1996a], Foster and Schwan [1996]. Figure 2.7 shows the relative permittivity as well as the effective conductivity for muscle tissue corresponding to the Cole-Cole model presented by Gabriel et al. [1996c]. The permittivity shows a continuous decrease over the frequency range. The  $\alpha$  dispersion occurs in the low frequency range ( $< 1$  kHz) and is associated with ionic diffusion effects at

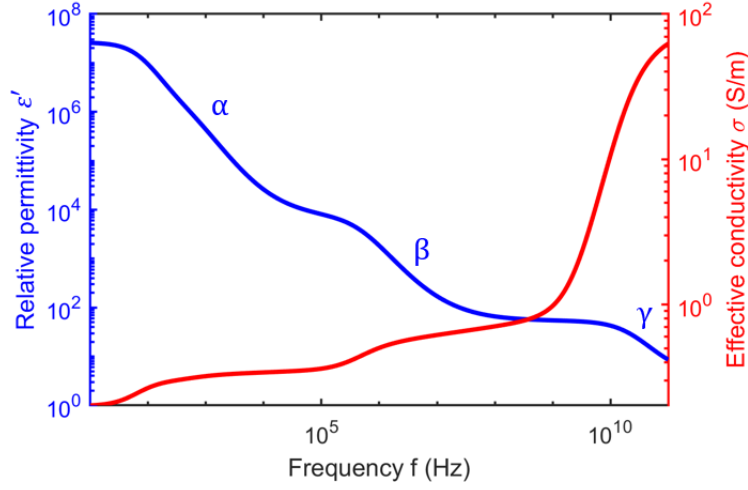


**Figure 2.7:** Dielectric properties of muscle tissue with the three major dispersion regions, which are typically for soft tissue. The relative permittivity and effective conductivity are determined with the Cole-Cole model as introduced by Gabriel et al. [1996c].

the cell membranes as explained by Gabriel et al. [1996a], Foster and Schwan [1996]. The  $\beta$  dispersion ranges in the hundreds of kilohertz region and results from the capacitive charging of cellular membranes in tissues. A further contribution to the  $\beta$  dispersion occurs at high radiofrequencies and arises from the rotation of proteins and other organic macromolecules as described by Gabriel et al. [1996a], Foster and Schwan [1996]. A further minor relaxation, known as the  $\delta$  dispersion, occurs between  $\beta$  and  $\gamma$  dispersion in the frequency range from about 100 MHz to some GHz and is caused by protein bound water as well as the rotation of amino acids and charged side groups of proteins as summarized by Schwan [1957], Michaelson and Lin [1987]. The  $\gamma$  dispersion ranges in the GHz region and is caused by the orientation polarization of water molecules as described by Schwan [1957], Gabriel et al. [1996a]. Gabriel et al. introduced a parametric model to describe the dielectric spectrum of tissues in the frequency range from 10 Hz to 100 GHz. A four pole Cole-Cole model was introduced to describe the dielectric spectrum of various tissues due to the three main relaxation regions and other minor dispersions (see Gabriel et al. [1996c]):

$$\underline{\varepsilon}(f) = \varepsilon_{\infty} + \sum_n \frac{\Delta\varepsilon_n}{1 + (i2\pi f\tau_n)^{1-\alpha_n}} + \frac{\sigma_s}{i2\pi f\varepsilon_0} \quad (2.27)$$

where  $n$  is the number of poles,  $\varepsilon_{\infty}$  the permittivity at very high frequencies,  $\Delta\varepsilon_n$  refers to the dispersion amplitudes,  $\tau_n$  represents the corresponding relaxation times and  $\sigma_s$  is the static conductivity. The parameter  $\alpha_n$  is set empirically and represents a distribution parameter describing the broadening of the dispersions. Figure 2.8 shows the relative

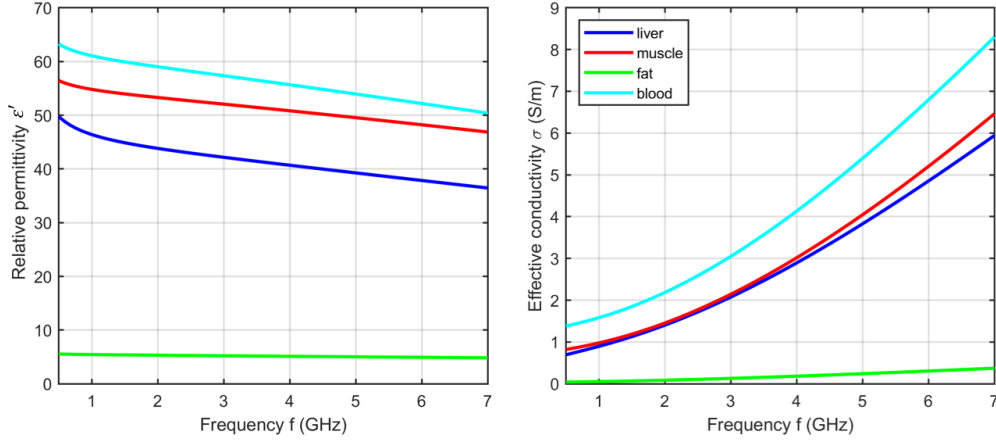


**Figure 2.8:** Relative permittivity and effective conductivity of various tissues in the microwave frequency range between 500 MHz and 7 GHz corresponding to the Cole-Cole model as introduced by Gabriel et al. [1996c].

permittivity as well as the effective conductivity of different tissues in the microwave frequency range corresponding to Equation (2.27) with the Cole-Cole parameter presented by Gabriel et al. [1996c].

The model shows the dielectric properties for various tissues over a wide frequency range for a constant temperature, but the relative complex permittivity and effective conductivity are temperature-dependent. However, only a few studies have measured the dielectric properties of tissues for different temperatures over a wide frequency range. Lazebnik et al. investigated the relative permittivity and effective conductivity of liver in the temperature range of 25 °C to 60 °C and in the frequency range of 0.5 GHz to 20 GHz. They presented a temperature-dependent single pole Cole-Cole model corresponding to Equation (2.27) with  $n = 1$  where the frequency dependence is modeled by temperature-dependent Cole-Cole parameters, which are determined by a second order polynomial fit (see Lazebnik et al. [2006]). Figure 2.9 shows the results of their temperature-dependent investigations for liver. The relative permittivity decreases with increasing temperature below the intersection point at 5 GHz, whereby this trend reverses for frequencies above the intercept. The effective conductivity has two intersection points at about 2.5 GHz and 18 GHz. Between both intercepts, the conductivity decreases with increasing temperature and this behavior reverses for frequencies lower than 2.5 GHz and higher than 18 GHz, respectively.

Further studies investigated the temperature-dependent dielectric properties of blood in the frequency range lower than 1 GHz (see Jaspard and Nadi [2002]), between 0.4 GHz and 20 GHz (see Wolf et al. [2011]) as well as in the frequency range from 0.4 GHz to 20 GHz (see Salahuddin et al. [2017]). In addition, there are some more studies investigating

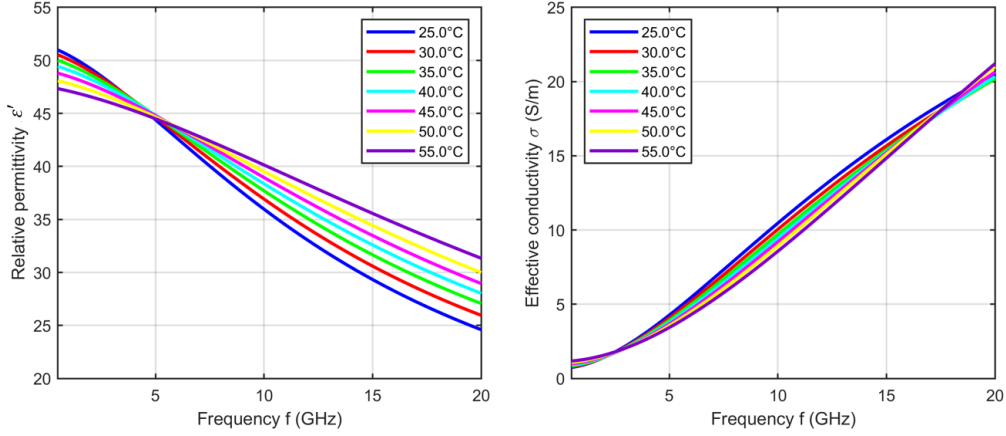


**Figure 2.9:** Temperature-dependent relative permittivity and effective conductivity of liver in the microwave frequency range between 500 MHz and 20 GHz corresponding to the temperature-dependent one pole Cole-Cole model introduced by Lazebnik et al. [2006].

the dielectric properties as a function of temperature, but only for discrete frequencies. A literature survey corresponding to the temperature-dependent dielectric properties of biological tissues is given by Rossmann and Haemmerich [2014].

## 2.5 Magnetic Susceptibility of MNPs in the Microwave Frequency Range

Single domain magnetic nanoparticles based on iron oxide (magnetite or hematite) commonly have radii ranging from 2 to 10 nm. The complex susceptibility of such single domain particles can be described by their parallel (longitudinal) and perpendicular (transversal) components corresponding to Fannin et al. [1997a]:

$$\underline{\chi}(f) = \frac{1}{3}[\underline{\chi}_{\parallel}(f) + 2\underline{\chi}_{\perp}(f)] \quad (2.28)$$

where the parallel susceptibility  $\underline{\chi}_{\parallel}(f)$  is dominated by relaxation mechanisms and the perpendicular susceptibility  $\underline{\chi}_{\perp}(f)$  is mainly related to the ferromagnetic resonance as described by Fannin et al. [1997a], Bellizzi and Bucci [2013]. The parallel susceptibility can be expressed by the Debye equation

$$\underline{\chi}_{\parallel}(f) = \frac{\chi_{\parallel 0}}{1 + i2\pi f\tau_{\parallel}} \quad (2.29)$$

where  $\chi_{\parallel 0}$  is the static parallel susceptibility. The effective relaxation time  $\tau_{\parallel}$  depends on

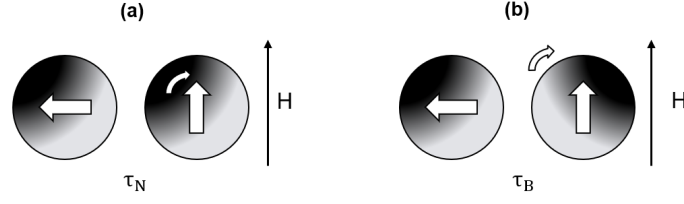


**Figure 2.10:** Néel rotation and Brownian rotation; **(a)** Néel rotation where the magnetic moment rotates while the particle remains fixed; **(b)** Brownian rotation where the particle rotates while the magnetic moment remains fixed with respect to the crystalline axes.

two relaxation processes, Néel and Brownian relaxation, that describe the time delay of the reorientation of the MNPs arising from a change of an external magnetic field  $H$ . The Néel relaxation relates to the internal fluctuation of the magnetic moment. Assuming that the anisotropic energy threshold will be exceeded, the direction of magnetization changes due to the rotation of the magnetic moments within the magnetic particles as illustrated in Figure 2.10(a). The Néel relaxation time is given by

$$\tau_N = \tau_0 \exp\left(\frac{K_a V_p}{k_b \vartheta}\right) \quad (2.30)$$

where  $\tau_0$  is a characteristic time,  $K_a$  the anisotropy factor,  $V_p$  the core volume of the particle,  $k_b$  the Boltzmann constant and  $\vartheta$  the absolute temperature. The Brownian relaxation is related to the mechanical rotation of the particle in a carrier medium as depicted in Figure 2.10(b). It is defined by

$$\tau_B = \frac{3V_h \eta}{k_b \vartheta} \quad (2.31)$$

where  $V_h$  is the hydrodynamic volume of each MNP and  $\eta$  is the effective viscosity of the carrier liquid. If Brownian and Néel relaxation act simultaneously, the overall relaxation behavior is given by the effective relaxation time

$$\tau_{\parallel} = \frac{\tau_N \cdot \tau_B}{\tau_N + \tau_B}. \quad (2.32)$$

The transverse or perpendicular susceptibility is associated with the ferromagnetic resonance. Under equilibrium conditions, the magnetization  $M$  and the anisotropy axis of the particles are parallel. A deflection of  $M$  from its equilibrium position results in the precession of the magnetization around the anisotropy axis as described by Skrotskii and Kurbatov [1966], Neudecker [2014], Bellizzi and Bucci [2013] and as illustrated in Figure 2.11. The precession of  $M$  can be achieved by an additional low power electromagnetic



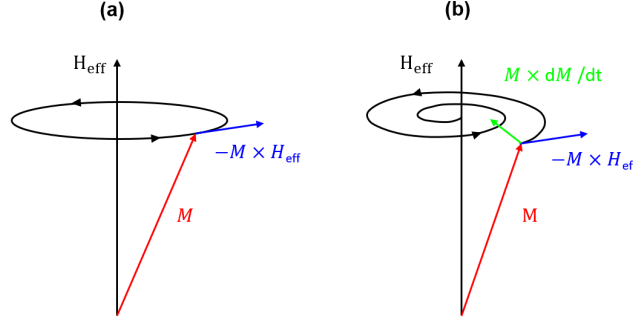


**Figure 2.11:** (a) Precession of the magnetization around the effective magnetic field direction  $H_{eff}$  with a high frequency magnetic field; (b) Damped precession of the magnetization without the presence of a high frequency magnetic field corresponding to Skrotskii and Kurbatov [1966].

microwave field  $h$  perpendicular to the magnetization field. After finishing this excitation,  $M$  returns to equilibrium conditions after a few nanoseconds as illustrated by Hoffmann [2010]. The motion of the magnetization can be described by the Landau-Lifshitz-Gilbert equation corresponding to Gilbert [1955]:

$$\frac{dM}{dt} = \underbrace{-|\gamma|\mu_0 \cdot M \times H_{eff}}_{\text{precession}} + \underbrace{\frac{\alpha_d}{M_s} \cdot \left( M \times \frac{dM}{dt} \right)}_{\text{damping}} \quad (2.33)$$

where  $\gamma$  is the gyromagnetic ratio,  $\mu_0$  is the permeability constant in free space and  $\alpha_d$  is a phenomenological and dimensionless damping parameter. The effective magnetic field is related to the free energy density and can be formulated as

$$H_{eff} = H_{Ani} + H_{Demag} + H + h \quad (2.34)$$

with the internal fields (anisotropy field  $H_{Ani}$  and demagnetizing field  $H_{Demag}$ ) as well as a static external DC field  $H$  and the microwave driving field  $h$  as described by Hoffmann [2010]. The application of an electromagnetic microwave field  $h$  leads to a precession of the magnetic moment as mentioned above. In the case where the deviation of  $M$  from the anisotropy axis is small, the resonance frequency without an external PMF (DC field) is given by

$$f_{res} = \frac{\gamma H_A}{2\pi} \quad (2.35)$$

where  $H_A$  represents the internal magnetic field. Considering a single domain particle with an uniaxial anisotropy, the internal anisotropy field is defined by

$$H_A = \frac{2K_a}{M_s} \quad (2.36)$$

with the saturation magnetization  $M_s$  of the MNP core according to Fannin et al. [1997b]. The resonant component of the perpendicular susceptibility can be described as in Coffey et al. [1993b]:

$$\chi_{\perp}(f) = \chi_{\perp 0} \frac{1 + i 2\pi f \tau_{02} + \Delta}{(1 + i 2\pi f \tau_{02})(1 + i 2\pi f \tau_{\perp}) + \Delta} \quad (2.37)$$

where  $\chi_{\perp 0}$  is the static transverse susceptibility,  $\tau_{\perp}$  is the transverse magnetic relaxation time,  $\tau_{02}$  a second effective relaxation time and

$$\Delta = \frac{\sigma_E \tau_{02} (\tau_N - \tau_{\perp})}{\alpha_a^2 \tau_N^2} \quad (2.38)$$

where  $\sigma_E$  is the ratio of anisotropy energy to thermal energy,  $\tau_N$  the Néel relaxation time and  $\alpha_a$  a dimensionless damping factor as introduced by Coffey et al. [1993b,a], Fannin et al. [1997b]. Finally, the overall frequency-dependent susceptibility is given by combining Equations (2.28), (2.29) and (2.37) according to Fannin et al. [2002]:

$$\chi(f) = \frac{1}{3} \left[ \frac{\chi_{\parallel 0}}{1 + i 2\pi f \tau_{\parallel}} + 2\chi_{\perp 0} \frac{1 + i 2\pi f \tau_{02} + \Delta}{(1 + i 2\pi f \tau_{02})(1 + i 2\pi f \tau_{\perp eff}) + \Delta} \right] \quad (2.39)$$

where  $\tau_{\perp}$  is replaced by

$$\tau_{\perp eff} = \frac{\tau_{\perp} \cdot \tau_B}{\tau_{\perp} + \tau_B} \quad (2.40)$$

in order to include the effects of the Brownian relaxation. If an additional external PMF with an amplitude  $H$  is applied, the resonance frequency will increase corresponding to

$$f_{res}(H) = \frac{\gamma(H_A + H)}{2\pi} \quad (2.41)$$

as described by Fannin et al. [2005]. Furthermore, the dependence of the static susceptibilities and the relaxation times on the magnetic field intensity have to be taken into account as investigated by Fannin [2002], Fannin et al. [2002].

The magnetic susceptibility of MNPs depending on the magnetic field intensity of an external PMF has been measured by Fannin et al. [1997a] in the frequency range between 30 MHz and 6 GHz for magnetic field intensities between 0 and 116 kA/m and by Bucci et al. [2017] in the frequency range between 100 MHz and 8 GHz for magnetic field in-

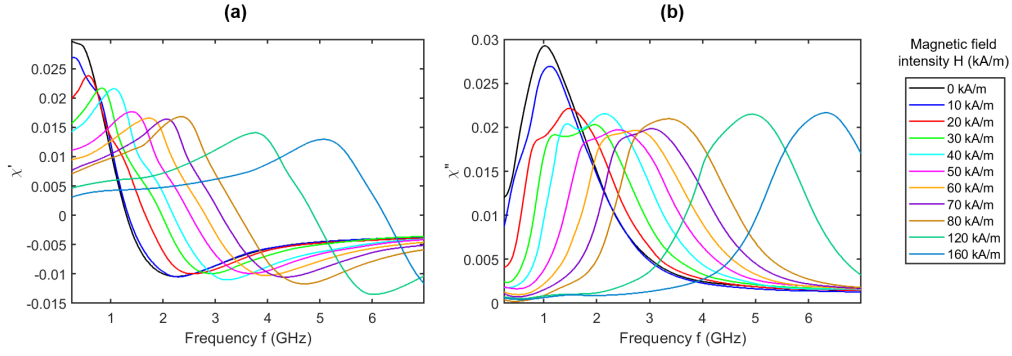


**Figure 2.12:** (a) Real part and (b) opposite of the imaginary part of the magnetic susceptibility of iron oxide nanoparticles corresponding to Bucci et al. [2017].

tensities between 0 and 160 kA/m. Figure 2.12 shows the real and the opposite of the imaginary part of the magnetic susceptibility corresponding to the measurements of Bucci et al. [2017] where the increase of the resonance frequency with a rising magnetic field intensity is shown. The results of these investigations are fundamental for MNP detection and imaging by means of UWB technology. The change of the magnetic susceptibility  $\chi(f, H)$  or relative permeability  $\mu(f, H)$  of the MNPs, caused by the changing external magnetic field intensity, results in a change of the measured UWB differential signal as shown in Chapter 5.

## 3 State of the Art

### 3.1 Temperature Monitoring during Thermal Treatment

The aim of thermal treatments (e.g. hyperthermia) is to increase the body temperature in the tumor area in order to increase the sensitivity of tumor cells during oncological treatments (chemotherapy, radiation therapy). In the case of hyperthermia the temperature is increased to 41-45 °C as described by Vrbova and Vrba [2012], Hilger [2013], whereby the treatment time ranges between 40 and 90 minutes as indicated by Paulides et al. [2014]. It is crucial that the temperature does not exceed the upper temperature limit and that the surrounding healthy tissue remains unaffected. For this reason, a continuous temperature monitoring during the thermal treatment is necessary.

Fiber optic catheters (FOC) are commonly used to monitor the temperature during thermal treatments continuously as summarized by Schena et al. [2016]. The method is affordable and shows a high accuracy, but the spatial resolution is limited due to the number of probes. The probability of detecting all temperature hotspots is low, especially for large volumes. In addition, inserting the invasive probes can cause patient discomfort and bears risks such as inflammation or bacterial infections.

Recent studies investigated the potential of Magnetic Resonance Imaging (MRI) in terms of noninvasive temperature monitoring. The main temperature-dependent parameters (in order to their temperature sensitivity) are the proton-resonance frequency (PRF) shift, the diffusion coefficient and the longitudinal relaxation time (T1) as described by Lüdemann et al. [2010].

The PRF shift method shows a high sensitivity and linear temperature dependence for water protons over a relatively large temperature range. Therefore, the technique is suitable for high water content tissues, but studies (e.g. Lüdemann et al. [2010]) indicate that this method is not sensitive when applied to fatty tissue.

The diffusion coefficient also shows a high temperature sensitivity. Studies indicate that the change in diffusion is approximately 2.4 %/°C (see Zhang et al. [1992], Lüdemann et al. [2010]). However, this method is limited due to its high motion sensitivity, a comparatively long echo time, the anisotropy of tissue and its limited application in adipose tissue.

The spin-lattice relaxation time  $T_1$  is a further parameter in terms of temperature mapping. A temperature increase results in an increasing relaxation time  $T_1$  of 0.8 %/°C to 2 %/°C.

Further temperature-dependent parameters are the equilibrium magnetization ( $M_0$ ), transverse or spin–spin relaxation time  $T_2$ , magnetization transfer and temperature-dependent contrast agents. An overview of magnetic resonance thermometry (MRT) and the various magnetic properties which can be used to estimate the temperature distribution is given by Rieke and Butts Pauly [2008]. A further overview of MRT and its clinical performance as well as future potentials is presented by Feddersen et al. [2021].

In general, the use of an MRI is associated with very high costs and compliance with spatial and technological requirements, regardless of what physical effect is exploited to determine the temperature distribution.

Ultrasound thermometry (UT) is based on the temperature-dependent properties of acoustic parameters to estimate temperature changes noninvasively during hyperthermia treatments (see Casper et al. [2012]). Most common approaches exploit the changing attenuation coefficient, the variations in the backscattered energy at the boundaries (tissue inhomogeneities) or the echo shift, which is caused by the change in the thermal tissue expansion and the propagation velocity of the sound waves as shown by Arthur et al. [2005], Foiret and Ferrara [2015]. However, this technique is very susceptible to motion artifacts as demonstrated in Seo et al. [2014] .

Microwave radiometry is a passive method being investigated for hyperthermia temperature monitoring as proposed by Dubois [1996], Arunachalam et al. [2008]. The measuring principle is based on the spontaneous electromagnetic radiation emitted by lossy objects in the microwave range. Thereby, the radiated power depends on the temperature and can be measured by radiometric systems. In contrast to infrared thermography systems, which can measure temperatures only on the tissue surface, microwave radiometry is able to determine the temperature inside of a body due to the higher penetration depth (see Klemetsen and Jacobsen [2012]). The challenge of this approach is that the weak microwave radiation has to be in coexistence with the natural microwave radiation as well as with disturbance sources in this frequency range.

In recent years active microwave sensors have been investigated to determine the temperature changes noninvasively. The approach relies on the temperature-dependent dielectric properties of tissue. A change of the tissue temperature causes a change of the relative permittivity and the effective conductivity. This results in a changing scattering behavior

of the electromagnetic wave, which can be measured by means of microwaves.

The temperature monitoring systems presented by Meaney et al. [2008] and Haynes et al. [2014] are working with single frequencies at 900/1100 MHz and 915 MHz, respectively. Haynes et al. summarized a temperature sensitivity of 1 °C for a 3D image reconstruction of their phantom experiments. A further development of their approach is presented by Chen et al. [2018], where the Born approximation technique is replaced by the nonlinear distorted Born iterative method, which provides a better approximation of the mean temperature within the medium under test. Meaney et al. [2008] demonstrated a microwave tomographic imaging system in combination with a high intensity focused ultrasound therapy device and their results showed 2D images representing temperature changes. They summarized a temperature sensitivity and accuracy better than 0.5 °C and 0.35 °C, respectively, for the presented experimental setup.

The Chirp-pulse microwave computed tomography (CP-MCT) offers a further approach to determine the temperature distribution in biological tissue as presented by Miyakawa [1993] and Bertero et al. [2000]. A transmitting antenna emits a chirp-pulse signal with a bandwidth between 1 and 2 GHz into the MUT and the transmitted signal is measured by a receiving antenna at the opposite MUT. The technique is based on the estimation of the point spread function, which is then used for an appropriate deconvolution method. The results of their phantom measurements indicate a spatial resolution of 10 mm and confirmed the feasibility of measuring temperature changes for a two-dimensional scenario.

UWB microwave temperature monitoring according to the radar principle differs from the narrow-band microwave tomography by its lower computational effort. The images represent a mapping of the reflected signal energy instead of absolute values of the relative permittivity and the effective conductivity. The approach is based on the temperature dependence of the dielectric properties of tissue. An increase in temperature of the malignant tissue leads to a change of its dielectric properties, which can be measured using UWB technology as described in more detail in Chapter 4. The approach of noninvasive temperature monitoring with UWB microwaves has hardly been explored. As far as is known, only the research group of Prof. Vrba (Department of Electromagnetic Field of the Czech Technical University in Prague), is also working in this field, focusing mainly on the design and optimization of hyperthermia applicator systems as presented by Fiser et al. [2016] and Fiser [2018].

## 3.2 Magnetic Nanoparticles in Medical Applications

The use of contrast agents for biomedical applications has been investigated over the last decades. Due to their specific properties, magnetic nanoparticles (e.g. iron oxide) are exploited by different technologies for diagnostics and therapy.

MNPs can be used to target delivery of multiple immunotherapeutics as investigated by Cheng et al. [2021], as well as for accurate targeting of therapeutic-drug-delivery microrobots as shown by Lee et al. [2021]. Magnetic field hyperthermia offers a promising approach to support cancer therapies in which the MNPs are locally heated by a time-varying magnetic field as described by Wells et al. [2021]. Furthermore, magnetoelastic biosensors combined with magnetic nanoparticles offer an approach for the wireless detection of pathogens in liquids as well as for real-life diagnostic purposes as proposed by Campanile et al. [2020].

The approach of modulating magnetic nanoparticles by a magnetic field in order to enhance sensitivity has been used for different biomedical applications such as a computational cytometer based on magnetically modulated lensless speckle imaging as described by Zhang et al. [2019] and magnetomotive photoacoustic (mmPA) imaging as shown by Jin et al. [2010].

Furthermore, the possibility of selective MNP targeting to a region of interest (e.g., tumor) makes them attractive as a contrast agent for diagnostics and imaging. Therefore, the need for MNP imaging methods has motivated research in several technologies such as magnetic resonance imaging (MRI), magnetic particle imaging (MPI), magnetorelaxometry (MRX), and contrast enhanced microwave imaging (MWI).

Recent studies show the potential of iron oxide nanoparticles in order to improve the contrast in MRI. A contrast can be realized by influencing the longitudinal relaxation time  $T_1$  and the transverse relaxation time  $T_2$ . Superparamagnetic iron oxide nanoparticles (SPIONs) mainly cause a negative  $T_2$  contrast. If a sufficient amount of SPIONs is accumulated in the tissue, the spin-spin relaxation time  $T_2$  decreases, resulting in a negative contrast enhancement as described by Pankhurst et al. [2003], Dulińska-Litewka et al. [2019]. Furthermore, Bao et al. [2016] show that ultra small spherical iron oxide nanoparticles ( $<5$  nm) reduce the longitudinal relaxation time  $T_1$  and act as positive contrast agent.

Magnetic Particle Imaging (MPI) is a noninvasive and quantitative 3D imaging modality of ferromagnetic nanoparticles that offers high spatial and temporal resolution (see Weizenecker et al. [2009]). The approach relies on the nonlinear magnetization curve of the ferromagnetic nanoparticles. An MPI system contains two different magnetic fields, a static magnetic field (selection field) and an oscillating field (drive or modulation field)

with a single frequency. The selection field provides a field free point in space (FFP), which can be realized with a special Helmholtz-type coil setup. If the MNPs are located in the FFP, their magnetic properties are modulated by the oscillating field. Due to the nonlinear magnetization, the time-dependent MNP response exhibits higher harmonics. If the particles are outside the FFP, they are saturated due to the selection field. In this case the modulation field does not influence the MNP response significantly and the higher harmonics disappear. A description of the MPI principle is given by Gleich and Weizenecker [2005]. Due to the special coil design, most experimental systems have so far been limited to small objects (see Ludewig et al. [2017], Wu et al. [2019]).

Magnetorelaxometry (MRX) is a noninvasive method which offers qualitative and quantitative information about the spatial distribution of MNPs as shown by Liebl et al. [2015], Schier et al. [2020]. The approach is based on the detection of the time-varying magnetic flux density of the MNPs. In a first step, the MUT is exposed to a constant and homogeneous magnetizing field, with the MNPs rotating in the direction of the magnetic field. In the second step, the magnetic field is switched off and the MNPs turning back into a randomly oriented distribution of magnetic moments. The relaxation of the MNPs is measured by an array of sensitive magnetic field sensors, such as superconducting quantum interference devices (SQUIDS). The distribution of the MNPs is determined by applying an inverse problem solution. More information on this principle can be found in Wiekhorst et al. [2012].

The approach of using MWI in combination with contrast agents for cancer detection was introduced by Bellizzi et al. [2011]. The MUT (e.g. breast) is stimulated by low-power electromagnetic waves in the microwave frequency range, which are partially reflected at each dielectric and magnetic boundary. Assuming that a sufficient amount of functionalized MNPs accumulates within the malignant tissue, the magnetic properties of the MNPs can be modulated by an external PMF, resulting in a changing behavior of their magnetic properties. In addition, the scattering behavior of the MNPs changes and the microwave magnetic response is modified accordingly. Due to the nonmagnetic properties of the surrounding tissue, the MNP response can be derived by a differential measurement strategy between the ON and OFF state of the external PMF. A more detailed description is presented in Chapter 5. In the context of contrast enhanced MWI, Bucci et al. [2014] performed numerical simulations with regard to the optimal measurement configuration. Furthermore, Bucci et al. [2018] evaluated the detection limits in nanoparticle enhanced MWI. In addition Bucci et al. [2021] investigated the cause of disturbing influences on contrast enhanced MWI within the framework of experimental measurements.



## 4 UWB Microwave Temperature Monitoring

The knowledge of temperature distribution within the body during thermal treatments (e.g., hyperthermia) is crucial to ensure patient safety and improve clinical outcome as described in Section 1.1. UWB temperature monitoring is a promising technique to measure temperature continuously and noninvasively. The approach is based on the temperature-dependent change of the dielectric properties of biological tissue. Due to the high water content of a tumor, the permittivity of cancerous tissue changes with increasing temperature. This results in a changing scattering behavior of the electromagnetic waves and these differences can be measured by means of UWB radar technology as demonstrated by Ley et al. [2018b], Fiser et al. [2018], Prokhorova et al. [2021]. Figure 4.1 illustrates the principle of the approach exemplarily for one channel. The transmitting antenna (Tx) emits low power electromagnetic waves into the MUT. The electromagnetic waves propagate according to the tissue specific dielectric properties  $\underline{\varepsilon}(f, \vartheta)$ , which are frequency- and the temperature-dependent. Considering a scenario without magnetic contrast agents (e.g. magnetic nanoparticles), a permeability of  $\underline{\mu} = 1$  can be assumed due to the nonmagnetic

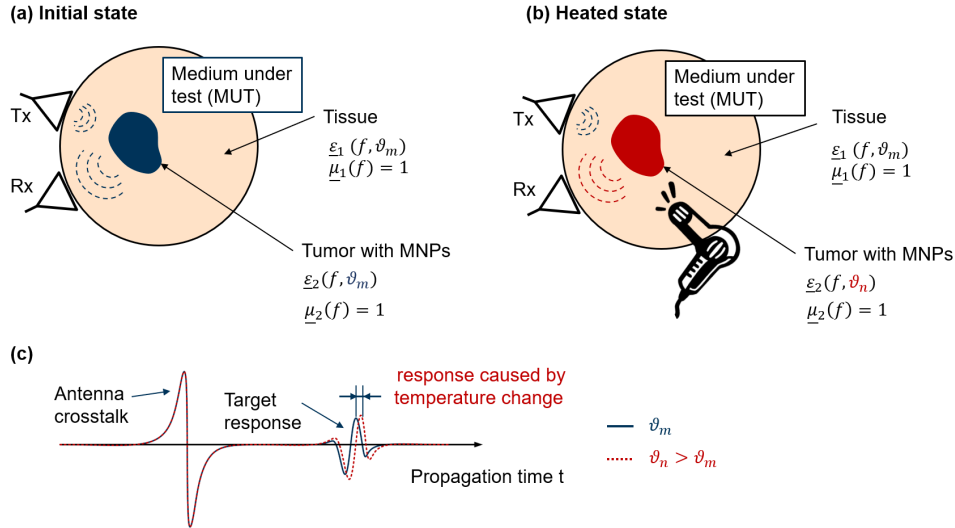


**Figure 4.1:** Principle of noninvasive temperature monitoring by means of UWB technology; (a) Initial state without heating before treatment; (b) Heated state during treatment; (c) Resulting IRFs for both temperature states.

behavior of tissue. The electromagnetic waves are partially reflected at each dielectric boundary. If the temperature is increased in a specific region (e.g. tumor), the scattering of the electromagnetic waves at the boundary between healthy and tumor tissue changes due to the temperature-dependent dielectric properties. These changes can be measured by the receiving antenna (Rx) as illustrated in Figure 4.1(c) where the corresponding IRFs for the initial and the heated state are shown. For simplicity, the antenna crosstalk and the target response are separated in propagation time and the amplitudes of the target responses are half of the crosstalk, which is not the case in a real measurement. In a realistic scenario, the change of the target response caused by a temperature change can be  $10^3$  times less than the amplitude of the antenna crosstalk. Furthermore, both components (crosstalk and target response) overlap in time, making it difficult to separate them. However, assuming that the clutter remains constant between the initial state and the measurement in the heated condition, the signal changes caused by the temperature change can be determined by a differential measurement and subtracting both IRFs, respectively. To estimate the temperature change corresponding to the measured difference in the UWB radar signal, the temperature-dependent dielectric properties of tissue have to be known over a wide frequency range. Therefore, this chapter deals with the measurement of the dielectric properties corresponding to the temperature range during a hyperthermia treatment and with respect to the working frequency range of the UWB radar systems. Furthermore, the feasibility of temperature change detection by means of UWB pseudo-noise sensing is demonstrated.

## **4.1 UWB Temperature-Dependent Dielectric Spectroscopy of Porcine Tissue and Blood**

This section is motivated by the lack of knowledge in terms of temperature-dependent dielectric properties of tissue over a wide microwave frequency range as described in Section 2.4. This study examines the relative permittivity and effective conductivity of porcine liver, muscle, fat and blood in the microwave frequency range from 0.5 GHz to 7 GHz and in the temperature range between 30 °C and 50 °C.

### **4.1.1 Measurement Setup**

The measurements of temperature-dependent dielectric properties are performed by means of an UWB M-sequence network analyzer (NWA) based on a one port measurement as described in Section 2.2. Figure 4.2 shows the measurement setup corresponding to Ley et al. [2019a]. In both cases, tissue and blood analysis, a coaxial probe (N1501A performance probe, Keysight Technologies, Santa Clara, CA, USA) was connected to the NWA

via coaxial cable. The dielectric properties were recorded with a frequency resolution of 35 MHz in the frequency range between 0.5 GHz to 7 GHz corresponding to a total number of 189 equidistant data points. The temperature was acquired by means of a temperature probe connected to a precision thermometer (GMH 3750, GHM Messtechnik GmbH, Remscheid, Germany). A total number of 21 temperature values were recorded in steps of 1 °C in the range between 30 °C and 50 °C.

The tissue samples had a cylindrical shape with a diameter of 6 cm and a thickness varying between 1 and 1.5 cm. The sample thickness ensures a sufficient distance from the tip of the coaxial probe to the bottom of the container to avoid unwanted reflections as proven by Hagl et al. [2003] and Meaney et al. [2016] as well as by own investigations. In order to prevent excessive desiccation, the samples were wrapped in plastic foil with two holes on the surface to ensure a direct contact of the temperature and coaxial probe

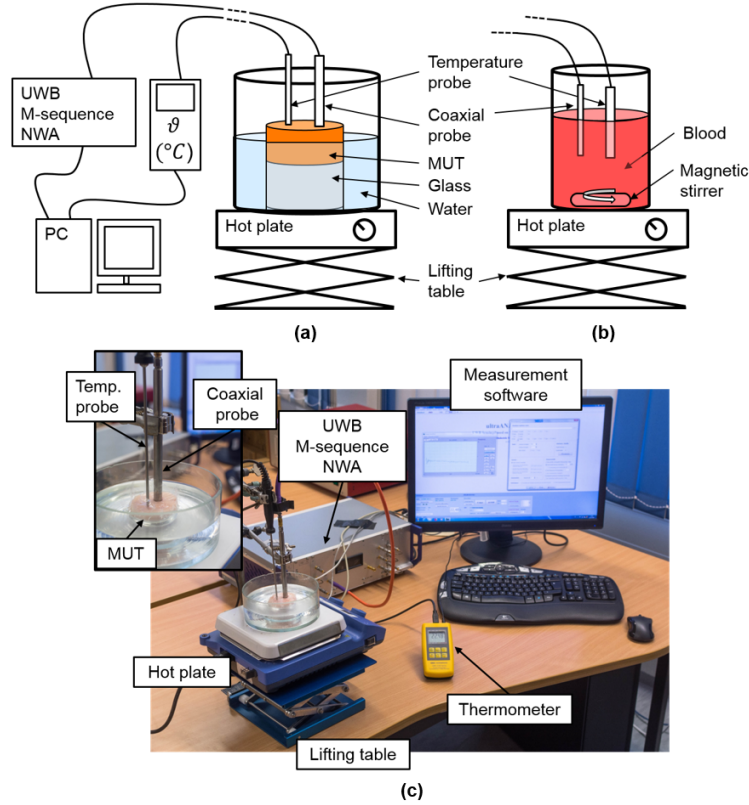


**Figure 4.2:** Schematic of the measurement setup for temperature-dependent UWB dielectric spectroscopy of (a) tissues and (b) blood by means of a coaxial probe connected to an UWB M-sequence network analyzer (NWA). The temperature is acquired by a temperature probe connected to a precision thermometer. Both, radar signals and temperature are recorded in parallel; (c) Corresponding laboratory measurement setup.

with the tissue sample. The samples were placed in a water bath, which was used for sample heating and cooling, respectively. Both measuring probes were placed equidistant from the center of the tissue sample in order to ensure an almost identical temperature development at the position of the coaxial and temperature probe due to the symmetrical shape of the sample. In terms of blood analysis, the blood was filled in a glass and heated by a hot plate as shown in Figure 4.2(b). The measurement probes were immersed a few millimeters into the liquid. A rotating magnetic stirrer was used to avoid a sedimentation of the cellular components during the measurement and to ensure a homogeneous temperature distribution of the blood.

The dielectric measurements were performed by applying a three term OSM calibration including SHORT, OPEN and distilled water as matching liquid at room temperature as described in Section 2.2. The complex dielectric properties of distilled water are defined by the Debye model

$$\begin{aligned}\underline{\varepsilon}(f, \vartheta) &= \varepsilon'(f, \vartheta) - i\varepsilon''(f, \vartheta) \\ &= \varepsilon_\infty(\vartheta) + \frac{\varepsilon_s(\vartheta) - \varepsilon_\infty(\vartheta)}{1 + i2\pi f\tau(\vartheta)} + \frac{\sigma_s(\vartheta)}{i2\pi f\varepsilon_0}\end{aligned}\quad (4.1)$$

where  $\underline{\varepsilon}$  is the complex dielectric permittivity,  $\varepsilon_\infty$  the permittivity at very high frequencies,  $\varepsilon_s$  the static permittivity,  $\tau$  the relaxation time,  $\sigma_s$  the static conductivity,  $\varepsilon_0$  the permittivity of free space,  $f$  the frequency and  $\vartheta$  the absolute temperature in degree Celsius. The temperature-dependent parameters  $(\varepsilon_\infty, \varepsilon_s, \tau)$  of distilled water are defined by the Debye interpolation function of Kaatz [1989] with  $\sigma_s = 0$ . The dielectric loss  $\varepsilon''$  can be converted into the effective conductivity according to Lazebnik et al. [2007a]:

$$\sigma(f, \vartheta) = 2\pi f\varepsilon_0\varepsilon''(f, \vartheta). \quad (4.2)$$

#### 4.1.2 Influences on the Acquisition of Temperature-Dependent Dielectric Properties

The accuracy of temperature-dependent dielectric spectroscopy (DSP) of tissues might be influenced by different factors. In this section, various potential influencing factors are investigated to determine reliable working conditions in terms of measuring temperature-dependent dielectric properties of tissues and blood.

##### Influence of Storage Time

First, the influence of the storage time, which is the time between excision and measurement of the MUT (tissue or blood), on the dielectric properties is investigated. Recent

studies have shown no significant difference in dielectric properties between *in vivo* and *ex vivo* measurements as reported by Peyman et al. [2005], Lazebnik et al. [2006], Farrugia et al. [2016]. Lazebnik et al. [2006] summarized that cell death has no significant influence on the dielectric properties at microwaves. Furthermore, it is postulated that some fluid loss and changes in oxygen tension, pH and temperature will occur after excision, whereby changes of the dielectric properties in the microwave frequency range are only expected due to fluid loss and temperature variations. Farrugia et al. [2016] also outlined that the differences between *in vivo* and *ex vivo* dielectric properties are caused by tissue hydration.

The aim of this section is not to investigate the differences between *in vivo* and *ex vivo* measurements of tissue, but to clarify whether the storage time has a significant influence on the dielectric properties. Therefore, fresh porcine tissue and blood were obtained from local slaughter houses. The samples were stored in a fridge between extraction and measurement. The dielectric properties were measured corresponding to the measurement setup presented in the previous section. In general, one and the same piece of tissue was measured only once in order to exclude denaturation effects. Therefore, several pieces of tissue from one animal were examined, whereby the storage time of them varied between a few hours and several days. Figure 4.3 shows the relative permittivity and effective conductivity of porcine tissue and blood as a function of frequency for different storage times. Considering the dielectric properties of liver as an example (see Figure 4.3(a,b)), curves of the same color show different samples from the same animal. This means that in the case of liver three different animals were analyzed and five different animals were examined for fat. A significant influence of the storage time on the dielectric properties would mainly result from the decreasing water content due to the progressive dehydration of the tissue. This effect would lead to continuously decreasing relative permittivity instead of a random behavior, as can be seen in Figure 4.3. For example, considering the results of muscle samples of different animals (see Figure 4.3(c,d)), the sample with the longest storage time of the first animal (blue dashed curves) shows the lowest permittivity and conductivity, whereby the two samples with the longest storage time of the second animal (red dashed curves) show the highest dielectric properties. Moreover, all measurements of the second animal (red curves) indicate significant differences between the samples without any correlation to the storage time, whereas the results of the third animal (green curves) show nearly no differences. The same irregular behavior can be seen in the curves of liver and fat (see Figure 4.3(a,b,e,f)). From these findings it can be concluded that the storage time itself cannot be the origin of these differences. The intra-individual tissue differences (permittivity differences between various samples of one tissue type of one animal due to the tissue inhomogeneity) as well as the inter-individual differences (permittivity differences between samples of one tissue type of different animals) are much more dominant than the

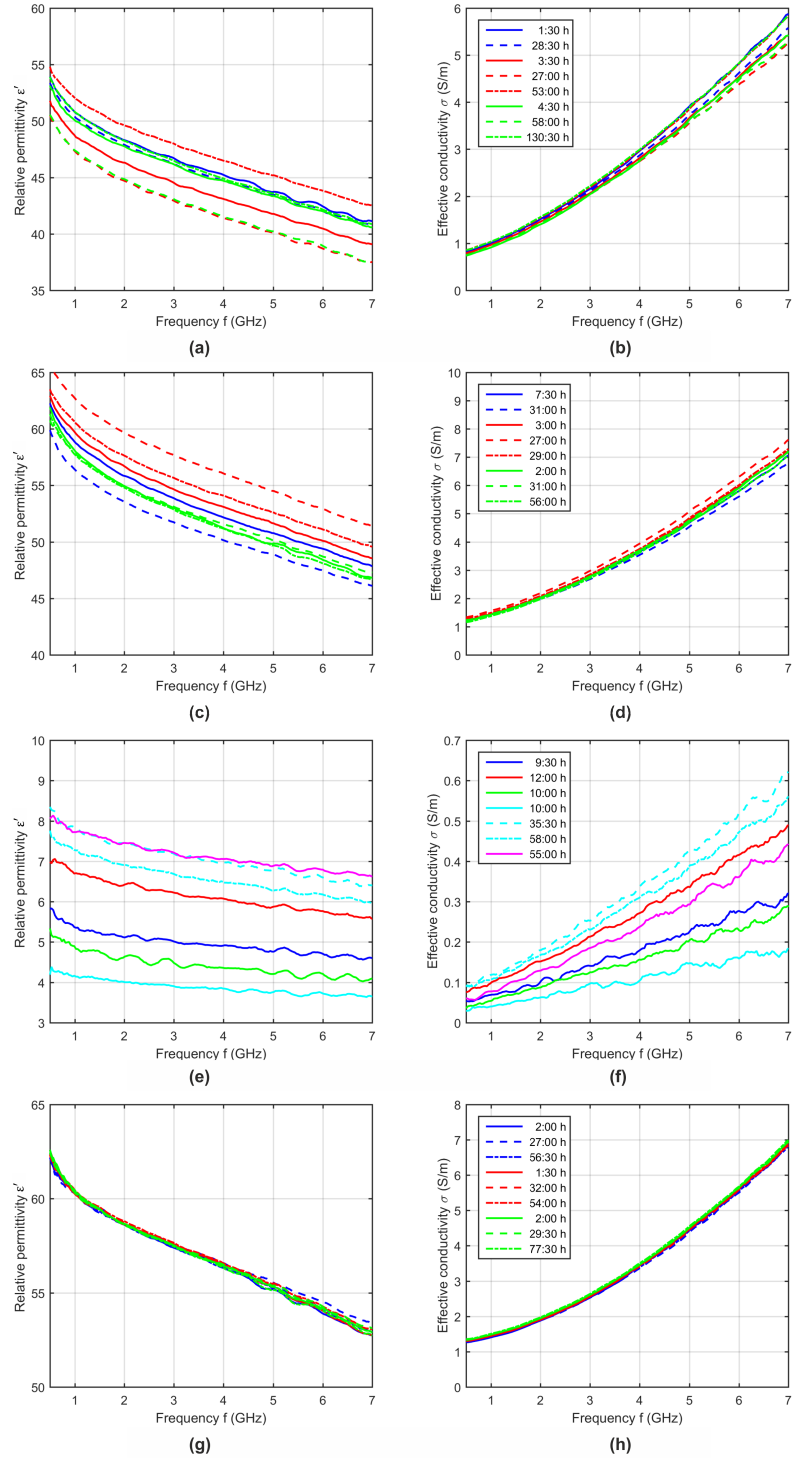


**Figure 4.3:** Relative permittivity and effective conductivity of (a,b) porcine liver, (c,d) muscle, (e,f) fat and (g,h) blood at 37°C as a function of frequency for different storage times. Each curve shows the dielectric properties of one sample, whereby curves of the same color indicate samples of the same animal.

influence of the storage time. These findings and the result that all blood measurements are nearly identical allow to average the measurements of one tissue type independently from the storage time.

### Influence of the Measurement Procedure

The detection of small temperature-dependent changes in permittivity and conductivity require reliable measurement conditions. Therefore, the dielectric properties of tissue were analyzed at a constant temperature depending on the measurement time, which means the time after coaxial probe positioning. Figure 4.4(a,b) shows exemplarily the relative permittivity and effective conductivity of one liver sample over a measurement time of 32 minutes with a measurement rate of two minutes. The curves show a non-linear increase of the dielectric properties over the measurement time. This effect also occurred with muscle and fat tissues. In contrast, the curves for blood show no change in permittivity and conductivity after immersing the probe into the blood as depicted in Figure 4.4(c,d). Based on these results, it seems that pressing the probe onto the tissue

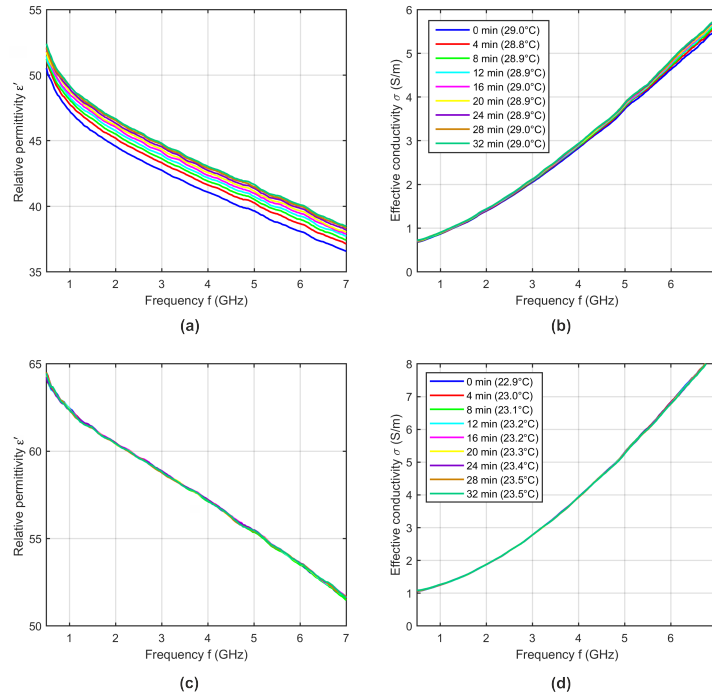


**Figure 4.4:** (a) Relative permittivity and (b) effective conductivity of one porcine liver sample as a function of frequency at a constant temperature over a time period of 32 minutes; (c) Relative permittivity and (d) effective conductivity of one porcine blood sample as a function of frequency at a constant temperature over a time period of 32 minutes. The blue curves indicate the measurement immediately after coaxial probe positioning.

samples causes a change in the dielectric properties. As a consequence, the temperature-dependent DSP of liver, muscle and fat started 30 minutes after probe positioning, because after this waiting time the changes of the dielectric properties were significantly lower. In general, these remaining minor changes should be minimized as much as possible, but it seems that they cannot be completely suppressed. It has to be noted that this error is almost negligible compared to the absolute permittivity and conductivity, but it can be significant compared to the temperature-dependent changes of the dielectric properties.

The temperature-dependent dielectric properties can be determined during heating or cooling cycle of the sample. Figure 4.5 shows the differences between both approaches using the example of porcine liver. Figure 4.5(a,d) illustrates the relative permittivity and effective conductivity at five distinct temperatures averaged over six samples during the heating cycle and Figure 4.5(b,e) shows the temperature-dependent dielectric properties averaged over six samples during the cooling cycle. The error bars indicate the standard deviation for some individual frequencies. The relative permittivity recorded during the heating cycle shows a lower temperature dependence compared to the data measured during the cooling cycle. In addition, both scenarios show an intersection, with the cross-over point occurring during heating measurements at 5.2 GHz and shifting to 7 GHz during cooling experiments. The effective conductivity shows an almost identical behavior between heating and cooling analysis with an intersection point at 2.8 GHz in both cases. Lazebnik et al. [2006] also described differences between heating and cooling cycles with the result that repeatable anomalies were recorded during the heating cycle. However, the reason for the permittivity and conductivity anomalies are not described in detail. Considering the results presented in Figure 4.5(a,b), it can be supposed that the pressure-dependent influence described above superimposes the temperature-dependent changes of the dielectric properties of tissue. It is expected that the relative permittivity decreases with increasing temperature due to the water content of the tissue. Considering the dielectric spectroscopy during heating cycle, the temperature-dependent decrease of the permittivity will be reduced by the pressure-dependent increase of the permittivity (see Figure 4.5(a)). In contrast, the pressure-dependent increase of the permittivity additionally raised the temperature-dependent increase of the permittivity during the cooling cycle measurement. To compensate for this effect, the relative permittivity and effective conductivity is computed by averaging the results over all samples including six measurements recorded during the heating and six measurements during the cooling cycle as shown in Figure 4.5(c,f). In addition, averaging the same number of heating and cooling measurements ensures that the slight influence of the mentioned pressure-dependent error, which persists after waiting 30 minutes after positioning the probe, is independent of temperature. This is important to obtain reliable temperature-dependent dielectric properties



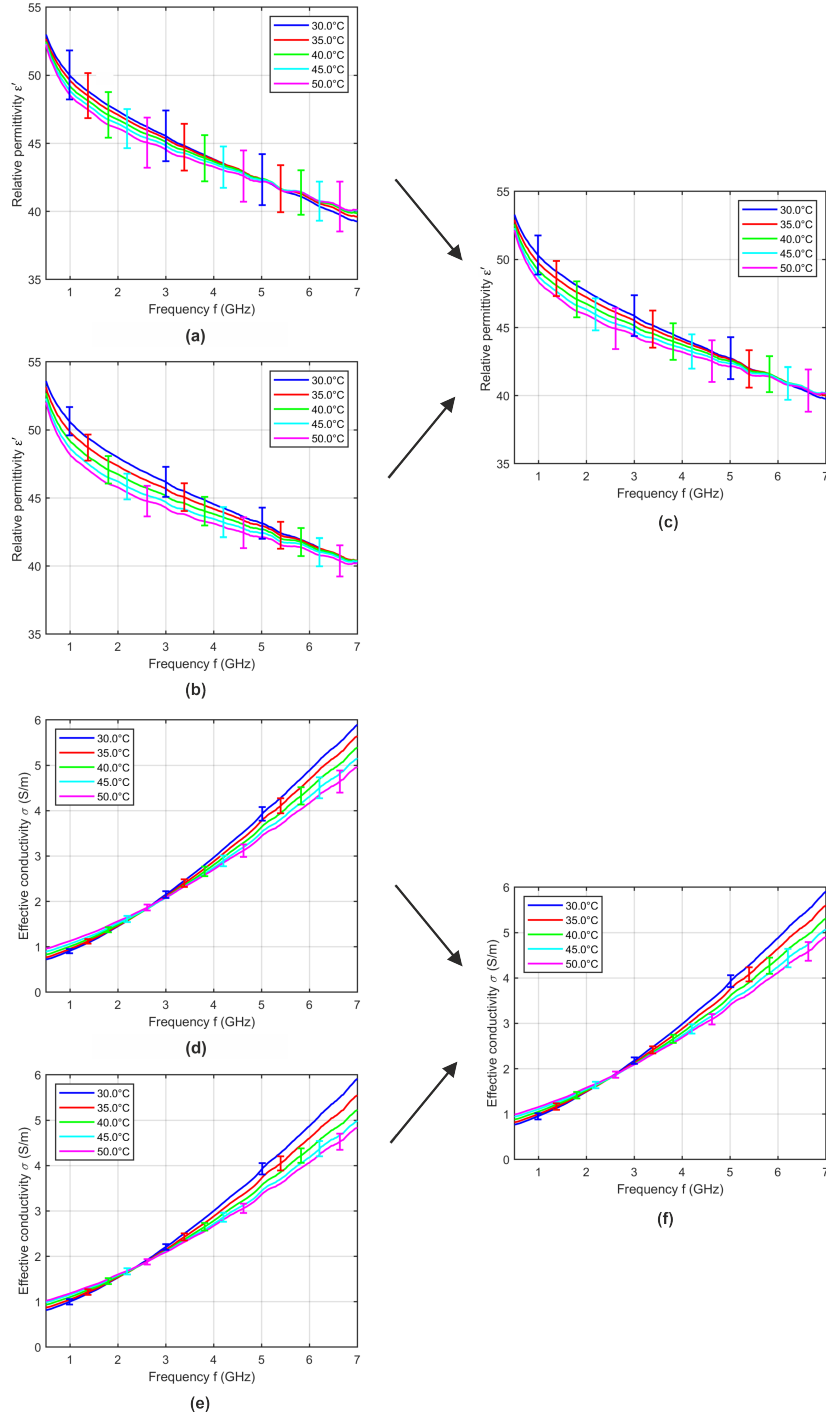


**Figure 4.5:** Mean relative permittivity and mean effective conductivity of six porcine liver samples acquired during (a,d) heating and (b,e) cooling cycle as a function of frequency at different temperatures; (c,f) Mean relative permittivity and mean effective conductivity of 12 porcine liver samples including six heating and six cooling measurements. Error bars indicate the corresponding standard deviation.

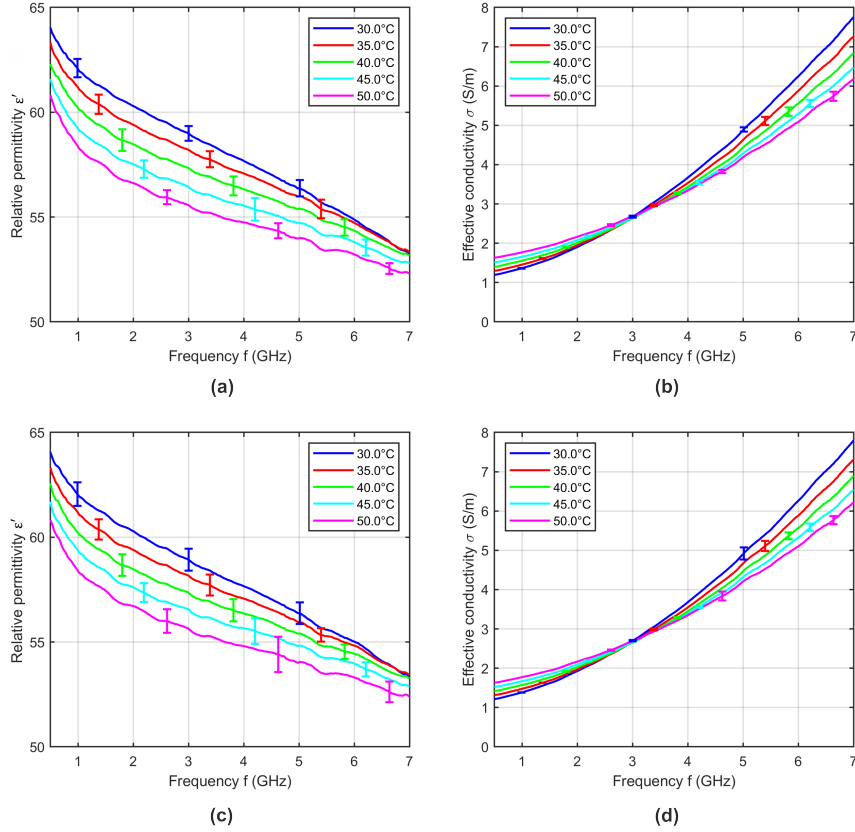


**Figure 4.6:** Mean relative permittivity and mean effective conductivity of three porcine blood samples acquired during (a,b) heating and (c,d) cooling cycle as a function of frequency at different temperatures. Error bars indicate the corresponding standard deviation.

of tissues. The procedure is applied to determine the temperature-dependent dielectric properties of liver, muscle and fat.

In contrast to soft tissue, the DSP measurements of blood did not show a pressure-dependent error. For this reason, the temperature-dependent measurements began immediately after immersing the probe into the liquid. Figure 4.6 shows the relative permittivity and effective conductivity of blood averaged over three samples measured during heating and three samples during cooling with the corresponding standard deviation indicated by the error bars. On the contrary to soft tissue, blood shows no differences between both cycles. Due to this finding, the temperature-dependent dielectric properties of blood were recorded during sample heating.

### 4.1.3 Temperature-Dependent Cole-Cole Model

In this section, a parametric model is introduced to calculate the relative permittivity and effective conductivity at any temperature and frequency in the specified ranges. Such a model reduces the size of the measured data set, since only a few parameters are required to calculate the temperature-dependent dielectric properties. The frequency-dependent dielectric properties of tissue are dominated by three relaxation regions,  $\alpha$ ,  $\beta$ , and  $\gamma$  occurring in the low, medium and high frequency range as described in Section 2.4. Gabriel et al. [1996c] presented a model to describe the spectrum over a wide frequency range from 10 Hz to 100 GHz. They introduced a Cole-Cole model consisting of four poles ( $n = 4$ ) corresponding to Equation (2.27) in order to determine the relative complex permittivity for different kinds of tissues at one temperature.

In contrast, the frequency range considered in this study is between 0.5 GHz and 7 GHz, in which the dielectric properties are mainly characterized by the  $\gamma$  dispersion. Since the dispersion regions frequently overlap as described by Foster and Schwan [1996], a two-pole Cole-Cole model is used to fit the data in this frequency range. According to Equation (2.27) with  $n = 2$  the frequency- and temperature-dependent relative complex permittivity is determined by

$$\varepsilon(f, \vartheta) = \varepsilon_{\infty}(\vartheta) + \frac{\Delta\varepsilon_1(\vartheta)}{1 + (i2\pi f\tau_1(\vartheta))^{1-\alpha_1}} + \frac{\Delta\varepsilon_2(\vartheta)}{1 + (i2\pi f\tau_2(\vartheta))^{1-\alpha_2}} + \frac{\sigma_s(\vartheta)}{i2\pi f\varepsilon_0}. \quad (4.3)$$

Figure 4.7 shows the principle of the fitting procedure. In the first step, the initial values

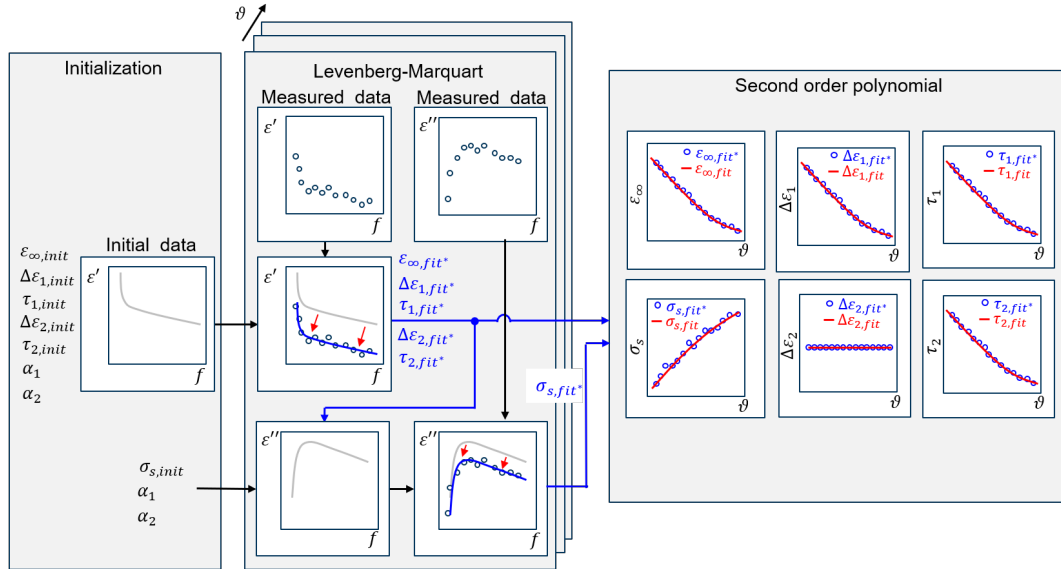


**Figure 4.7:** Schematic of the fitting procedure.

$\varepsilon_{\infty,init}$ ,  $\Delta\varepsilon_{1,init}$ ,  $\Delta\varepsilon_{2,init}$ ,  $\tau_{1,init}$ ,  $\tau_{2,init}$  and  $\sigma_{s,init}$  are set to the data presented by Gabriel et al. [1996c]. The parameters  $\alpha_1$  and  $\alpha_2$  are set to a constant value for each tissue to limit the number of fitting parameters. After initialization, the Levenberg-Marquart algorithm is applied to fit the Cole-Cole parameters to the experimental data for each temperature corresponding to Equation (4.3). First, the real part of the complex permittivity  $\varepsilon'$  is fitted by adapting the Cole Cole parameters  $\varepsilon_{\infty,fit*}$ ,  $\Delta\varepsilon_{1,fit*}$ ,  $\Delta\varepsilon_{2,fit*}$ ,  $\tau_{1,fit*}$  and  $\tau_{2,fit*}$  iteratively until the mean absolute error (the difference between the modeled and measured relative permittivity) across the specified frequency range is minimized. After this, the imaginary part of the complex permittivity  $\varepsilon''$  is fitted. The input parameters are the initial values  $\sigma_{s,init}$ ,  $\alpha_1$  and  $\alpha_2$  as well as the Cole-Cole parameters of the real part fitting procedure. Based on this,  $\sigma_{s,fit*}$  is calculated by minimizing the mean absolute difference between the modeled and measured relative dielectric loss across all frequency points. As mentioned above, the Levenberg-Marquart fitting procedure is applied for each temperature resulting in a data set of six Cole-Cole parameters ( $\varepsilon_{\infty,fit*}$ ,  $\Delta\varepsilon_{1,fit*}$ ,  $\Delta\varepsilon_{2,fit*}$ ,  $\tau_{1,fit*}$ ,  $\tau_{2,fit*}$  and  $\sigma_{s,fit*}$ ) per temperature, which is illustrated in Figure 4.7. In the final step, a second order polynomial is applied to fit the temperature-dependent Cole-Cole parameters corresponding to

$$\begin{aligned}
 \varepsilon_{\infty,fit}(\vartheta) &= A_1\vartheta^2 + B_1\vartheta + C_1 \\
 \Delta\varepsilon_{1,fit}(\vartheta) &= A_2\vartheta^2 + B_2\vartheta + C_2 \\
 \tau_{1,fit}(\vartheta) &= A_3\vartheta^2 + B_3\vartheta + C_3 \\
 \Delta\varepsilon_{2,fit}(\vartheta) &= A_4\vartheta^2 + B_4\vartheta + C_4 \\
 \tau_{2,fit}(\vartheta) &= A_5\vartheta^2 + B_5\vartheta + C_5 \\
 \sigma_{s,fit}(\vartheta) &= A_6\vartheta^2 + B_6\vartheta + C_6,
 \end{aligned} \tag{4.4}$$

which is also suggested by Lazebnik et al. [2006]. The coefficients  $A_k, B_k, C_k$  ( $k = 1...6$ ) for the different tissues are presented in the following sections.

Finally, the temperature-dependent dielectric properties can be computed by

$$\begin{aligned}
 \underline{\varepsilon}_{fit}(f, \vartheta) &= \varepsilon'_{fit}(f, \vartheta) - i\varepsilon''_{fit}(f, \vartheta) \\
 &= \varepsilon_{\infty,fit}(\vartheta) + \frac{\Delta\varepsilon_{1,fit}(\vartheta)}{1 + (i2\pi f\tau_{1,fit}(\vartheta))^{1-\alpha_1}} + \frac{\Delta\varepsilon_{2,fit}(\vartheta)}{1 + (i2\pi f\tau_{2,fit}(\vartheta))^{1-\alpha_2}} + \frac{\sigma_{s,fit}(\vartheta)}{i2\pi f\varepsilon_0}.
 \end{aligned} \tag{4.5}$$

To quantify the quality of the fitting procedure, the difference between the measured data and the results derived by the temperature-dependent two-pole Cole-Cole model

corresponding to Equation (4.5) is analyzed by

$$\begin{aligned}\delta\varepsilon'_{measured,fit}(f, \vartheta) &= \varepsilon'_{measured}(f, \vartheta) - \varepsilon'_{fit}(f, \vartheta) \\ \delta\sigma_{measured,fit}(f, \vartheta) &= \sigma_{measured}(f, \vartheta) - \sigma_{fit}(f, \vartheta)\end{aligned}\tag{4.6}$$

with  $\sigma_{fit}(f, \vartheta) = 2\pi f\varepsilon_0\varepsilon''_{fit}(f, \vartheta)$ .

#### 4.1.4 Results of Temperature-Dependent Dielectric Spectroscopy

In this section the temperature-dependent dielectric properties of liver, muscle, fat and blood are presented. The results are determined by the introduced temperature-dependent two-pole Cole-Cole model (see Section 4.1.3). Due to the findings of Section 4.1.2, the fitting procedure is applied to the mean relative permittivity and mean effective conductivity over all samples for each tissue and blood.

##### Liver

The temperature-dependent Cole-Cole parameters for liver are determined on the basis of the averaged measurements as shown in Figure 4.5(c,f). The empirical distribution parameters  $\alpha_1$  and  $\alpha_2$  are set to 0.2. Figure 4.8 shows the modeled Cole-Cole parameters (blue circles) as a function of temperature and the corresponding second order polynomial fit (red curves). The coefficients of the quadratic fit are given by Table 4.1.

Figure 4.9 shows exemplarily five curves of the relative permittivity and effective conduc-

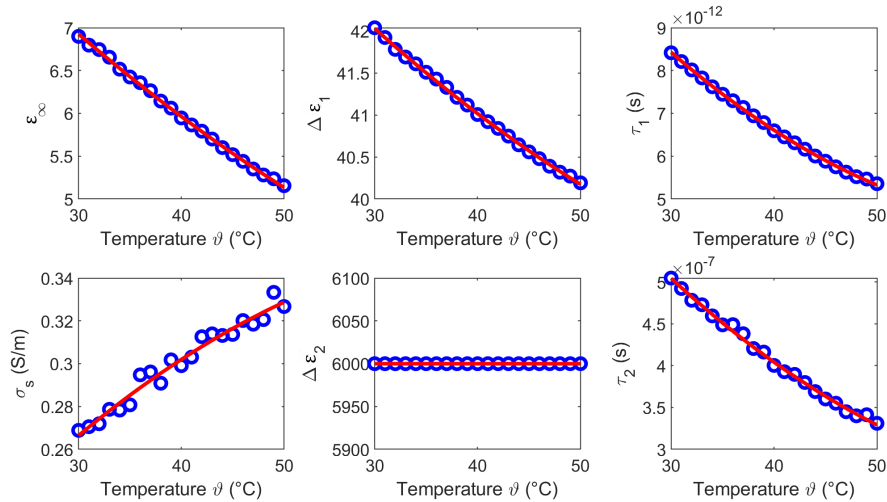


**Figure 4.8:** Temperature-dependent Cole-Cole parameters (blue circles) of liver and the corresponding second order polynomial fit (red curves).

**Table 4.1:** Tissue-dependent coefficients of the second order polynomial fit of liver.

	$k$	$A_k$		$B_k$		$C_k$	
$\varepsilon_{\infty,fit}$	1	$0.6634 \cdot 10^{-3}$	(K <sup>-2</sup> )	-0.1427	(K <sup>-1</sup> )	10.61	
$\Delta\varepsilon_{1,fit}$	2	$0.8595 \cdot 10^{-3}$	(K <sup>-2</sup> )	-0.1616	(K <sup>-1</sup> )	46.10	
$\tau_{1,fit}$	3	2.693	(fs · K <sup>-2</sup> )	-0.3705	(ps · K <sup>-1</sup> )	17.12	(ps)
$\Delta\varepsilon_{2,fit}$	4	0	(K <sup>-2</sup> )	0	(K <sup>-1</sup> )	6000	
$\tau_{2,fit}$	5	0.1259	(ns · K <sup>-2</sup> )	-18.83	(ns · K <sup>-1</sup> )	955.8	(ns)
$\sigma_{s,fit}$	6	-0.0436	(mS · K <sup>-2</sup> )	6.603	(mS · K <sup>-1</sup> )	107.6	(mS)

tivity determined by Equation (4.5) with the temperature-dependent Cole-Cole parameters computed by Equation (4.4) and the temperature coefficients summarized in Table 4.1.

The relative permittivity shows a decreasing trend over the frequency range, whereby the effective conductivity increases towards higher frequencies. These results are consistent with the dielectric properties at 37 °C presented by Lazebnik et al. [2006] and Gabriel et al. [1996c]. The modeled temperature-dependent relative permittivity curves have a cross-over point at 6 GHz. Below this point, the relative permittivity decreases with increasing temperature, whereas this trend reverses at frequencies above 6 GHz. The effective conductivity also has an intersection point in the observed frequency range at 3 GHz. The conductivity rises up with increasing temperature below 3 GHz and this dependence reverses at frequencies above the cross-over point. The observed temperature dependen-

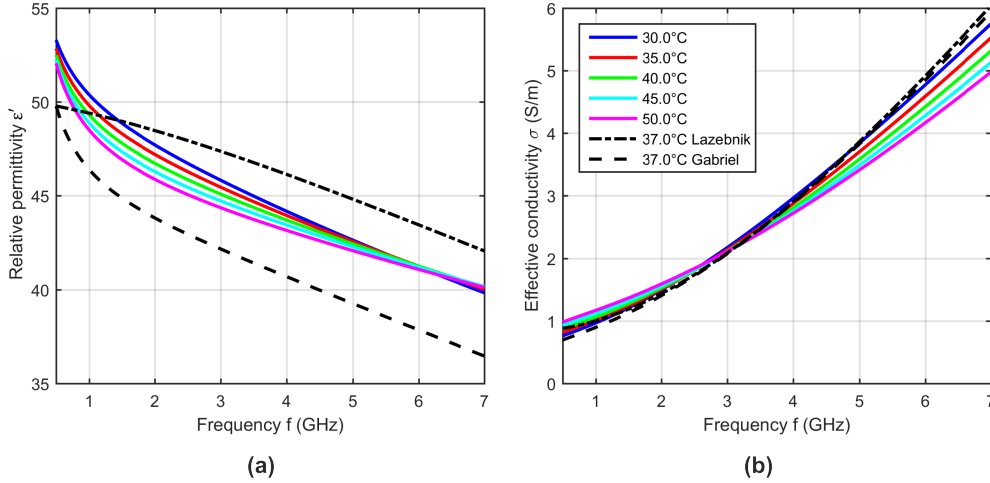


**Figure 4.9:** (a) Relative permittivity and (b) effective conductivity of porcine liver as a function of frequency at five different temperatures determined by the two-pole Cole-Cole model based on the derived temperature-dependent Cole-Cole parameters. Black curves show the dielectric properties of liver at 37 °C reported by Lazebnik et al. [2006] for bovine and Gabriel et al. [1996c] for ovine.

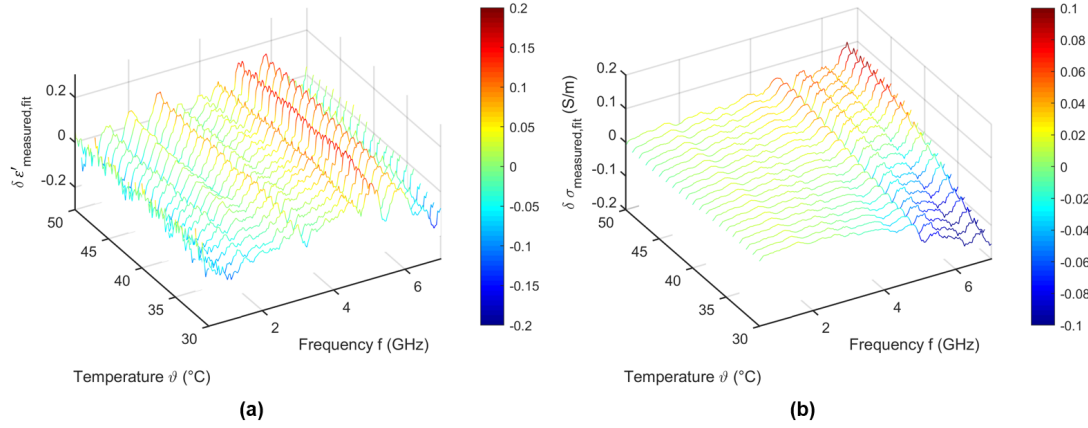


**Figure 4.10:** Difference between the measured data and the temperature-dependent two-pole Cole-Cole model of (a) relative permittivity and (b) effective conductivity of porcine liver.

cies are in agreement with the results reported by Lazebnik et al. [2006].

To quantify the quality of the introduced two-pole Cole-Cole model, Figure 4.10 shows the difference between the measured values and the modeled data corresponding to Equation (4.6). The fitted curves are largely consistent with the experimental data. The deviations of the relative permittivity are lower than 0.2. The variations concerning the effective conductivity show slight differences to the measured data in the high frequency range for temperatures between 30 °C and 35 °C.

## Muscle

The temperature-dependent Cole-Cole parameters for muscle corresponding to the measured data are shown in Figure 4.11, whereby  $\alpha_1$  and  $\alpha_2$  are set to 0.18. The circles represent the temperature-dependent Cole-Cole coefficients and the solid curves indicate the corresponding quadratic fit. The coefficients of the second order polynomial fit are summarized in Table 4.2. Figure 4.12 shows exemplarily five curves of the relative permittivity and effective conductivity calculated by the two-pole Cole-Cole model (see Equation (4.5)) with the temperature-dependent Cole-Cole parameters computed by Equation (4.4) and the temperature coefficients given by Table 4.2. The results are within the range of the relative permittivity and effective conductivity at 37 °C presented by Gabriel et al. [1996c]. Furthermore, the temperature-dependent dielectric properties show similarities with the results of liver. The relative permittivity decreases towards higher frequencies and the effective conductivity shows an opposite curve shape. Considering the temperature dependence, both the relative permittivity and the effective conductivity have an intersection point in the considered frequency range, where the dielectric properties do not change

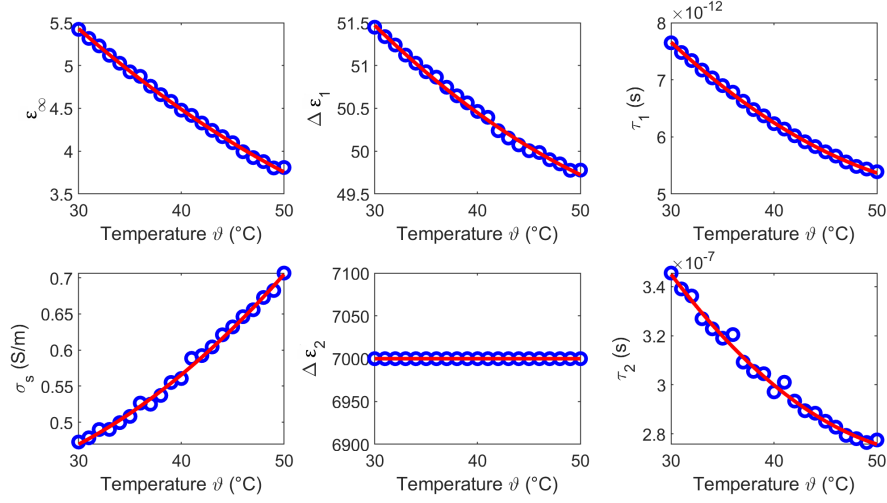


**Figure 4.11:** Temperature-dependent Cole-Cole parameters (blue circles) of muscle and the corresponding second order polynomial fit (red curves).

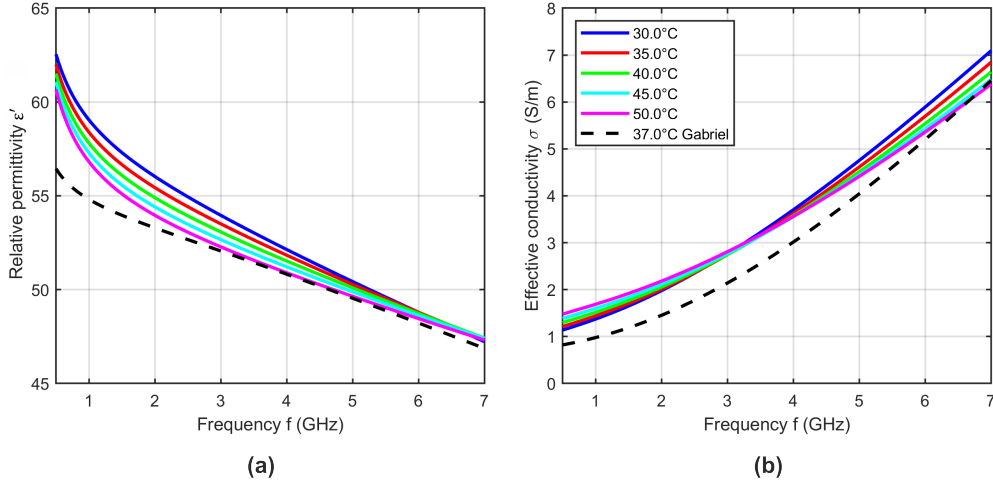
**Table 4.2:** Tissue-dependent coefficients of the second order polynomial fit of muscle.

	$k$	$A_k$		$B_k$		$C_k$	
$\varepsilon_{\infty,fit}$	1	$1.047 \cdot 10^{-3}$	(K <sup>-2</sup> )	-0.1675	(K <sup>-1</sup> )	9.513	
$\Delta\varepsilon_{1,fit}$	2	$1.495 \cdot 10^{-3}$	(K <sup>-2</sup> )	-0.2068	(K <sup>-1</sup> )	56.33	
$\tau_{1,fit}$	3	2.651	(fs · K <sup>-2</sup> )	-0.3266	(ps · K <sup>-1</sup> )	15.07	(ps)
$\Delta\varepsilon_{2,fit}$	4	0	(K <sup>-2</sup> )	0	(K <sup>-1</sup> )	7000	
$\tau_{2,fit}$	5	0.1053	(ns · K <sup>-2</sup> )	-11.89	(ns · K <sup>-1</sup> )	606.8	(ns)
$\sigma_{s,fit}$	6	0.2140	(mS · K <sup>-2</sup> )	-5.352	(mS · K <sup>-1</sup> )	437.5	(mS)

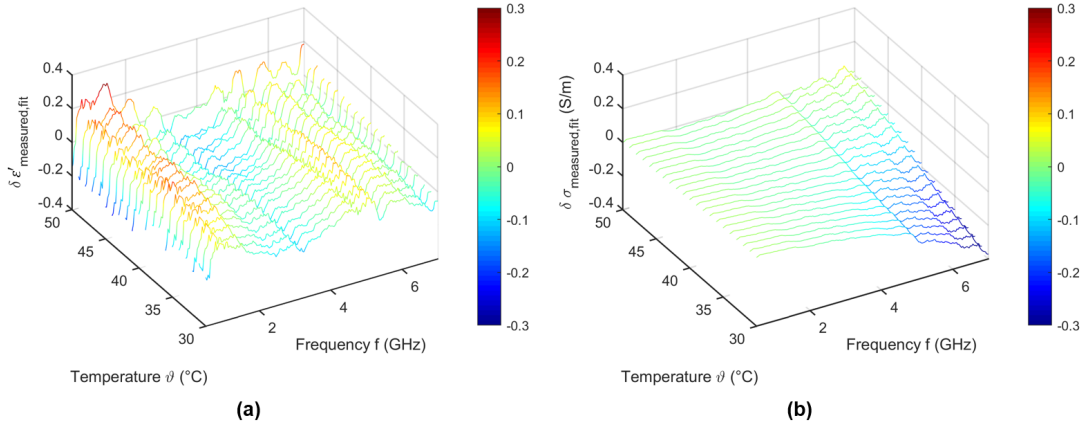
with temperature. The relative permittivity decreases with increasing temperature below the cross-over point at 6.5 GHz. The effective conductivity rises up with increasing temperature below the intersection point at 3 GHz. The trend reverses in both cases for frequencies above the corresponding cross-over point.

Figure 4.13 shows the difference between the measured and the modeled data corresponding to Equation (4.6). The fitted curves agree with the experimental data. The deviations of the relative permittivity are lower than 0.3. The results of the fitting procedure concerning the effective conductivity show slight differences to the measured data in the high frequency range for temperatures between 30 °C and 35 °C.





**Figure 4.12:** (a) Relative permittivity and (b) effective conductivity of porcine muscle as a function of frequency at different temperatures. Black curves show the dielectric properties of muscle reported by Gabriel et al. [1996c] at 37 °C.



**Figure 4.13:** Difference between the measured and the temperature-dependent two-pole Cole-Cole model of (a) relative permittivity and (b) effective conductivity of porcine muscle.

## Fat

Figure 4.14 shows the temperature-dependent Cole-Cole parameters for fat corresponding to the experimental data with  $\alpha_1$  and  $\alpha_2$  are set to 0.4. The circles show the temperature-dependent Cole-Cole parameters and the solid curves indicate the corresponding quadratic fit. The coefficients of the second order polynomial fit are summarized in Table 4.3. Figure 4.15 shows exemplarily five curves of the relative permittivity and effective conductivity computed by the two-pole Cole-Cole model (see Equation (4.5)) with the temperature-dependent Cole-Cole parameters determined by Equation (4.4) and the temperature coef-

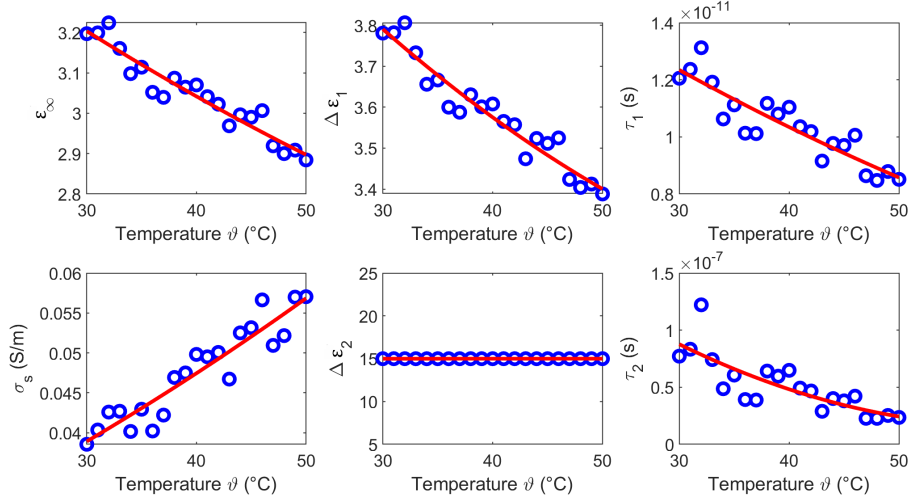


**Figure 4.14:** Temperature-dependent Cole-Cole parameters (blue circles) of fat and the corresponding second order polynomial fit (red curves).

**Table 4.3:** Tissue-dependent coefficients of the second order polynomial fit of fat.

	$k$	$A_k$		$B_k$		$C_k$
$\varepsilon_{\infty,fit}$	1	$0.0845 \cdot 10^{-3}$	( $K^{-2}$ )	$-0.0221$	( $K^{-1}$ )	3.789
$\Delta\varepsilon_{1,fit}$	2	$0.2014 \cdot 10^{-3}$	( $K^{-2}$ )	$-0.0356$	( $K^{-1}$ )	4.679
$\tau_{1,fit}$	3	1.163	( $fs \cdot K^{-2}$ )	$-0.2815$	( $ps \cdot K^{-1}$ )	19.74 (ps)
$\Delta\varepsilon_{2,fit}$	4	0	( $K^{-2}$ )	$-0.0002$	( $K^{-1}$ )	15.00
$\tau_{2,fit}$	5	0.0779	( $ns \cdot K^{-2}$ )	$-9.398$	( $ns \cdot K^{-1}$ )	299.5 (ns)
$\sigma_{s,fit}$	6	0.0043	( $mS \cdot K^{-2}$ )	0.5504	( $mS \cdot K^{-1}$ )	18.50 (mS)

ficients given by Table 4.3. The relative permittivity is almost constant over the considered frequency range and the effective conductivity raises towards higher frequencies, which is consistent with the data shown by Gabriel et al. [1996c]. Furthermore, the permittivity decreases slightly with increasing temperature. The effective conductivity rises up with increasing temperature at low frequencies and shows nearly no temperature dependence in the higher frequency range.

Figure 4.16 shows the difference between the experimental data and the modeled data corresponding to Equation (4.6). The variations between fitted and measured data are lower than 0.15 for the relative permittivity and less than 0.02 for the effective conductivity.

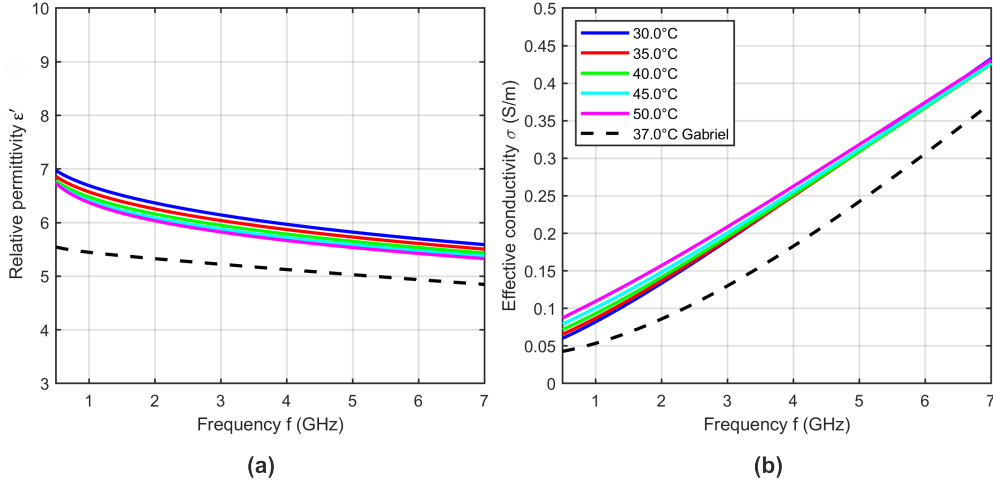


**Figure 4.15:** (a) Relative permittivity and (b) effective conductivity of porcine fat as a function of frequency at different temperatures. Black curves show the dielectric properties of fat reported by Gabriel et al. [1996c] at 37 °C.

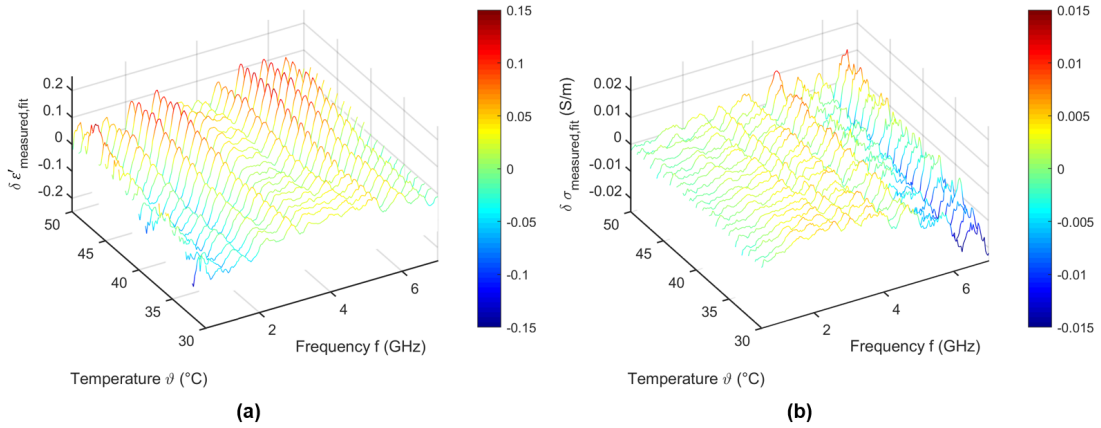


**Figure 4.16:** Difference between the measured data and the temperature-dependent two-pole Cole-Cole model of (a) relative permittivity and (b) effective conductivity of porcine fat.

## Blood

The temperature-dependent Cole-Cole parameters for blood based on the measured data are shown in Figure 4.17, whereby  $\alpha_1$  and  $\alpha_2$  are set to 0.1. The circles indicate the Cole-Cole coefficients as a function of temperature and the red curves show the corresponding second order polynomial fit. The coefficients of the quadratic fit are summarized in Table 4.4. Figure 4.18 shows five curves of the relative permittivity and effective conductivity determined by Equation (4.5) with the temperature-dependent Cole-Cole parameters calculated by Equation (4.4) and the temperature coefficients presented in Table 4.4. The

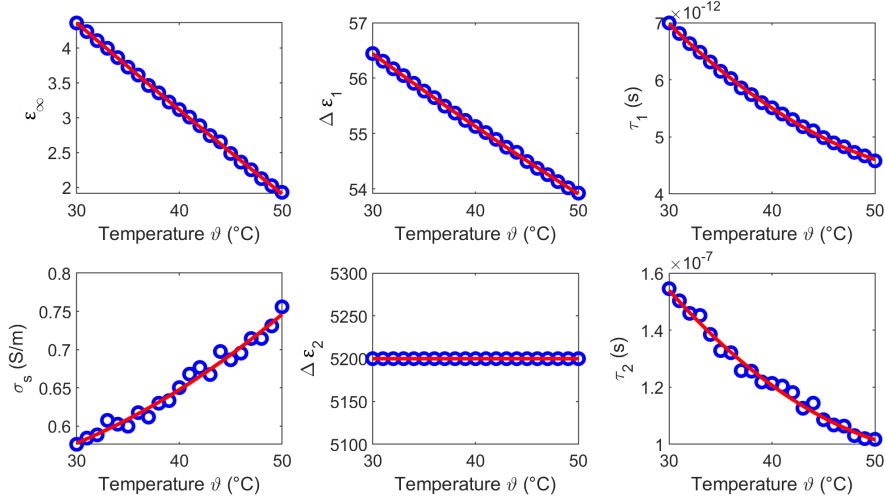


**Figure 4.17:** Temperature-dependent Cole-Cole parameters (blue circles) of blood and the corresponding second order polynomial fit (red curves).

**Table 4.4:** Tissue-dependent coefficients of the second order polynomial fit of blood.

	$k$	$A_k$		$B_k$		$C_k$
$\varepsilon_{\infty,fit}$	1	$0.2158 \cdot 10^{-3}$	(K <sup>-2</sup> )	-0.1399	(K <sup>-1</sup> )	8.362
$\Delta\varepsilon_{1,fit}$	2	$0.4829 \cdot 10^{-3}$	(K <sup>-2</sup> )	-0.1652	(K <sup>-1</sup> )	60.96
$\tau_{1,fit}$	3	2.865	(fs · K <sup>-2</sup> )	-0.3479	(ps · K <sup>-1</sup> )	14.84 (ps)
$\Delta\varepsilon_{2,fit}$	4	0	(K <sup>-2</sup> )	0	(K <sup>-1</sup> )	5200
$\tau_{2,fit}$	5	0.0712	(ns · K <sup>-2</sup> )	-8.314	(ns · K <sup>-1</sup> )	339.2 (ns)
$\sigma_{s,fit}$	6	0.1434	(mS · K <sup>-2</sup> )	-3.063	(mS · K <sup>-1</sup> )	540.6 (mS)

relative permittivity decreases over the frequency range whereas the effective conductivity rises towards higher frequencies. The curves show slight variations in slope compared to the data presented by Gabriel et al. [1996c], but the dielectric properties are within the same range. The relative permittivity decreases with increasing temperature, whereby it is noticeable that the temperature dependence at higher frequencies is nonlinear. This trend is comparable to the temperature-dependent relative permittivity of water as shown by Kaatz [1989], Ellison [2007]. The effective conductivity increases with rising temperature at frequencies below the intersection point at 3 GHz. This behavior reverses at frequencies above the cross-over point and is in accordance with the results presented by Wolf et al. [2011].

Figure 4.19 shows the difference between the measured data and the temperature-dependent Cole-Cole model corresponding to Equation (4.6). The fitted data are consistent with the measured ones. The variations of the relative permittivity are lower than

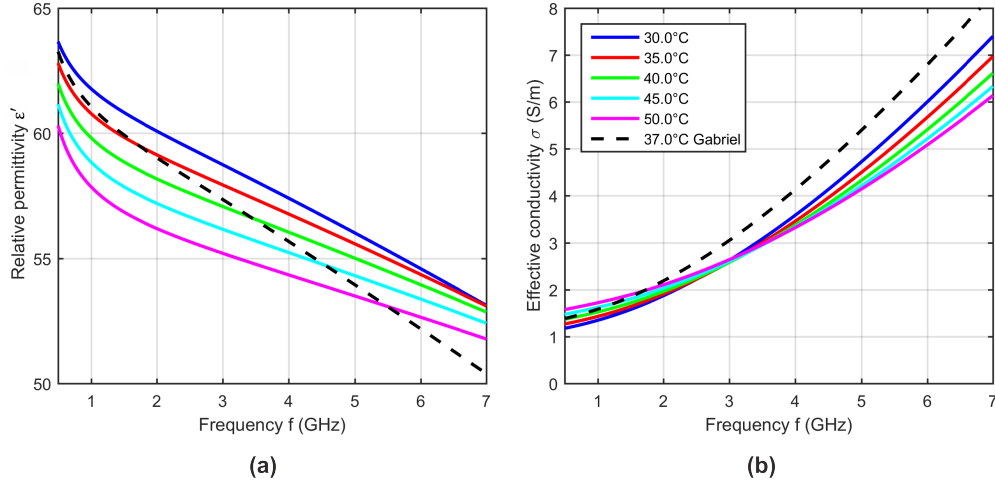


**Figure 4.18:** (a) Relative permittivity and (b) effective conductivity of porcine blood as a function of frequency at different temperatures. Black curves show the dielectric properties of blood at 37°C reported by Gabriel et al. [1996c].

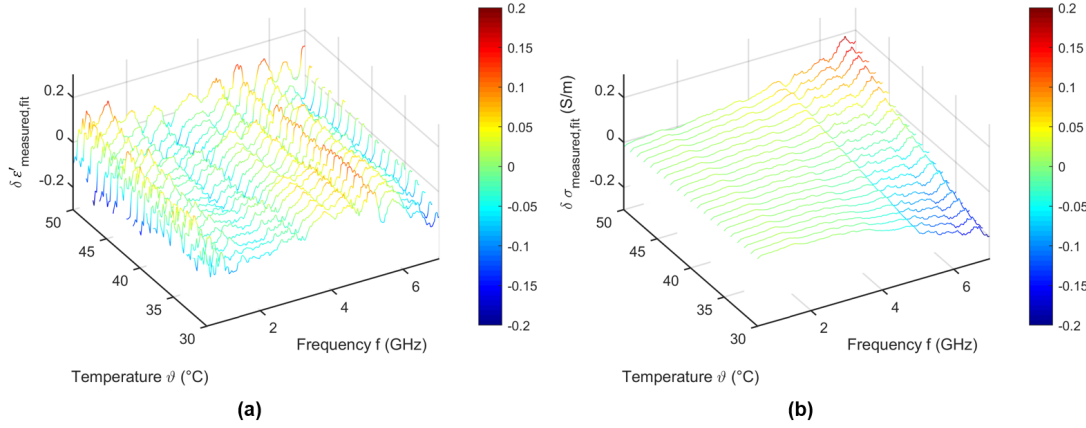


**Figure 4.19:** Difference between the measured data and the temperature-dependent two-pole Cole-Cole model of (a) relative permittivity and (b) effective conductivity of porcine blood.

0.2 and the deviations in terms of the effective conductivity show slight differences to the measured data in the high frequency range.

## 4.2 Noninvasive Detection of Temperature Changes by Means of UWB Microwave Radar

This section is motivated by the previously presented results of the temperature-dependent DSP of tissues. The measurements showed that the relative permittivity and the effective conductivity vary with temperature in the considered microwave frequency range, which is fundamental for the UWB temperature monitoring approach as depicted in Figure 4.1. Due to these findings, this section investigates the feasibility of detecting temperature changes noninvasively by means of UWB pseudo-noise sensing. Therefore, an experimental measurement setup with a phantom consisting of two materials is analyzed. Furthermore, a modelling approach based on the reflection coefficient is derived in order to evaluate the differences in the measured radar signals. The experimental setup, the results of the investigations as well as the modeling approach correspond to Ley et al. [2018b].

The measurement setup consisted of a phantom container filled with sunflower oil in which a test tube filled with 12 ml of distilled water (target) was positioned (see Figure 4.20). One transmitting antenna (Tx) and four receiving antennas (Rx) were used to detect the small temperature changes of the target. The antennas were in direct contact with the oil and were connected to an UWB multiple-in and multiple-out (MIMO) system with a 9th order M-sequence and a 13 GHz clock rate. The radar system was controlled by

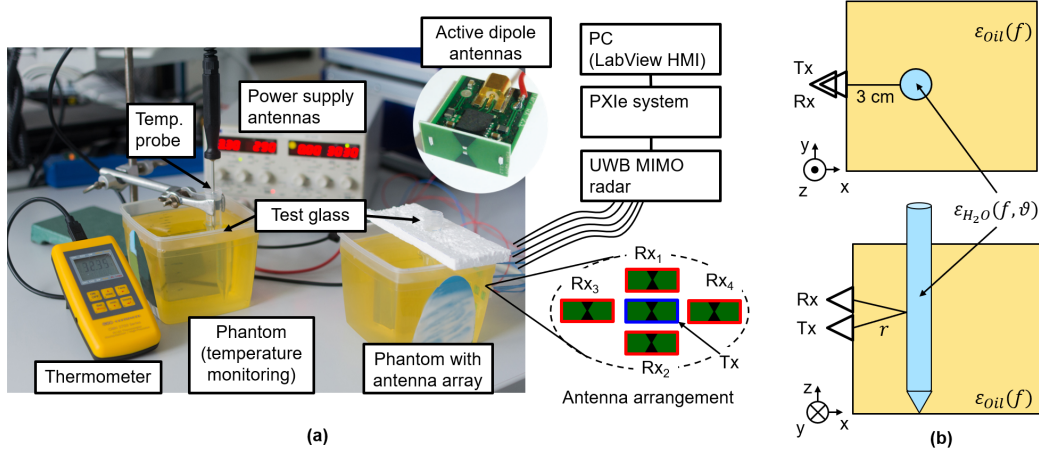


**Figure 4.20:** Measurement setup for temperature change detection by means of UWB pseudo-noise sensing; (a) Laboratory setup where two phantoms are filled with sunflower oil and each of them contains a test glass (target) filled with distilled water. A temperature probe is placed inside of the target of the left phantom in order to monitor the temperature. The phantom box on the right side acts as antenna array. The active dipole antennas are connected to an UWB MIMO system, which is controlled by a PXIe system and a LabVIEW Human Machine Interface (HMI); (b) Corresponding schematic of the setup for one UWB channel.

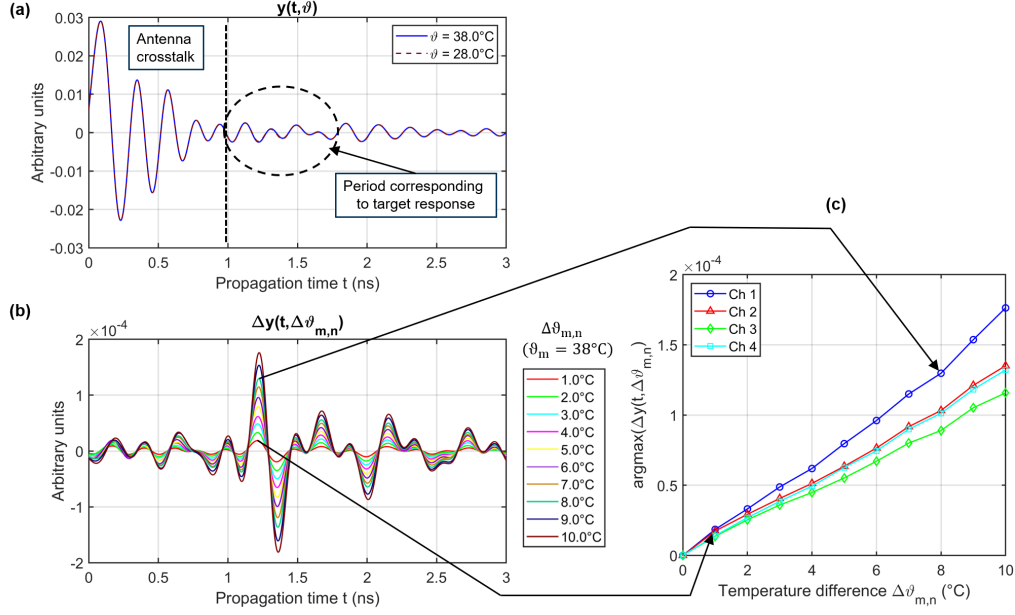
a PXIe system (National Instruments) and a LabVIEW Human Machine Interface (HMI) as presented by Helbig et al. [2017]. A second phantom container without antennas was used to monitor the temperature. It was also filled with sunflower oil and an identical target was placed inside. A temperature probe connected to a precision thermometer (GHM 3750, GHM Messtechnik GmbH, Regenstauf, Germany) was used to acquire the water temperature. The sunflower oil had an almost constant temperature ( $\approx 22^\circ\text{C}$ ) during the measurement procedure. The initial temperature of the distilled water in both targets was  $40^\circ\text{C}$  and the UWB signals were measured during the cooling down process in steps of  $1^\circ\text{C}$ . The decreasing water temperature leads to a change in the dielectric properties and thus to a changing reflection coefficient between the target (distilled water) and the surrounding medium (sunflower oil). The cooling process of water can slightly increase the temperature of the surrounding medium, but due to the almost temperature-independent complex permittivity of sunflower oil as presented in Ley et al. [2018b], a small temperature change of the surrounding medium does not affect the UWB signal. Consequently, the changing reflection coefficient at the boundary between the target and the surrounding medium depends only on the temperature change of distilled water.

Figure 4.20(b) shows the measurement scenario for one channel where the temperature changes can be detected by a differential measurement according to Equation (2.23). In terms of temperature monitoring, the contrast parameter  $\zeta$  will be replaced by the temperature and the differential signal is defined by

$$\begin{aligned}\Delta y(t, \Delta\vartheta_{m,n}) &= y(t, \vartheta_m) - y(t, \vartheta_n) \\ &= y_0(t) * [\Gamma_\vartheta(t, \vartheta_m) - \Gamma_\vartheta(t, \vartheta_n)] = y_0(t) * \Delta\Gamma_\vartheta(t, \Delta\vartheta_{m,n})\end{aligned}\quad (4.7)$$

where  $\vartheta_m$  and  $\vartheta_n$  are the temperatures of the target (distilled water). Figure 4.21(a) shows exemplarily two measured raw IRFs for a water temperature of  $38^\circ\text{C}$  and  $28^\circ\text{C}$ , respectively. The differential signals  $\Delta y(t, \Delta\vartheta_{m,n})$  for  $\vartheta_m = 38^\circ\text{C}$  and  $\vartheta_n = 37^\circ\text{C} \dots 28^\circ\text{C}$  are depicted in Figure 4.21(b) where the amplitude increases linearly with the temperature difference  $\Delta\vartheta_{m,n}$ . The linear increase is also valid for the other channels, as illustrated in Figure 4.21(c). It shows the maximum amplitude of the differential signals as a function of the temperature difference. The curves show slight differences in slope due to the fact that the temperature independent part of the measured target response  $y_{tar}(t, \vartheta)$  (see Equation 2.22) is channel-dependent. The linear dependence can be explained by the changing reflection coefficient. In order to demonstrate the temperature-dependent influence of the reflection coefficient, Equation (4.7) is converted to the frequency domain:

$$\Delta Y(f, \Delta\vartheta_{m,n}) = Y_0(f) \cdot \underbrace{[\underline{\Gamma}_\vartheta(f, \vartheta_m) - \underline{\Gamma}_\vartheta(f, \vartheta_n)]}_{=\Delta\underline{\Gamma}_\vartheta(f, \Delta\vartheta_{m,n})}. \quad (4.8)$$



**Figure 4.21:** (a) Measured raw signal  $y(t, \vartheta)$  for  $38^\circ\text{C}$  and  $28^\circ\text{C}$ ; (b) Measured differential signals  $\Delta y(t, \Delta \vartheta_{m,n})$  with  $\vartheta_m = 38^\circ\text{C}$  and  $\vartheta_n = 37^\circ\text{C} \dots 28^\circ\text{C}$ ; (c) Maximum amplitude of the measured differential signals depending on  $\Delta \vartheta_{m,n}$  for each channel, where channel one is e.g. Tx  $\rightarrow$  Rx<sub>1</sub> as depicted in Figure 4.20.

For the sake of simplicity, a specular reflection at the boundary between the surrounding medium and the target is assumed, so the reflection coefficient is given by

$$\underline{\Gamma}_\vartheta(f, \vartheta) = \frac{\sqrt{\varepsilon_{oil}(f)} - \sqrt{\varepsilon_{H_2O}(f, \vartheta)}}{\sqrt{\varepsilon_{oil}(f)} + \sqrt{\varepsilon_{H_2O}(f, \vartheta)}}. \quad (4.9)$$

The complex permittivity of sunflower oil can be found in Ley et al. [2018b] and the temperature-dependent complex permittivity of distilled water is given by Ellison [2007]. If one considers Equation (4.8), the first term is temperature-independent, whereby the temperature dependence is described by the second part  $\Delta \underline{\Gamma}_\vartheta(f, \Delta \vartheta_{m,n})$ . Figure 4.22(a) shows the real part of  $\Delta \underline{\Gamma}_\vartheta(f, \Delta \vartheta_{m,n})$  for various temperature differences where it is obvious that the curves show a nearly linear behavior for low temperature differences, but towards higher temperature differences the curve shapes become slightly nonlinear in the upper frequency range. Figure 4.22(b) shows the imaginary part, which increases with higher temperature differences. With knowledge of the temperature-dependent dielectric properties, the measured differential signals can be validated using the following model



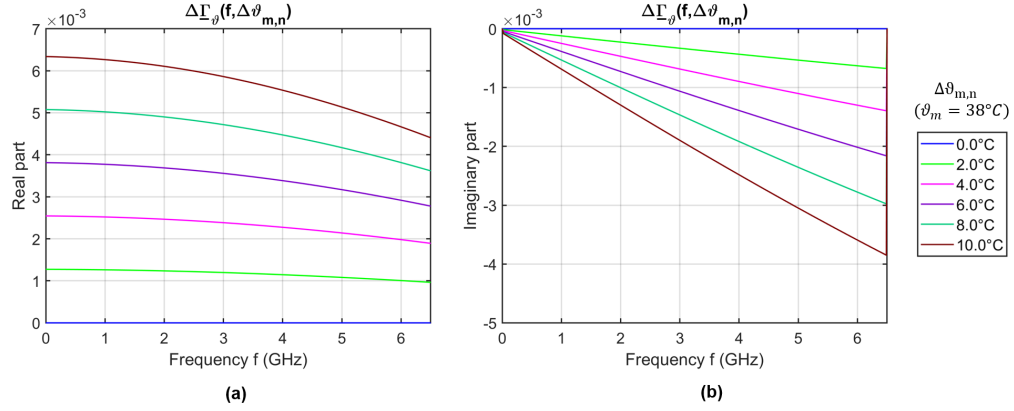


**Figure 4.22:** Temperature dependency of the differential reflection coefficient  $\Delta\Gamma_\vartheta(f, \Delta\vartheta_{m,n})$ .

assumption. Equation (4.8) can be formulated as

$$\underline{Y}_0(f) = \frac{\Delta Y(f, \Delta\vartheta_{m,n})}{\Delta\Gamma_\vartheta(f, \Delta\vartheta_{m,n})} = \frac{\Delta Y(f, \Delta\vartheta_{m,x})}{\Delta\Gamma_\vartheta(f, \Delta\vartheta_{m,x})} \quad (4.10)$$

with the differential signal  $\underline{Y}(f, \Delta\vartheta_{m,x})$  for an arbitrary temperature difference. Finally, the differential signal  $\Delta y(t, \Delta\vartheta_{m,x})$  can be estimated by

$$\underbrace{\Delta Y(f, \Delta\vartheta_{m,x})}_{=\mathcal{F}\{\Delta y(t, \Delta\vartheta_{m,x})\}} = \underbrace{\frac{\Delta Y(f, \Delta\vartheta_{m,n})}{\Delta\Gamma_\vartheta(f, \Delta\vartheta_{m,n})}}_{=\underline{Y}_0(f)=\mathcal{F}\{y_0(t)\}} \cdot \Delta\Gamma_\vartheta(f, \Delta\vartheta_{m,x}) \quad (4.11)$$

where  $\mathcal{F}\{\cdot\}$  denotes the Fourier Transform. Figure 4.23 shows the results of the validation. The measured differential signals are depicted in Figure 4.23(a). Figure 4.23(b) illustrates the estimated differential signals calculated using the temperature-dependent dielectric properties of distilled water (target) and the relative permittivity of oil (surrounding medium) as data input. In addition, one measured differential signal (e.g. preferably the measurement with the maximum temperature difference, in this case  $\Delta y(t, \Delta\vartheta_{38,28})$ ) is necessary to solve Equation (4.11). The estimated differential signals  $\Delta y(t, \Delta\vartheta_{m,x})$  are shown as the result of the calculation step. Figure 4.23(c) compares the maximum amplitudes of the measured and modeled differential signals as a function of temperature for all four channels. The modeled curves also show a linear dependence and agree well with the measured values.

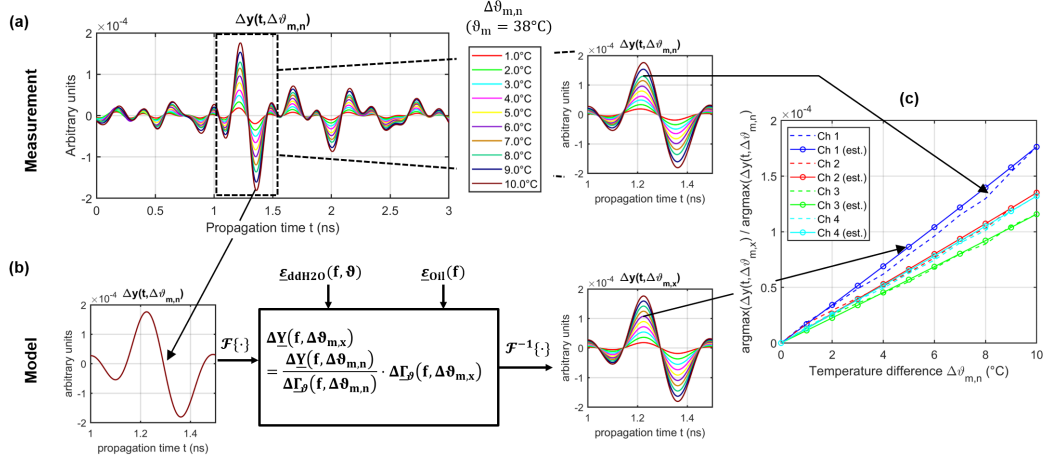


**Figure 4.23:** (a) Measured differential signals  $\Delta y(t, \Delta \vartheta_{m,n})$  with  $\vartheta_m = 38^\circ\text{C}$  and  $\vartheta_n = 37^\circ\text{C} \dots 28^\circ\text{C}$ ; (b) Model approach to validate the measured signals based on one known differential measurement and the dielectric properties of the phantom materials; (c) Maximum amplitudes of the measured differential signals depending on  $\Delta \vartheta_{m,n}$  for each channel and the corresponding maximum of the estimated differential signals.

### 4.3 Discussion

In the first part of this chapter, a reliable measurement method for measuring the temperature-dependent dielectric properties of tissue and blood was presented. The temperature-dependent dielectric properties of *ex vivo* porcine liver, muscle, fat and blood were investigated in the temperature range of  $30^\circ\text{C}$  to  $50^\circ\text{C}$  and in the frequency range between  $0.5\text{ GHz}$  and  $7\text{ GHz}$ . In addition, a temperature-dependent parametric model was introduced to determine the temperature and frequency dependence. The model consists of a two-pole Cole-Cole model to describe the dielectric properties over the frequency range combined with a second order polynomial fit, which models the temperature dependence of the Cole-Cole parameters. The model reduces the data from 3,969 data points to 20 model parameters per tissue and provides access to arbitrary values in the specified temperature and frequency range.

The measurements indicate that the dielectric properties of porcine tissue (liver, muscle and fat) show intra-individual differences between various samples of one animal as well as inter-individual differences between samples of different animals. In contrast, porcine blood shows significant lower intra- as well as inter-individual variations of relative permittivity and effective conductivity.

The dielectric properties of porcine tissue and blood, which were determined by DSP,

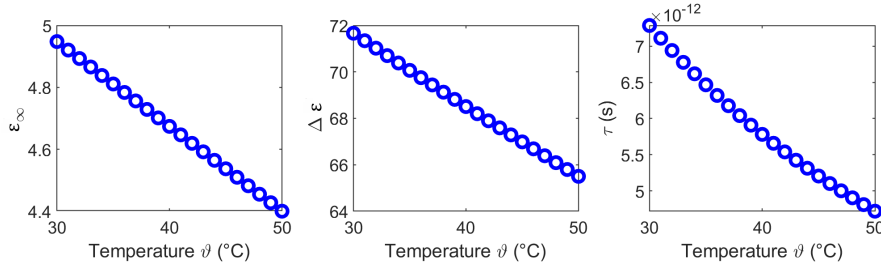


**Figure 4.24:** Temperature-dependent model parameters of pure water corresponding to Kaatze [1989].

correlate to their water content. The water content of blood is between 79 % and 81 %. It has the highest relative permittivity as well as the highest effective conductivity of all investigated samples. In addition, the dielectric properties also show the greatest sensitivity to temperature changes. Liver and muscle contain between 73 % and 78 % water as given by Pethig and Kell [1987]. Due to the high water content their dielectric properties are much higher in comparison with fat, which has a water content between 5 % and 20 % percent (see Pethig and Kell [1987]). Furthermore, the results of liver and muscle have an almost identical temperature sensitivity of their dielectric properties. However, fat shows the lowest temperature-dependent changes of the relative permittivity and effective conductivity.

The correlation between the permittivity of the investigated samples and their water content is consistent with the fact that the dielectric properties in the microwave frequency range are related to the rotation of water molecules. Kaatze [1989] and Ellison [2007] described the temperature-dependent dielectric properties of pure water over a broad frequency range. The temperature-dependent complex permittivity in the microwave frequency range can be modeled with the Debye model as presented by Kaatze [1989]. Figure 4.24 depicts the Debye parameter of pure water as a function of temperature. The parameters  $\varepsilon_\infty, \Delta\varepsilon, \tau$  decrease with increasing temperature similar to the Cole-Cole parameters  $\varepsilon_\infty, \Delta\varepsilon_1, \tau_1$  of the tissues investigated in Section 4.1.4. In contrast, the static conductivity  $\sigma_s$  of the investigated tissues and blood increases towards higher temperatures. This behavior is in accordance with the results of liver presented by Lazebnik et al. [2006]. The parameters  $\Delta\varepsilon_2$  and  $\tau_2$  corresponding to the second Cole-Cole pole mainly influence the lower frequency range. This is evident from the increasing relative permittivity in the frequency range between 0.5 GHz and 2 GHz, which is not represented by the data of the single-pole Cole-Cole model from Lazebnik et al. (see Figure 2.9). The relaxation time  $\tau_2$  of the second Cole-Cole pole decreases with increasing temperature. However, the tissue-specific dispersion amplitudes  $\Delta\varepsilon_2$  are constant over the temperature range and the

values are identical to the initial dispersion amplitudes  $\Delta\epsilon_{2,init}$ , which correspond to the values given by Gabriel et al. [1996c].

Considering the high water content samples liver, muscle and blood, the strongest temperature induced changes in relative permittivity occur in the frequency range between 1 and 4 GHz. This frequency range coincides with the -10 dB fractional bandwidth of the applied active dipole antennas, which is between 1-3 GHz as investigated by Helbig et al. [2012a]. In contrast to the real part, the effective conductivity shows an intersection point at 3 GHz. At this point the imaginary part of the complex permittivity does not generate temperature induced contrast. These findings are essential in terms of choosing the optimal working conditions (e.g. the frequency band) and can be directly incorporated into future developments of UWB temperature monitoring systems.

The results obtained during the first part of this chapter show a significant temperature dependence of the investigated high water content tissues, but the slight differences of the dielectric properties also demonstrate the challenges regarding noninvasive UWB temperature monitoring. In the second part of this chapter, the detectability of temperature changes was investigated by means of UWB M-sequence technology in an experimental phantom measurement setup. The phantom consisted of oil, which is an appropriate fat imitate due to its low dielectric properties and its low temperature dependence as presented by Ley et al. [2018b]. The target was represented by distilled water due to the well known temperature-dependent dielectric properties as given by Kaatze [1989] and Ellison [2007]. In order to ensure a high measurement accuracy and controllable conditions, the measurements were performed at room temperature instead of body temperature. To prove a thermotherapy approach (e.g. hyperthermia), the investigated temperature differences of the target varied between 1 °C and 10 °C. The measurements indicate that temperature changes of 1 °C cause differential signals that are detectable with the active dipole antennas and the UWB MIMO system.

Considering the presented measurement setup, the temperature change is limited to the boundary between the surrounding medium and the target, which can be described by the reflection coefficient as validated by the introduced model approach. The results of both the measured and modeled radar signals show a linear dependence between the changes of the radar signals and the temperature variations in the range between 28 °C and 38 °C. This can be explained by the temperature-dependent differential reflection coefficient of distilled water as shown in Figure 4.22, which shows a nearly linear decrease with increasing temperature in the relevant frequency and temperature range. Such a behavior is also valid for higher temperatures (e.g. between 36 °C and 45 °C) which are common in hyperthermia treatments. The linear dependency can be exploited to derive temperature differences from measured UWB signals in a practical measurement scenario.

However, it should be noted that the increasing nonlinearity of the differential reflection coefficient towards higher temperature differences, as indicated by Figure 4.22, results in a slight distortion of the differential signals for temperature differences higher than 10 °C. Since the temperature-dependent dielectric properties of tissues are mainly influenced by their water content, the linear behavior should also apply to tissue measurements, which needs to be proven in further experiments.

## 5 MNP Detection and Imaging by Means of UWB Microwave Sensing

During the last years, the use of MNPs as contrast agent has gained an increased interest in medical applications as shown in Section 3.2. Contrast enhanced MWI offers a promising approach to increase the diagnostic reliability of breast cancer detection, which is not always given by using MWI methods without contrast agents due to the low dielectric contrast between cancerous tissue and fibro/glandular tissue as described in Section 1.1. The approach is based on the change of the relative permeability  $\underline{\mu}$  of the MNPs by applying an external PMF as described theoretically in Section 2.5. In practice, functionalized MNPs that can specifically bind to tumor tissue are injected intravenously. The so-called active targeting enables the detection of tumors without prior knowledge, since a change in the measured radar signal is caused by the presence of MNPs, which only occurs in combination with tumorous tissue. The magnetic properties of these MNPs are modulated by the external PMF as illustrated in Figure 5.1. The scenario shows the principle for one channel (one Tx and one Rx), where the transmitting antenna emits the low power electromagnetic waves into the MUT. The waves propagate corresponding to the constitutive properties  $(\underline{\varepsilon}, \underline{\mu})$  of the MUT and are partially reflected at each dielectric and magnetic boundary. Switching on the external PMF causes a change in the scattering behavior of the MNPs. If a sufficient amount of MNPs has accumulated in the tumor, these changes can be detected by means of UWB technology. Figure 5.1(c) depicts exemplarily two IRFs recorded by the receiving antenna according to the scenario with and without the presences of an external PMF. It should be noted that in a real measurement scenario the clutter (e.g. antenna crosstalk) and the target response overlap in time. Furthermore, the amplitude of the crosstalk is much higher than the expected tumor response. In order to eliminate the undesired clutter components and to get the MNP response, a differential measurement between the ON and OFF state of the PMF is performed. Due to the non-magnetic properties of the surrounding tissue, changes in the measured signal result from the presence of MNPs as depicted in Figure 5.1.

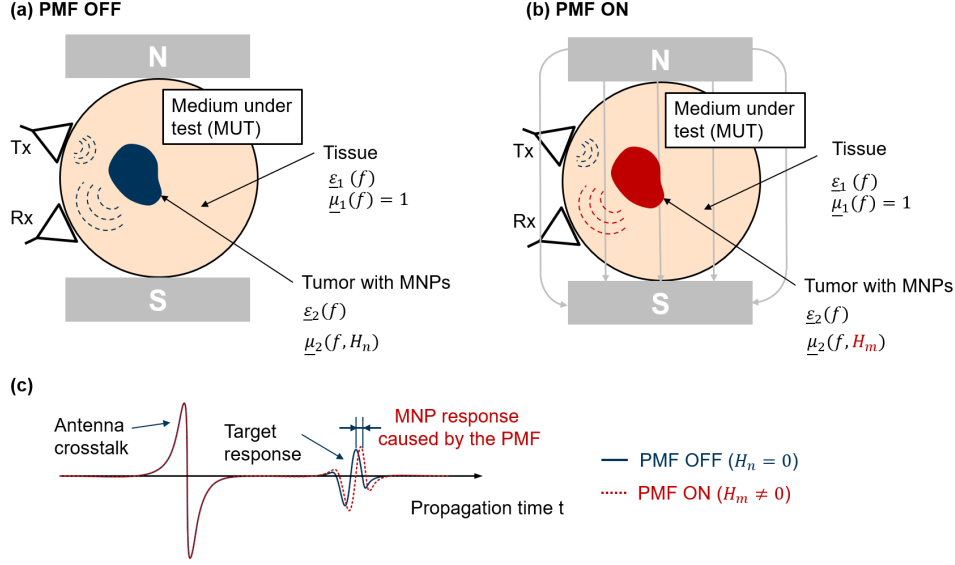


**Figure 5.1:** Principle of contrast enhanced MWI and MNP detection for an ON/OFF modulation of the external PMF; (a) Scenario without the presence of an external PMF; (b) Scenario with the presence of an external PMF; (c) Resulting IRFs for both PMF states.

## 5.1 Influence of the Magnetic Permeability on the UWB Signal

The idea of contrast enhanced MWI is based on an induced magnetic contrast by means of an external magnetic field, as described previously. In this section, the influence of the relative permeability depending on the magnetic field intensity of the external magnetic field (magnetic contrast) on the measured UWB signal (IRF) is analyzed. For this purpose, the recorded IRFs (see Figure 5.1(c)) are described by two components corresponding to Equation (2.21, whereby the contrast  $\zeta$  is replaced by the magnetic field intensity of the external PMF resulting in

$$y(t, H) = y_{cl}(t) + y_{tar}(t, H) \quad (5.1)$$

with the propagation time  $t$ , the magnetic field intensity  $H$ , the static clutter components  $y_{cl}(t)$  (e.g. antenna crosstalk) and  $y_{tar}(t, H)$  representing the target response of the MNP-loaded tumor. Under some idealized conditions (no drift, noise and spurious effects caused by the PMF), the received target response can be modeled as suggested by Sachs et al. [2014]:

$$y_{tar}(t, H) = y_0(t) * \Gamma_H(t, H) \quad (5.2)$$

where  $y_0(t)$  summarizes all magnetic field independent components of the target reflection (including e.g. path-dependent attenuation and propagation time delay corresponding to Equation (2.23)). The magnetic field-dependent reflection coefficient  $\Gamma_H(t, H)$  describes

the signal reflection at the boundary between the surrounding tissue and the MNP-loaded tumor. The static clutter  $y_{cl}(t)$  can be eliminated by a differential measurement:

$$\begin{aligned}\Delta y(t, \Delta H_{m,n}) &= y(t, H_m) - y(t, H_n) \\ &= y_0(t) * [\Gamma_H(t, H_m) - \Gamma_H(t, H_n)].\end{aligned}\quad (5.3)$$

In order to demonstrate the dependence of the measured UWB signals on the magnetic permeability of the MNPs, Equation (5.3) is converted to the frequency domain:

$$\Delta \underline{Y}(f, \Delta H_{m,n}) = \underline{Y}_0(f) \cdot [\underline{\Gamma}_H(f, H_m) - \underline{\Gamma}_H(f, H_n)]. \quad (5.4)$$

For the sake of simplicity, a plane wave propagation as well as a specular reflection at the boundary between the host medium and the target is assumed. Thus, the reflection coefficient can be formulated by

$$\underline{\Gamma}_H(f, H) = \frac{\underline{Z}_2(f, H) - \underline{Z}_1(f)}{\underline{Z}_2(f, H) + \underline{Z}_1(f)}. \quad (5.5)$$

In addition, the impedance of the healthy surrounding tissue can be described by

$$\underline{Z}_1(f) = Z_0 \cdot \sqrt{\frac{\underline{\mu}_1(f)}{\underline{\varepsilon}_1(f)}} \quad (5.6)$$

with  $\underline{\mu}_1(f) = 1$  due to the nonmagnetic properties of tissue and  $Z_0 = \sqrt{\mu_0/\varepsilon_0}$ , where  $\mu_0$  is the permeability constant in free space and  $\varepsilon_0$  is the permittivity constant in free space. The impedance of the tumor with MNPs can be formulated as follows:

$$\underline{Z}_2(f) = Z_0 \cdot \sqrt{\frac{\underline{\mu}_2(f, H)}{\underline{\varepsilon}_2(f)}}. \quad (5.7)$$

Finally, the reflection coefficient is given by the combination of Equations (5.5), (5.6) and (5.7) resulting in

$$\underline{\Gamma}_H(f, H) = \frac{\sqrt{\underline{\mu}_2(f, H) \cdot \frac{\underline{\varepsilon}_1(f)}{\underline{\varepsilon}_2(f)}} - 1}{\sqrt{\underline{\mu}_2(f, H) \cdot \frac{\underline{\varepsilon}_1(f)}{\underline{\varepsilon}_2(f)}} + 1}. \quad (5.8)$$

Considering this equation, it is obvious that the reflection coefficient  $\underline{\Gamma}_H(f, H)$  depends on the dielectric properties  $\underline{\varepsilon}_1$  and  $\underline{\varepsilon}_2$  as well as on the magnetic permeability  $\underline{\mu}_2$  of the investigated MUT. The detection of the MNP response is based on a differential measurement approach in which the contrast is caused by the change of the magnetic properties of the



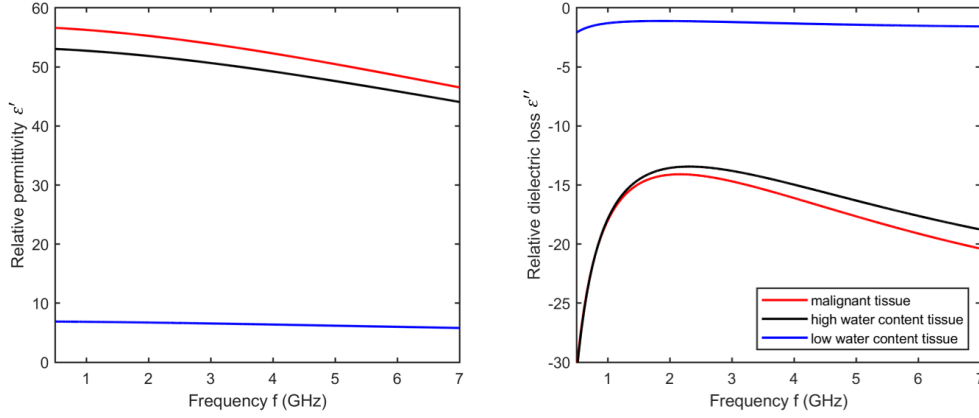


**Figure 5.2:** Relative permittivity and relative dielectric loss of high water content breast tissue as well as malignant breast tissue in the microwave frequency range between 500 MHz and 7 GHz corresponding to Cole-Cole parameters presented by Lazebnik et al. [2007b].

MNPs as described in Equation (5.4). Therefore, the differential reflection coefficient

$$\Delta \underline{\Gamma}_H(f, \Delta H_{m,n}) = \underline{\Gamma}_H(f, \Delta H_m) - \underline{\Gamma}_H(f, \Delta H_n) \quad (5.9)$$

is considered in the following (instead of  $\underline{\Gamma}_H$ ) with  $H_n = 0$  due to the ON/OFF modulation. In order to analyze the influence of the constitutive parameters  $\underline{\epsilon}_1, \underline{\epsilon}_2, \underline{\mu}_2$  on the differential reflection coefficient  $\Delta \underline{\Gamma}_H(f, \Delta H_{m,n=0})$ , two scenarios, one with an MNP-loaded tumor embedded in a high water content tissue (scenario "A") and the other with an MNP-loaded tumor embedded in a low water content tissue (scenario "B"), are analyzed in the microwave frequency range for various differential magnetic field intensities  $\Delta H_{m,0}$  of the external PMF. Figure 5.2 shows the dielectric properties of the healthy and malignant tissue corresponding to the study of Lazebnik et al. [2007b]. The high water content tissue samples (breast tissue with 0-30 % adipose tissue) and the low water content tissue samples (breast tissue with 85-100 % adipose tissue) were obtained from cancer surgeries. The cancer samples were also obtained from cancer surgeries, whereby the samples contained 30 % or higher malignant tissue content. Based on these dielectric properties and the magnetic properties of the MNPs presented in Figure 2.12, the differential reflection coefficient were determined by Equations (5.8) and (5.9). Figure 5.3(a) shows the results for the scenario "A" with an MNP-loaded tumor embedded in a high water content breast tissue, where it is obvious that the differential reflection coefficient  $\Delta \underline{\Gamma}_H(f, \Delta H_{m,n})$  shows a nonlinear behavior in the considered microwave frequency range. Furthermore,  $\Delta \underline{\Gamma}_H(f, \Delta H_{m,n})$  shifts to higher frequencies with an increasing external PMF. Figure 5.3(b) presents the

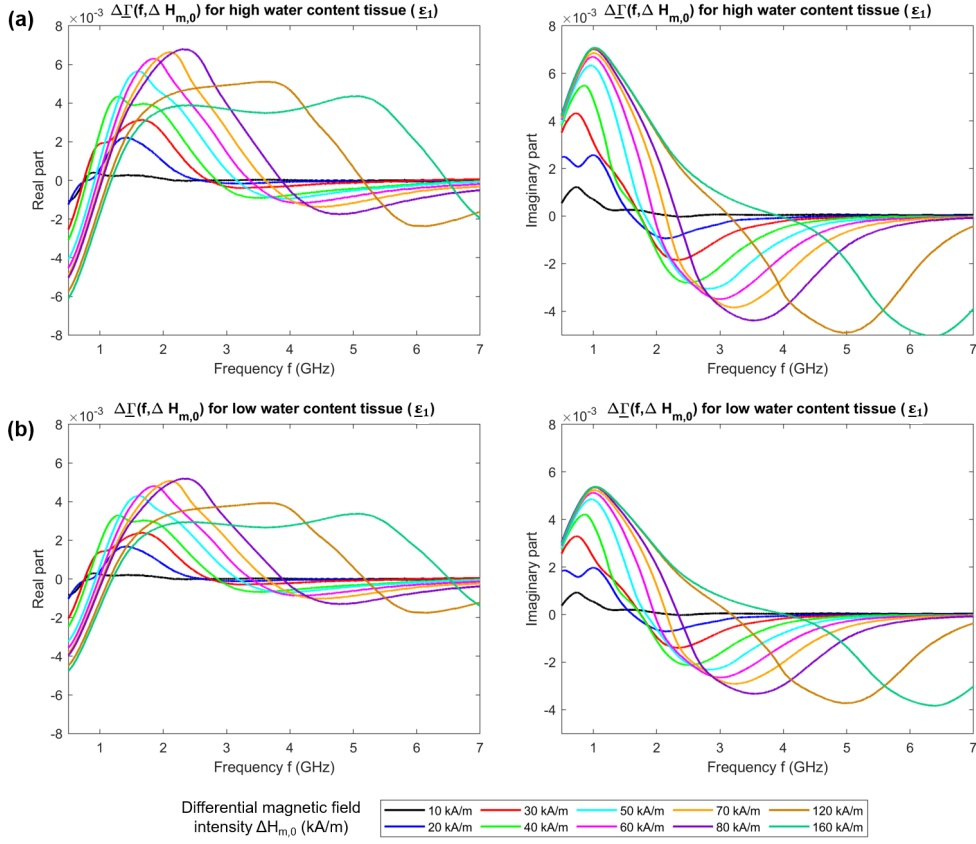


**Figure 5.3:** Differential reflection coefficient  $\Delta\Gamma_H(f, \Delta H_{m,0})$  as a function of frequency for various differential magnetic field intensities  $\Delta H_{m,0}$ ; (a) Scenario "A" for an MNP-loaded tumor embedded in a high water content breast tissue (0-30 % adipose tissue); (b) Scenario "B" for an MNP-loaded tumor embedded in a low water content breast tissue (85-100 % adipose tissue).

results for the scenario "B" with an MNP-loaded tumor embedded in a low water content breast tissue. The shape of the curves shows a similar nonlinear behavior compared with the high water content surrounding medium of scenario "A". However, the amplitude of the differential reflection coefficient is lower, indicating a lower contrast caused by the differential measurement between adipose tissue and MNP-loaded tumor in comparison with scenario "A" (high water content tissue and MNP-loaded tumor). This means, the dielectric properties of the tumor tissue and the surrounding tissue affect the amplitude of the differential reflection coefficient as illustrated in Figure 5.3 for both scenarios ("A", "B"), and thus also influences the MNP response. Moreover, it can be concluded that the MNP response in the measured UWB signal depends on the working frequency range of the MWI system due to the nonlinear differential reflection coefficient.

## 5.2 Clutter Removal and Signal Processing

As already mentioned, the response caused by the magnetic contrast is very low in amplitude compared to the clutter (e.g. antenna crosstalk) and also overlaps in time. Therefore, the undesired signal components must be eliminated before the MNP response induced by the external PMF can be analyzed. Figure 5.4 (left column) shows the signal processing procedure exemplarily for the ON/OFF modulation of the external PMF. Besides the two-state modulation, a low periodic modulation of the external PMF offers a further approach to extract the desired MNP response. Figure 5.4 (right column) illustrates the signal processing steps for a periodic sinusoidal modulation (SIN) of the PMF. A detailed comparison of the two types of modulation is presented in Section 5.4.5. The following equations are valid for both types of PMF modulation, whereby  $MOD$  indicates the applied modulation approach. Figure 5.4(a) shows the magnetic field intensity  $H(T)$  at the position of the MNPs in the air gap of an electromagnet depending on the observation time  $T$ . Between the time interval of two states (ON and OFF), the magnetic field is switched ON or OFF via a ramp function to preserve the electromagnet. Furthermore, this time period ensures that the magnetic field settles. Figure 5.4(b) illustrates the measured raw radargram  $y_{MOD}(t, T, H)$ , whereby each column corresponds to one measured IRF.

The first step is to estimate the clutter (e.g. antenna crosstalk) that superimposes the desired MNP response. It is determined by averaging the IRFs over the time period without the presence of a PMF ( $H_n = 0 \text{ kA/m}$ ) corresponding to

$$\bar{y}(t, H_n) = \frac{1}{T_{OFF}} \int_{T_{OFF}} y_{MOD}(t, T, H) dT, \quad H_n = 0 \text{ kA/m} \quad (5.10)$$

where  $t$  is the propagation time,  $T$  the observation time (measurement time) and  $T_{OFF}$  the time interval in which the electromagnet is switched off (see Figure 5.4(b)).

In the second step, the clutter removed radargram  $\Delta y_{MOD}(t, T, \Delta H_{m,0})$  (see Figure 5.4(c)) is calculated by subtracting the mean IRF  $\bar{y}(t, H_n=0)$  column by column from the raw radargram:

$$\Delta y_{MOD}(t, T, \Delta H_{m,0}) = y_{MOD}(t, T, H_m) - \bar{y}(t, H_n=0) \quad (5.11)$$

and the mean MNP differential signal is computed by

$$\Delta \bar{y}_{MOD}(t, \Delta H_{m,0}) = \frac{1}{T_{ON}} \int_{T_{ON}} \Delta y_{MOD}(t, T, \Delta H_{m,0}) dT. \quad (5.12)$$

In a further step, the differential signals can be analyzed in the frequency domain. Since the modulation sequence of the PMF is known, the MNP response can be extracted at

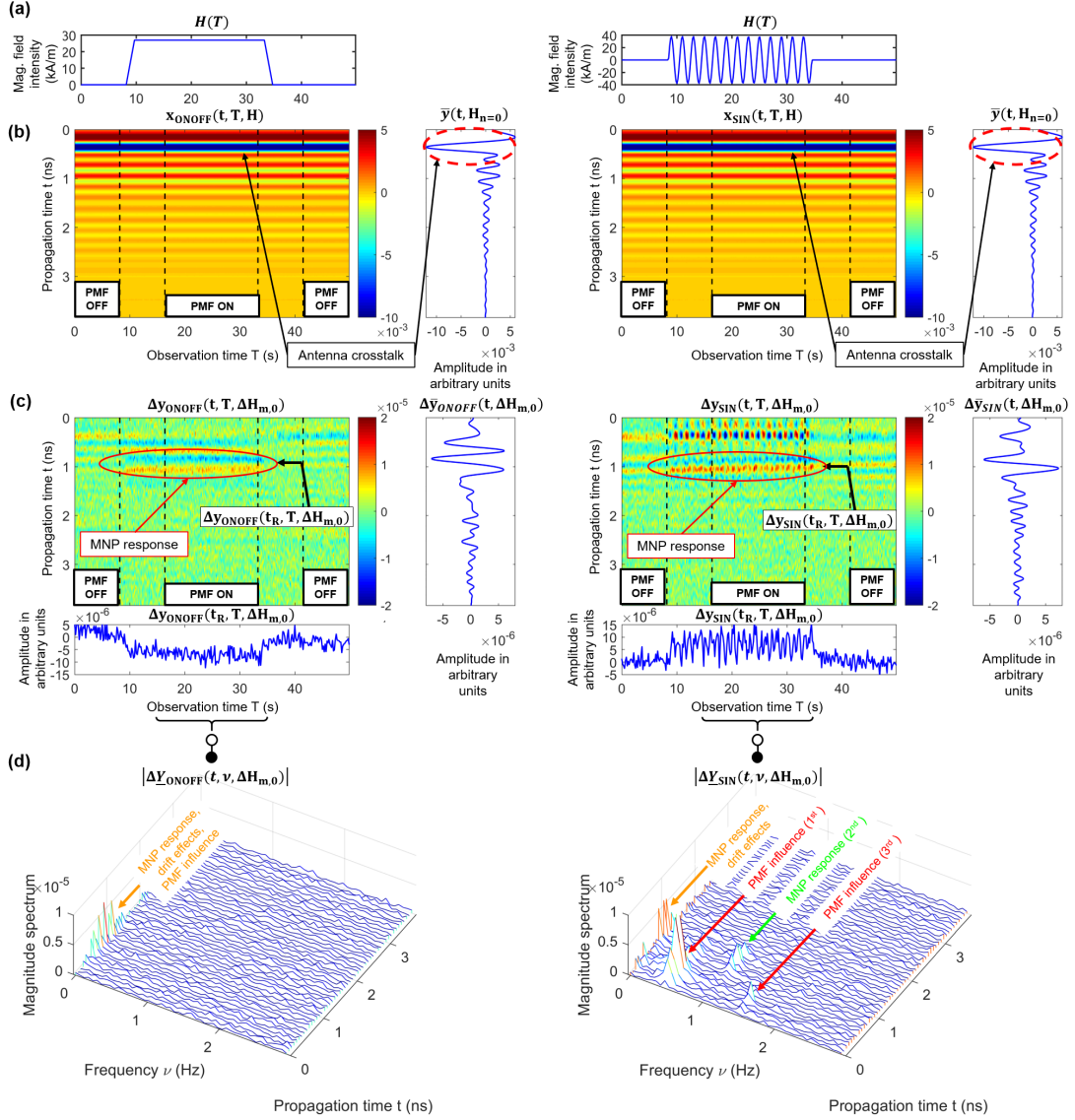


**Figure 5.4:** Clutter removal and signal processing exemplary for the ON/OFF modulation (left column) and the SIN modulation (right column); **(a)** Magnetic field intensity depending on the observation time  $T$  at the position of the MNPs; **(b)** Raw radargram  $y_{MOD}(t, T, H)$  and the estimated clutter signal  $\bar{y}(t, H_{n=0})$  averaged over the time period without the presence of the external PMF; **(c)** Clutter removed radargram  $\Delta y_{MOD}(t, T, \Delta H_{m,0})$  with the mean MNP response  $\Delta \bar{y}_{MOD}(t, \Delta H_{m,0})$  averaged over the time period with the presence of the external PMF. The index  $t_R$  represents the propagation time corresponding to the expected MNP response; **(d)** Single sided magnitude spectrum  $|\Delta Y_{MOD}(t, \nu, \Delta H_{m,0})|$ .

the related frequency. The frequency spectrum is calculated using the Fourier Transform in observation time:

$$\Delta Y_{MOD}(t, \nu, \Delta H_{m,0}) = \frac{1}{T_{ON}} \int_{T_{ON}} \Delta y_{MOD}(t, T, \Delta H_{m,0}) \cdot e^{-j2\pi\nu T} dT. \quad (5.13)$$

In case of the ON/OFF modulation, the MNP response occurs at the DC component ( $\nu = 0 \text{ Hz}$ ) as shown in the left plot of Figure 5.4(d).

The MNP response of the SIN modulation occurs at  $\nu = 0 \text{ Hz}$  and the second harmonic  $\nu = 1 \text{ Hz}$  of the modulation frequency as illustrated on the right side of Figure 5.4(d). Since the MNP response in the measured UWB signal is independent of the sign of the magnetic field intensity  $H(T)$  of the external magnetic field, there is no sign change of the MNP response over the observation time  $T$  as shown in Figure 5.4(c) (right column). Therefore, the MNP response has a periodic shape corresponding to the absolute value of the SIN modulation, resulting in a DC component (at  $\nu = 0 \text{ Hz}$ ) and further components at the even harmonics (e.g.  $\nu = 1 \text{ Hz}$ ) in the frequency spectrum (see Figure 5.4(d) (right column)). Further signal components occur at the modulation frequency  $\nu_{SIN} = 0.5 \text{ Hz}$  (1st harmonic) and at  $\nu_{SIN} = 1.5 \text{ Hz}$  (3rd harmonic). These spurious effects arise from the interaction of the PMF with the measurement setup as described by Bucci et al. [2018]. Further disturbing components are very slowly time-varying drift effects that occur in the low frequency range and superimpose the MNP response in this range. Nevertheless, the periodic modulation approach offers the possibility to separate the MNP response (at the 2nd harmonics) from the disturbing influences, which is not the case with ON/OFF modulation, since the MNP response at  $\nu = 0 \text{ Hz}$  is superimposed by the slight drift effects as well as by the spurious effects caused by the interaction of the PMF with the measurement setup.

### 5.3 Influences on the Detectability of MNPs

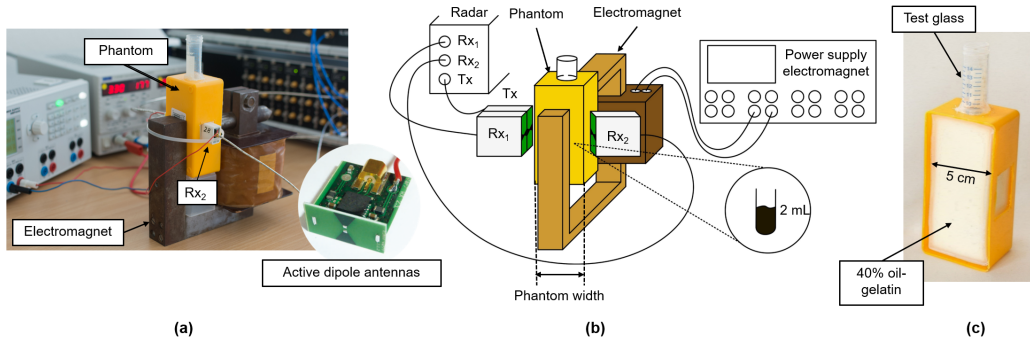
This section deals with the detection of MNPs depending on the magnetite mass as well as the magnetic field intensity of the external PMF. In addition, the viscosity of the surrounding medium in which the MNPs are embedded is analyzed, since it cannot be readily assumed that the MNPs exhibit the same behavior in water as in a more or less immobilizing environment such as tissue. Therefore, the influence of the viscosity of an MNP-loaded target on the measured UWB signal is investigated. The experiments were performed using an electromagnet with an air gap of approximately 4 cm and different kinds of phantoms.

### 5.3.1 Mass Dependency of the MNPs

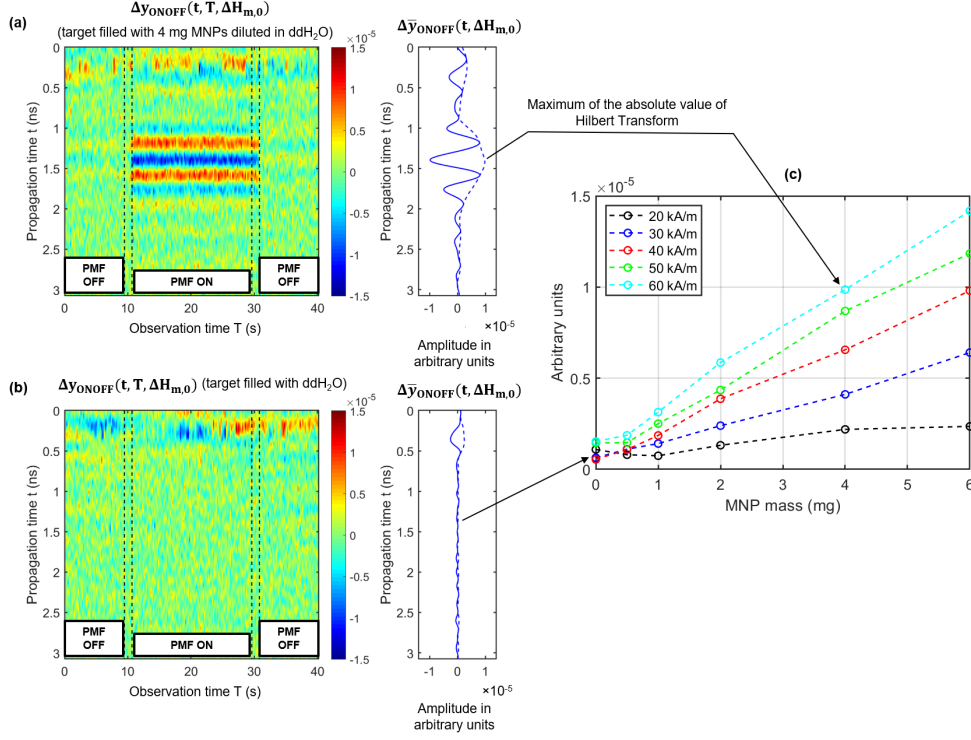
Figure 5.5 shows the measurement setup to determine the detection constraints of MNPs depending on the MNP mass according to Ley et al. [2015]. The noncoated MNPs (WHKS 1S12, Liquids Research Limited, Bangor, UK) had a saturation magnetization of  $M_s = 400$  G and a particle diameter of 10 nm. The viscosity of the raw ferrofluid is  $\eta < 50$  cP. They were diluted in distilled water and filled in a test glass, which was placed inside of a tissue mimicking phantom. The total volume of the ferrofluid solution was constantly 2 mL and the MNP concentration varied corresponding to the investigated MNP mass. The tissue substitute consisted of 40 % oil-gelatin (OG) according to the mixture presented by Lazebnik et al. [2005]. The phantom had a width of 5 cm and was placed inside the air gap of the electromagnet. The magnetic field intensities in the MNP region were determined by measuring the absolute magnetic flux density using a Gauss Meter (Model 7030 Gauss/Tesla Meter, F.W. Bell, Milwaukee, USA). The MNP responses were determined for different magnetite masses and magnetic field intensities.

Figure 5.6(a,b) shows the clutter removed radargrams  $\Delta y_{ONOFF}(t, T, \Delta H_{m,0})$  corresponding to Equation (5.11) for the scenario with 4 mg MNPs diluted in distilled water (mixture concentration of 2 mg/mL) and a magnetic field intensity of 60 kA/m as well as for the reference measurement with 2 mL distilled water inside test glass (no MNPs) and a magnetic field intensity of 40 kA/m. Figure 5.6(c) presents the maximum of the envelope of the mean MNP response  $\bar{y}_{ONOFF}(t, \Delta H_{m,0})$  as a function of MNP mass for different magnetic field intensities. It is obvious that the curves show a nearly linear dependency between the MNP response and the MNP mass.

This linear relationship is evaluated in a second measurement, whereby the movement



**Figure 5.5:** Experimental measurement setup for MNP detection depending on the MNP mass; (a) Laboratory measurement setup: The phantom is placed inside the air gap of the electromagnet. Small active dipole antennas are connected to the UWB M-sequence radar system; (b) Corresponding measurement schematic; (c) Phantom box filled with 40 % OG and a test glass with the MNPs inside.



**Figure 5.6:** (a) Clutter removed radargram and the mean response for the target filled with 4 mg MNPs diluted in distilled water; (b) Clutter removed radargram and the mean response for the reference target filled with distilled water (no MNPs); (c) Maximum of the envelope of the MNP responses as a function of the MNP mass for different magnetic field intensities.

of the MNPs was suppressed. In the first experimental setup (see Figure 5.6) the MNPs were filled in an open test glass, which allows them to move slightly towards the magnetic pole for high magnetic field intensities as illustrated in Figure 5.7(a). This results in a change of the scattering area, which enhances the differential signal between the ON and OFF state of the PMF. The aim of the second experiment was to determine only the influence of the changing permeability of the MNPs induced by the external PMF, independently of a possible change in the scattering area caused by the movement of the MNPs. Figure 5.7(b) shows the measurement setup with a modified phantom. A 3D printed box acted as antenna array as well as phantom holder. It was placed inside the air gap of the electromagnet. The phantom consisted of 96 wt./wt. % distilled water and 4 wt./wt. % agar and had a dimension of  $60 \times 38 \times 100 \text{ mm}^3$ . The MNPs diluted in distilled water were filled into a 3D printed hollow sphere embedded in the agar phantoms so that particle movement was suppressed. In total, six phantoms with targets of a volume of 2 mL and different MNP masses were prepared. In contrast to the first experiment, the targets were placed close to the magnetic pole, where the magnetic field intensity was



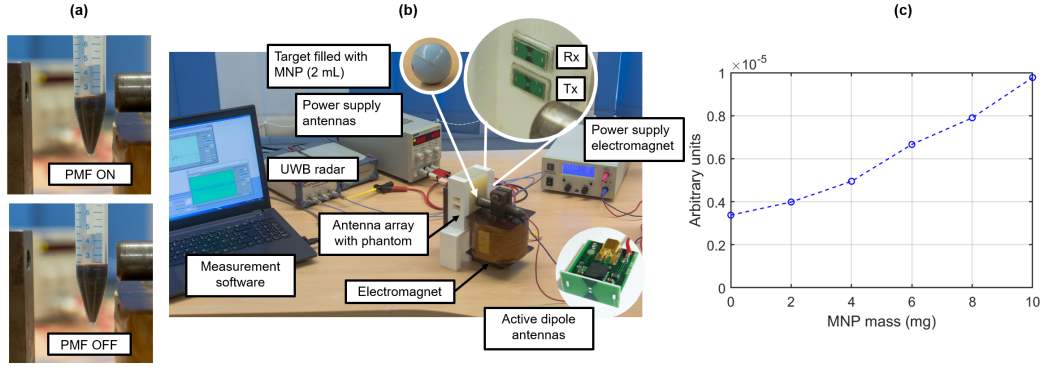


**Figure 5.7:** (a) Superparamagnetic liquid: MNPs diluted in distilled water with (PMF ON) and without (PMF OFF) the presence of an external PMF; (b) Experimental measurement setup for MNP detection depending on the MNP mass with a spherical target; (c) Maximum of the envelope of the MNP responses as a function of the MNP mass.

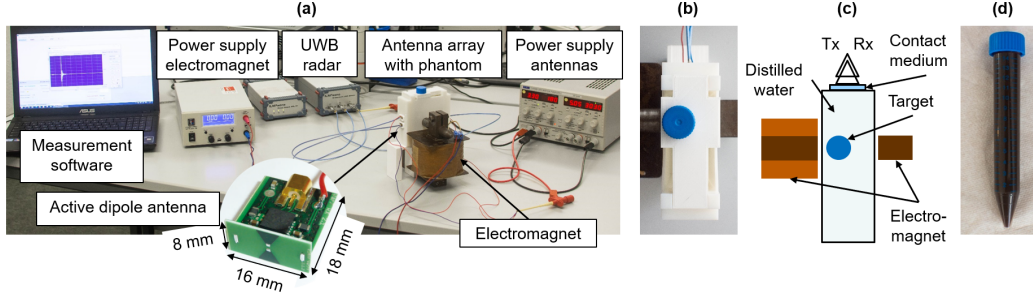
approximately 150 kA/m.

Figure 5.7(c) shows the results, where the linear dependence between the MNP response and the MNP mass is confirmed. The signal processing is identical as presented previously. The clutter removed radargram is computed corresponding to Equation (5.11) for each phantom and MNP mass, respectively. Afterwards, the maximum of the envelope of the mean MNP response is computed.

### 5.3.2 Influence of the Viscosity of the Target and the Magnetic Field Intensity of an External PMF on the MNP Response

The experiments presented in the previous section were based on MNPs diluted in distilled water. Considering a practical scenario, the MNPs are immobilized in the tumor tissue as demonstrated by Dutz et al. [2011]. Therefore, the influence of the viscosity of the surrounding medium in which the MNPs are embedded is investigated in a further experimental measurement setup. In addition, the influence of the magnetic field intensity in the range between 0 kA/m and approximately 140 kA/m on the MNP response is analyzed as shown by Ley et al. [2020b, 2021]. Figure 5.8 shows the corresponding measurement setup. It consisted of a 3D printed box filled with distilled water. This box also acted as antenna array for the active dipole antennas. It was placed inside the air gap of the electromagnet and had a dimension of  $60 \times 38 \times 100 \text{ mm}^3$ . The targets were test glasses filled with MNPs diluted in distilled water or embedded in agar, gelatin or two types of oil-gelatin. A total of 15 targets (three of each medium) with a volume of 15 mL including 100 mg of MNPs were prepared. The agar targets were composed of 97 wt./wt. % distilled water mixed with the MNPs and 3 wt./wt. % agar. The gelatin targets consisted of 90 wt./wt. % distilled water





**Figure 5.8:** Experimental measurement setup for MNP detection depending on the viscosity and the magnetic field intensity of the PMF; **(a)** A 3D printed tank filled with distilled water is placed inside the air gap of the electromagnet. This tank acts as antenna array. The active dipole antennas are connected to an UWB M-sequence radar; **(b)** Top view of the phantom with a bracket holding the test glass in the right position; **(c)** Corresponding schematic of the phantom box inside the air gap; **(d)** Test tube filled with MNPs embedded in gelatin.

mixed with the MNPs and 10 wt./wt. % gelatin. Furthermore, the 0 % OG and 40 % OG targets were prepared corresponding to the procedure presented by Lazebnik et al. [2005] without the addition of formaldehyde. Besides, three test glasses filled with distilled water were analyzed as reference. The targets were positioned close to the magnetic pole by using a holder as shown in Figure 5.8(b).

In a first step, the influence of the magnetic field intensity in the range between 0 and 140 kA/m on the MNP response was analyzed for six targets (one target with distilled water, MNPs diluted in distilled water, MNPs embedded in agar, gelatin and two types of oil-gelatin). Figure 5.9 shows the clutter removed radargrams  $\Delta y_{ON/OFF}(t, T, \Delta H_{m,0})$  according to Equation (5.11) for an ON/OFF modulation with a test glass filled with MNPs diluted in distilled water (a) and a reference target filled with distilled water and no MNPs (b). Figure 5.9(c) depicts the maximum of the envelope of the MNP response as function of the magnetic field intensity of each target. The black curve indicates the results of the test glass filled with distilled water without MNPs. As can be seen, the reference measurement shows no dependence on the magnetic field intensity. In contrast, the curves of the MNP-loaded targets clearly depend on the magnetic field intensity of the PMF. The MNP responses have a similar curve progression, where the maximum of the envelope increases with a rising magnetic field and reaches a maximum between 60 kA/m and 80 kA/m. The values decrease slightly for magnetic field intensities higher than 80 kA/m. Furthermore, the amplitudes of the MNP responses vary depending on the viscosity and the surrounding medium in which the MNPs are embedded, respectively.

In order to examine these differences, a second experiment was performed by analyzing the MNP response at a magnetic field intensity of 80 kA/m in more detail. The

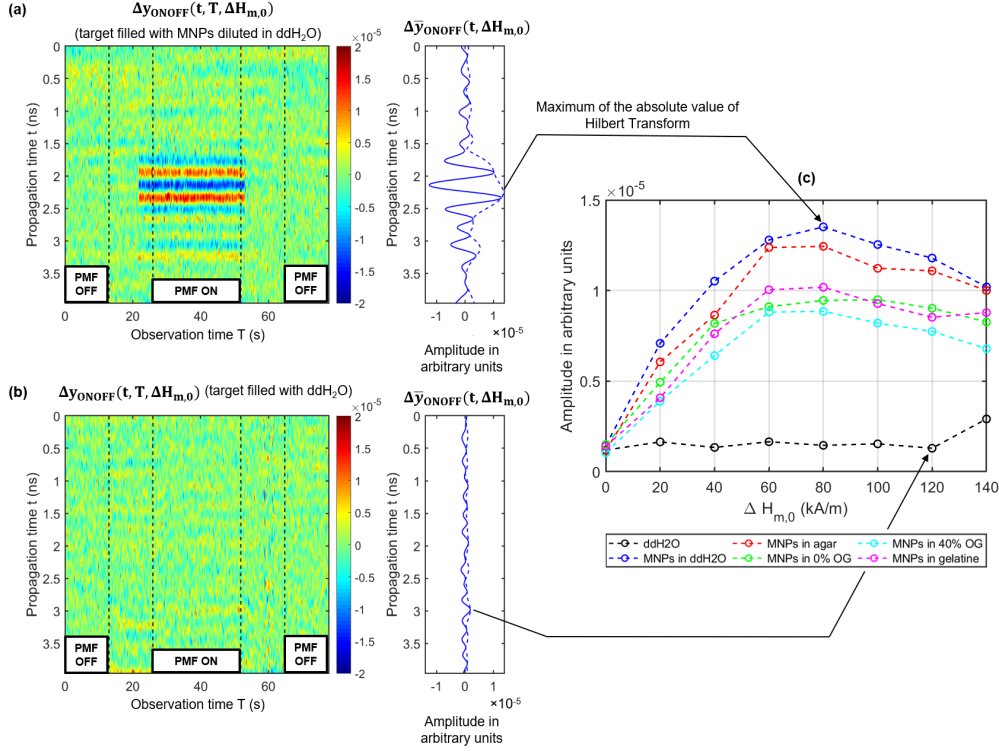


**Figure 5.9:** (a) Clutter removed radargram and the mean response for the target filled with MNPs diluted in distilled water; (b) Clutter removed radargram and the mean response for the reference target filled with distilled water; (c) Maximum of the envelope of the MNP responses as a function of the magnetic field intensity for different targets, whereby 0 % OG and 40 % OG indicate the mixture ratio oil in gelatin according to Lazebnik et al. [2005]. Black curve corresponds to the reference measurement where the target is filled with distilled water without MNPs.

MNP response for all 18 targets was measured eleven times resulting in a total number of 198 measurements. Figure 5.10(a) shows the maximum amplitudes of the envelope of the MNP responses. Each boxplot represents the results of eleven measurements of one target. The values are in accordance with the amplitudes shown in Figure 5.9(c) at  $\Delta H_{m,n} = 80$  kA/m and confirm a difference of the MNP responses depending on the viscosity and surrounding medium, respectively. In addition, the amplitudes of the distribution of each target are compared with all other targets by means of the two-sample Kolmogorov-Smirnov test according to Massey Jr. [1951]. The test returns a decision for the null hypothesis that the two data sets of the different targets have the same continuous distribution. The alternative hypothesis is that the data of two different targets have different continuous distributions. Figure 5.10(b) summarizes the test decisions, whereby the test confirms the null hypothesis at the 5 % significance level  $H_0=H_1$  (both data sets have the same distribution). Otherwise, the test rejects the null hypothesis  $H_0 \neq H_1$  and

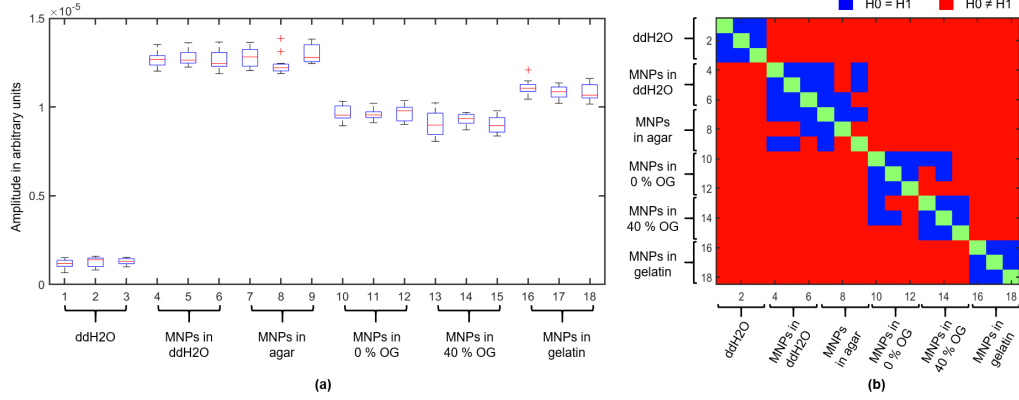


**Figure 5.10:** Results of the MNP response depending on the embedded medium, where 0 % OG and 40 % OG indicate the mixture ratio oil in gelatin corresponding to Lazebnik et al. [2005]; (a) Boxplots for each target showing the median (central mark of each box) and  $\pm 2.7$  standard deviations (whiskers); (b) Results of the two-sample Kolmogorov-Smirnov test.

confirms the alternative hypothesis. The test decisions indicate a significant difference between the reference measurement (test glass filled with distilled water and no MNPs) and all other targets with MNPs, which means that the MNPs can be detected reliably in all mixtures. Moreover, it can be distinguished significantly between three 'test groups' of targets. Group one includes the test glasses with MNPs diluted in distilled water and embedded in agar, group two represents the test glasses filled with the MNPs embedded in oil-gelatin corresponding to Lazebnik et al. [2005] and group three consists of the targets with MNPs embedded in 10 % gelatin. However, the results indicate no significant differences between the MNPs diluted in distilled water and embedded in agar. Furthermore, it is not possible to distinguish unambiguously between MNPs embedded in 0 % or 40 % oil-gelatin.

## 5.4 MNP Imaging

This section deals with the imaging of MNPs by means of UWB pseudo-noise sensing in a real measurement setup and presents the current UWB microwave MNP imaging setup. Furthermore, the imaging results of a target depending on the position and the penetration depth are analyzed. In addition, the influence of the inhomogeneity of the magnetic field distribution is investigated and a calibration approach is presented. Finally, this section compares two different types of PMF modulation in terms of the detectability of MNPs with respect to spurious effects as well as their practical application.

### 5.4.1 Measurement Setup

#### MNP Differential Microwave Imaging Setup

The current UWB measurement setup for MNP imaging has been developed in recent years as shown by Ley et al. [2016, 2017, 2021]. Figure 5.11 shows the setup consisting of an electromagnet with an air gap of approximately 14 cm. It was operated with a voltage source (EAC-S 3000, ET System electronic GmbH, Altlußheim, Germany). The antenna array with the active dipole antennas (see Figure 5.11(c,d)) and the cone-shaped examination mold (see Figure 5.11(e)) were placed inside the air gap of the electromagnet. In addition, a silicone layer mixed with 20 wt./wt. % carbon was placed between the antennas and the examination mold to achieve a better impedance matching. The setup included 8 transmitting and 16 receiving antennas, resulting in a total number of 128 channels. The antennas were connected with an UWB MIMO radar system (9th order M-sequence and a 13 GHz clock rate) via nonmagnetic high-frequency cables. The examination mold was filled with cream (32 % fat content) as a healthy tissue substitute (see Figure 5.11(b)). The tumor mimicking target consisted of 10 % gelatin mixed with distilled water and an MNP concentration of 25 mg/mL. The comparatively high concentration was chosen with

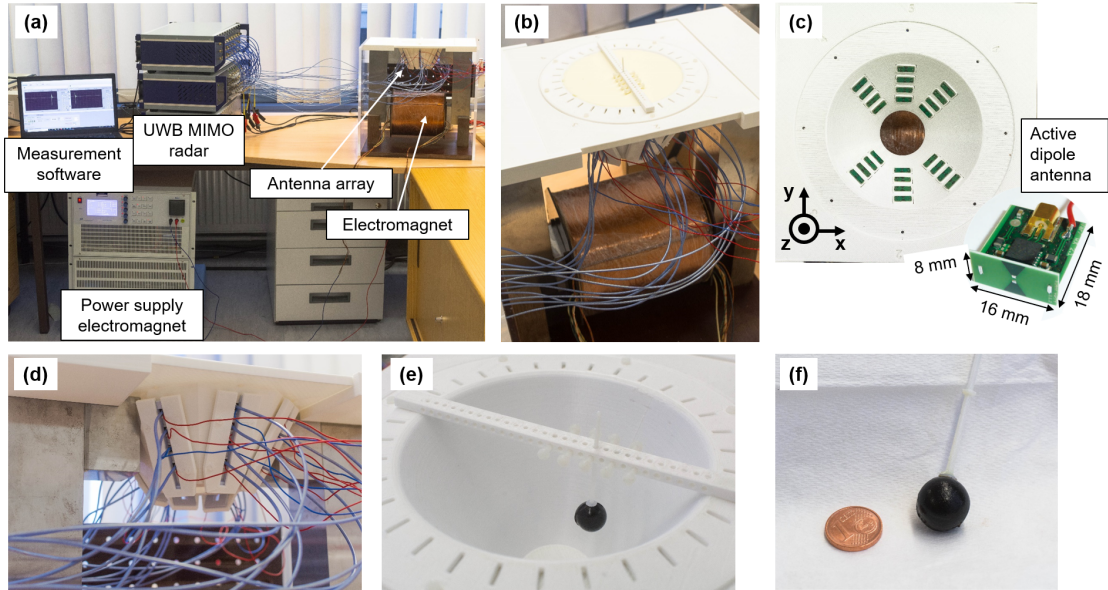


**Figure 5.11:** (a) UWB microwave MNP imaging setup; (b) Examination mold filled with the tissue mimicking material (cream) and the target inside; (c) Top view of the antenna array showing the arrangement of the active dipole antennas; (d) Antenna array placed in the air gap of the electromagnet with the antenna attachment; (e) Examination mold with the tumor mimicking target, which is positioned with the help of a holder; (f) Target with a volume of 2 mL and an MNP concentration of 25 mg/mL.

regard to the detectability of MNPs even at large penetration depths. The volume of the target was 2 mL as depicted in Figure 5.11(f). It was positioned in the mold by means of a holder as illustrated in Figure 5.11(e).

### Magnetic Field Measurement Setup

The electromagnet of the microwave imaging setup presented in the previous section does not have a homogeneous magnetic field distribution in the air gap. Due to the fact that an inhomogeneous magnetic field influences the MNP imaging results depending on the target position, it is essential to analyze the magnetic field distribution within the air gap. Therefore, the magnetic field intensity was measured for a total volume of  $[x \times y \times z] = [11 \times 11 \times 10] \text{ cm}^3$  with a spatial resolution of 5 mm. The magnetic flux density was measured with a transversal probe (BTP 201-75F, Dr. Brockhaus Messtechnik GmbH & Co. KG, Lüdenscheld, Germany) connected to a Gaussmeter (BGM 201, Dr. Brockhaus Messtechnik GmbH & Co. KG, Lüdenscheld, Germany). The probe was

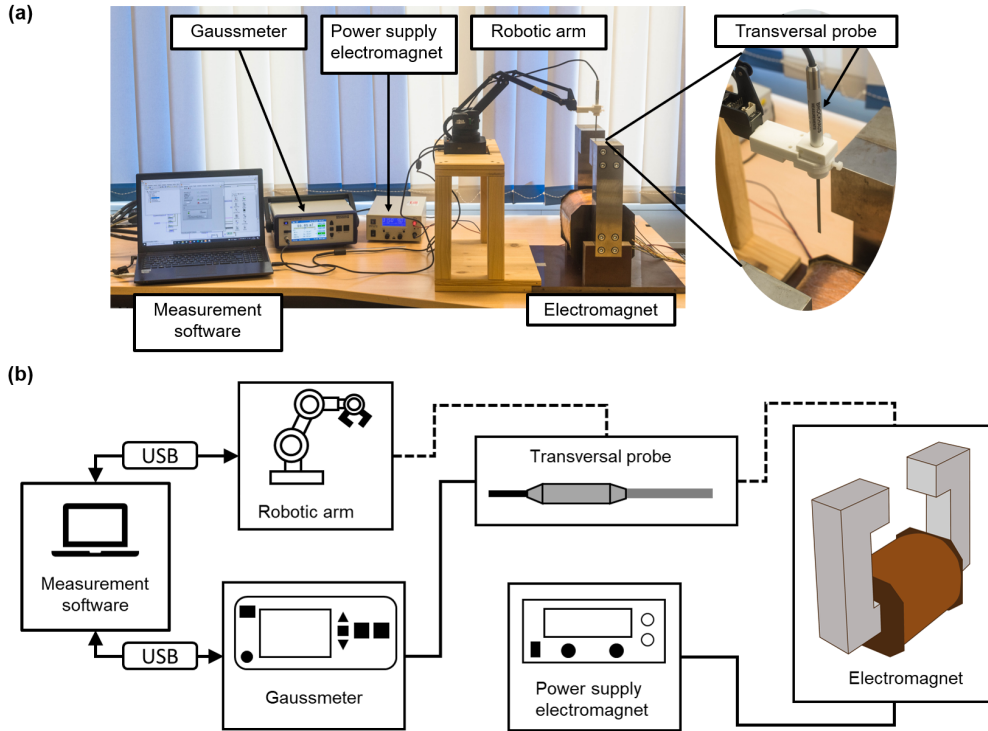


**Figure 5.12:** Magnetic field measurement setup; (a) Magnetic flux density is measured by a transversal probe connected to a Gaussmeter. The probe is clamped into a robotic arm. Both, Gaussmeter and robotic arm are controlled by LabVIEW; (b) Corresponding schematic of the setup.

clamped into a robotic arm (uArm Swift Pro, UFACTORY, Guangdong, China) using 3D printed adapters. Both systems were connected to a PC via USB and controlled by LabVIEW. Figure 5.12 shows the measurement setup corresponding to the project work of Kalla et al. [2020]. The stepper motors of the robotic arm were used to move and position the probe in the magnetic field. After each step, the magnetic flux density was recorded resulting in a total number of 11.109 measurement points corresponding to the investigated volume with a spatial resolution of 5 mm. Since the probe measures only one magnetic field component, the volume had to be measured for each of the three magnetic field components ( $B_x$ ,  $B_y$ ,  $B_z$ ). In order to reduce the measurement effort, the symmetry of the electromagnet could be exploited. Some preliminary investigations (see Kalla et al. [2020]) showed that measuring a quarter of the total volume for the B-field components  $B_x$  and  $B_z$  and one-eighth of the total volume for the B-field component  $B_y$  were sufficient and that the remaining values could be calculated due to the symmetry of the setup. Subsequently, the absolute value of the magnetic flux density for each position was calculated by

$$|B(\mathbf{r}_0)| = \sqrt{B_x^2(\mathbf{r}_0) + B_y^2(\mathbf{r}_0) + B_z^2(\mathbf{r}_0)} \quad (5.14)$$

and converted to the magnetic field intensity

$$|H(\mathbf{r}_0)| = \frac{|B(\mathbf{r}_0)|}{\mu_0}. \quad (5.15)$$

Finally, the results of the spatial distribution of the magnetic field intensity can be used to correct the magnetic field dependent MNP response at different target positions.

#### 5.4.2 MNP Imaging via DAS-Beamforming

The image processing is based on the DAS-beamforming algorithm introduced in Section 2.3. In contrast to Equation (2.24), the absolute value of the differential signal is used as input signal:

$$I(\mathbf{r}_0) = \sum_{ch=1}^N |\Delta y_{ch}(\tau_{ch}(\mathbf{r}_0), \Delta H_{m,n}(\mathbf{r}_0))| \quad (5.16)$$

where the clutter removed differential signal of channel  $ch$  is represented by  $\Delta y_{ch}$ . Calculating the UWB image by means of the absolute value of the differential signal, on the one hand, the signal components are prevented from being canceled out by the coherent summation, but on the other hand, the influence of the noise increases. A total of 48 channels are used for imaging processing. The other ones are not included due to the fact that channel configurations with a wide angle between transmitting and receiving antenna (e.g.



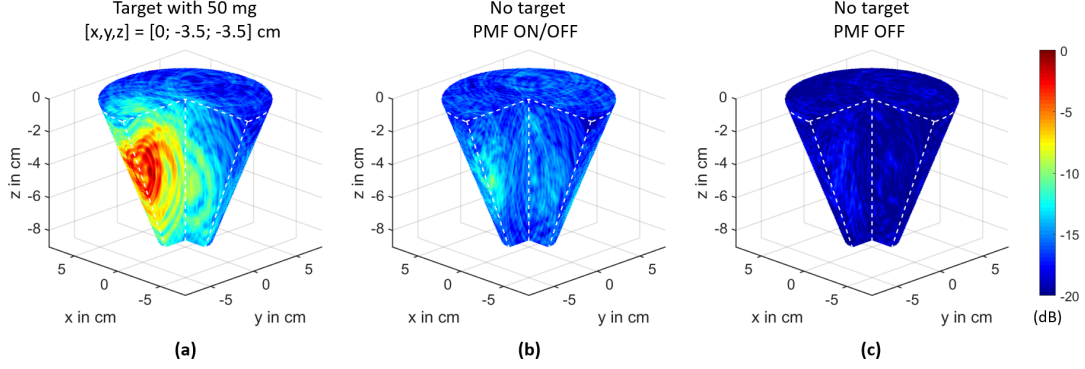


**Figure 5.13:** 3D UWB images based on differential measurements with  $\Delta y_{ch}(t, \Delta H_{m,n}) = \Delta \bar{y}_{ch,ON/OFF}(t, \Delta H_{m,0})$  (see Figure 5.4(c)) as DAS input signal; (a)  $I_{dB}(\mathbf{r}_0)$  for the scenario with a 2 mL target with 50 mg MNPs at the position  $[x,y,z]=[0;-3;-3.5]$  cm; (b)  $I_{dB,PMF}(\mathbf{r}_0)$  for the scenario without a target and with the presence of a PMF; (c)  $I_{dB,REF}(\mathbf{r}_0)$  for the scenario without a target and no presence of a PMF. The images are normalized to the maximum intensity of Subplot (a).

transmission channels) do not improve the imaging quality as described by Helbig et al. [2012b]. Figure 5.13 illustrates exemplarily the imaging results in dB corresponding to

$$I_{dB}(\mathbf{r}_0) = 10 \cdot \log_{10}(I^2(\mathbf{r}_0)) \quad (5.17)$$

for the ON/OFF measurements with a 2 mL target including 50 mg of MNPs (a) and without a target (b) as well as an image without a target and no presence of an external PMF (c). The scenario without a target and with the presence of a PMF shows differences compared to the image without a target and no presence of a PMF. These spurious effects are caused by interactions of the PMF with the measurement setup as described by Bucci et al. [2021] and also discussed in the following sections.

In order to evaluate the imaging results, the signal-to-clutter ratio is introduced as follows:

$$S/C = 10 \cdot \log_{10} \left( \frac{\frac{1}{V_{target}} \int_{V_{target}} I^2(\mathbf{r}_0) dV}{\frac{1}{V_{breast}} \int_{V_{breast}} I^2(\mathbf{r}_0) dV} \right) \quad (5.18)$$

where the numerator is the mean intensity of the target volume and the denominator is the mean intensity of the breast volume without the target region.

### 5.4.3 MNP Imaging Depending on the Target Position and the Penetration Depth

This section investigates the different aspects of MNP imaging corresponding to the setup presented in Section 5.4.1. First, the influence of the target's position on the MNP response

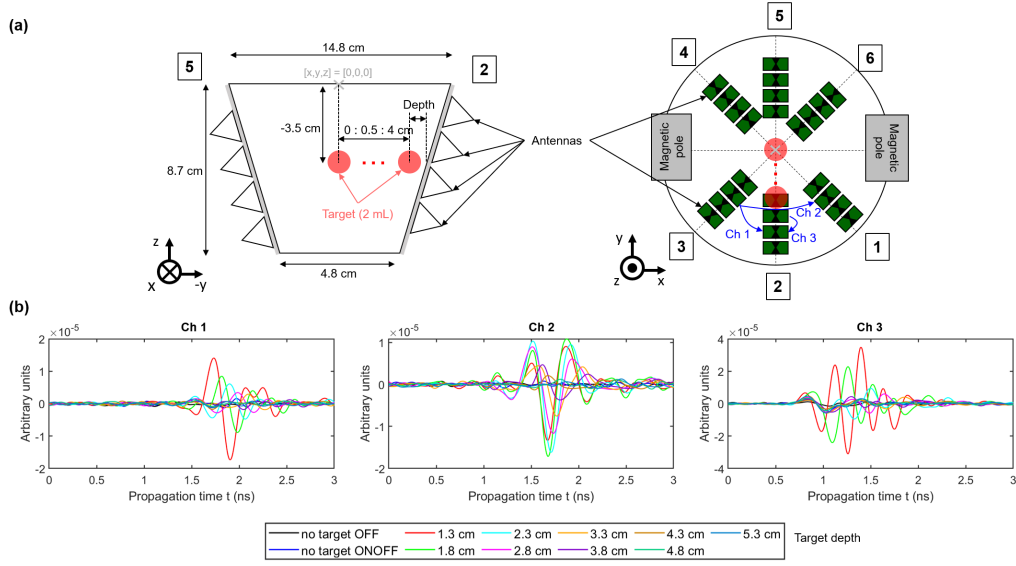


**Figure 5.14:** (a) Schematic of the measurement setup and the different target positions along the y-axis; (b) Differential IRFs for three different channels with the depth-dependent MNP response. The depth is related to the distance between the target and the wall of the examination mold.

is analyzed. Figure 5.14(a) illustrates the schematic of the measurement setup with the corresponding target positions. The target had a volume of 2 mL consisting of 10 % gelatin mixed with distilled water and 50 mg MNPs (WHKS 1S12, Liquids Research Limited, Bangor, UK). The MNP responses were measured at nine positions along the y-axis in steps of 5 mm as depicted in Figure 5.14(a). Furthermore, three channels with the MNP responses  $\Delta \bar{y}_{ONOFF}(t, \Delta H_{m,0})$  for different target depths are shown in Figure 5.14(b). The amplitude of the responses decreases with increasing depth for channel 1 and channel 3, whereby the latter one has the highest amplitude of all channels due to the short distance from the transmitting and receiving antenna to the target. However, the highest amplitude of channel 2 occurs at a target depth of 1.8 cm, which can be explained by the angle-dependent radiation pattern of the dipole antennas as investigated by Helbig et al. [2012a]. Figure 5.15 shows the 3D imaging results of the 2 mL target for the different target positions along the y-axis. The spurious effects that occur during a measurement with the presence of a PMF, as shown in Figure 5.13, are reduced by an image subtraction according to

$$I_{CF_{PMF}}(\mathbf{r}_0) = I(\mathbf{r}_0) - I_{PMF}(\mathbf{r}_0) \quad (5.19)$$

where  $I(\mathbf{r}_0)$  is the image with MNPs and  $I_{PMF}(\mathbf{r}_0)$  is a reference image without MNPs but with the presence of a PMF. Here,  $I_{PMF}$  represents a correction factor and a correction image, respectively, which includes the spurious effects of the PMF. Both im-



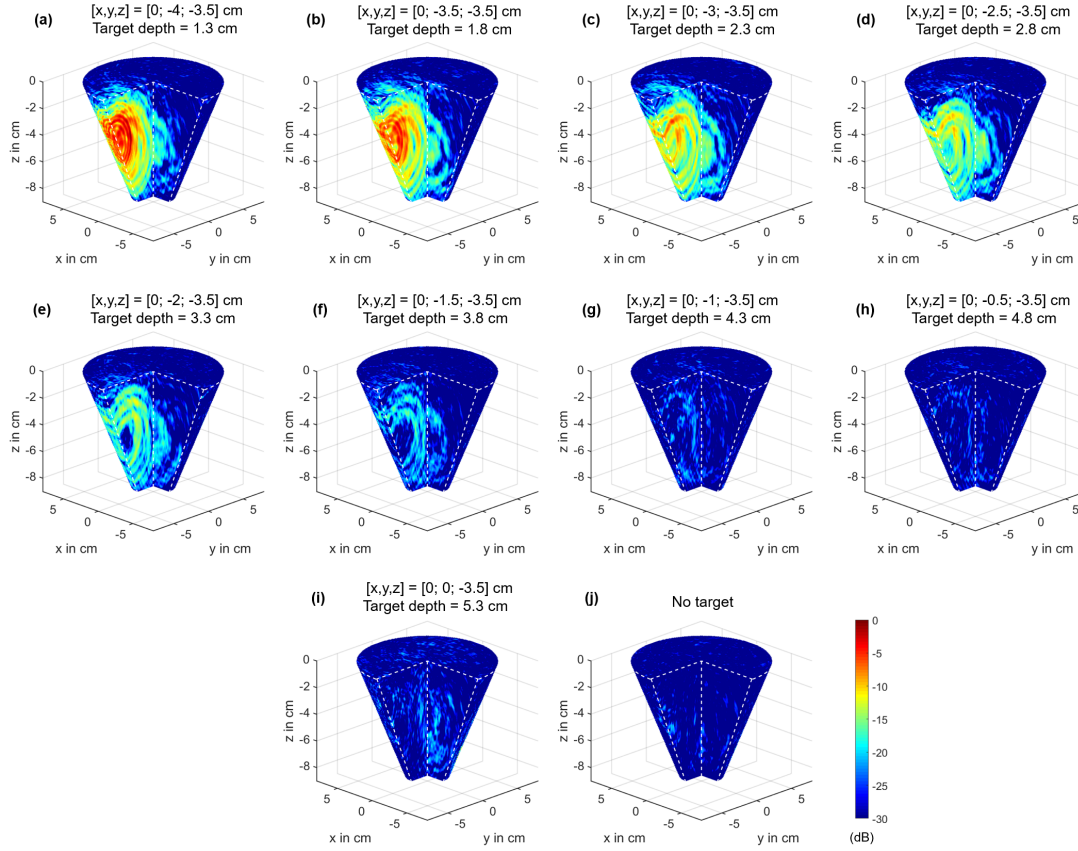


**Figure 5.15:** Imaging results of a 2 mL target with an MNP concentration of 25 mg/mL for different target positions along the y-axis. The images are computed corresponding to Equation 5.19 and presented in dB in accordance to Equation (5.17). The values are normalized to the maximum intensity of Subplot (a).

ages are computed by Equation (5.16) with the DAS input signal  $\Delta y_{ch}(t, \Delta H_{m,n}) = \Delta \bar{y}_{ch,ONOFF}(t, \Delta H_{m,0})$ . Figure 5.15 shows the PMF corrected images in dB corresponding to  $I_{CFPMF,dB}(\mathbf{r}_0) = 10 \cdot \log_{10}(I_{CFPMF}^2(\mathbf{r}_0))$ . The depth-dependent measurements are repeated for two additional axes as illustrated by the schematic in Figure 5.16(a). Furthermore, the  $S/C$  ratio is computed by Equation (5.18), replacing  $I$  with  $I_{CFPMF}$ , as a function of target depth in order to analyze the detectability of the MNPs (see Figure 5.16(b)). The  $S/C$  ratio decreases with increasing depth and shows the detection limit of the MNPs at a depth of approximately 4.3 cm. At higher distances, the  $S/C$  ratio is close to zero or less, indicating that the tumor does not rise above the clutter.

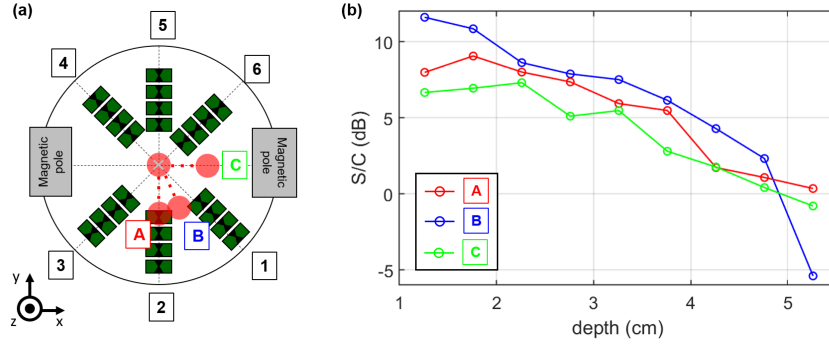


**Figure 5.16:** (a) Schematic of the antenna array and the target positions; (b) Corresponding signal-to-clutter ratio ( $S/C$ ) depending on the target depth for the three different axes A, B, C.

#### 5.4.4 Magnetic Field Influence

The results presented in Section 5.3.2 as well as given by Bellizzi et al. [2018], Ley et al. [2021] indicate a nonlinear behavior between the magnetic field intensity and the MNP response with respect to the working frequency range of the MWI system. In the case of an inhomogeneous magnetic field, the MNP response depends on the target position. The nonlinearity can be compensated by a correction factor derived from the investigations of Bellizzi et al. [2018]. Figure 5.17 illustrates the compensation approach, where the results of the magnetic field intensity measurements  $|H(\mathbf{r}_0)|$  (see Section 5.4.1) are shown exemplarily for one x-, y- and z-plane on the left-hand side. Furthermore, the differential magnetic susceptibility  $\Delta\chi_{m,n}(f, \Delta H_{m,n})$  as given by Bellizzi et al. [2018] is depicted (middle column). The knowledge of both parameters can be exploited to estimate a magnetic field intensity dependent normalization factor according to

$$\Delta M_{m,n} = \max |\Delta y_{\Delta\chi}(t, \Delta H_{m,n})| = \max \left| \int_{b_w} \Delta\chi_{m,n}(f, \Delta H_{m,n}) e^{j2\pi ft} df \right| \quad (5.20)$$

whereby  $b_w$  determines the working frequency range (1-4 GHz) and  $H_n = 0$  kA/m due to the ON/OFF measurement scenario. The differential magnetic susceptibility is computed by

$$\Delta\chi_{m,n}(f, \Delta H_{m,n}) = \chi(f, H_m) - \chi(f, H_n). \quad (5.21)$$

The data of  $\chi(f, H)$  for the MNPs under consideration are given by Bucci et al. [2017]. Figure 5.17 (middle) shows the results of the estimated differential signal  $\Delta y_{\Delta\chi}(t, \Delta H_{m,0})$  corresponding to Equation (5.20). The curves are normalized to the maximum value at  $\Delta H_{m,0} = 80$  kA/m. Please note that the focus is on the change of the magnetic properties,

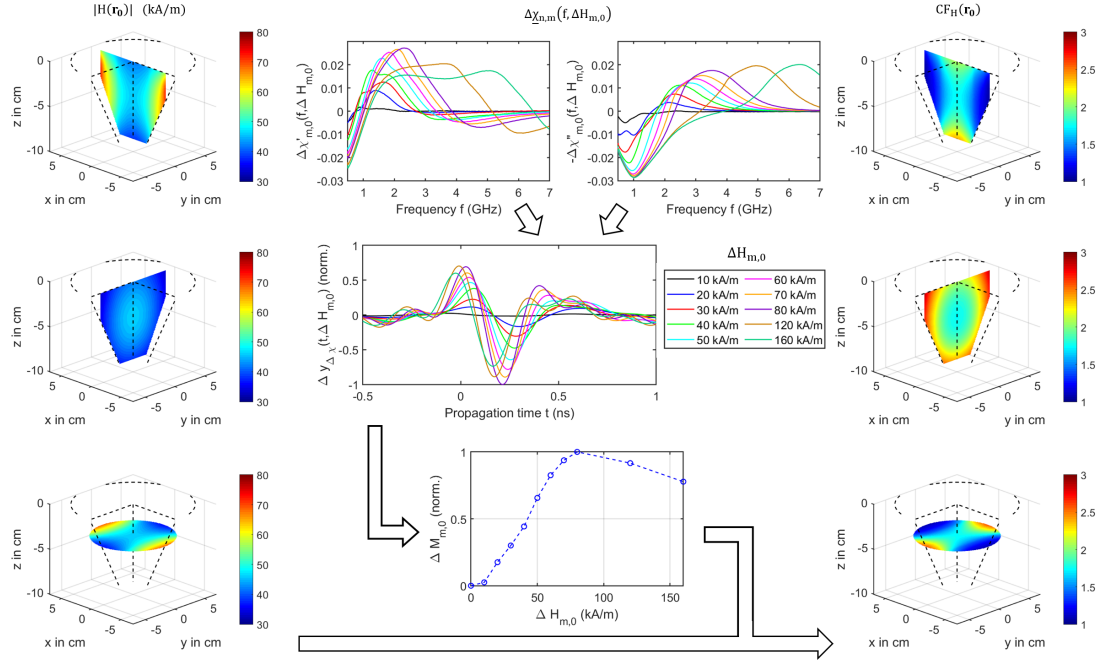


**Figure 5.17:** Compensation of the magnetic field inhomogeneity. Absolute value of the measured magnetic field intensity  $|H(\mathbf{r}_0)|$  (left column); Differential magnetic susceptibility  $\Delta\chi_{m,0}(f, \Delta H_{m,0})$  depending on the frequency for different magnetic field intensities according to Bellizzi et al. [2018], estimated differential signal  $\Delta y_{\Delta\chi}(t, \Delta H_{m,0})$  and the derived normalization curve as a function of  $\Delta H_{m,0}$  with  $b_w=1-4$  GHz scaled to its maximum at  $H_{m,0} = 80$  kA/m (middle column); 3D correction matrix  $CF_H(\mathbf{r}_0)$  computed by Equation (5.22) (right column).

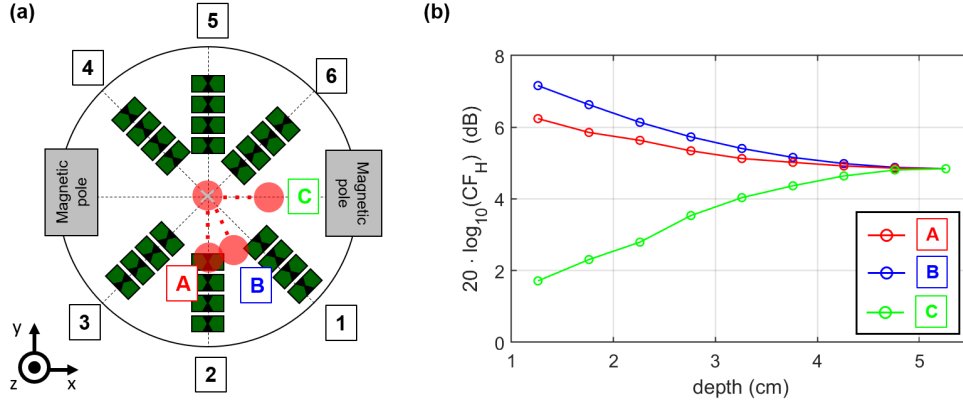


**Figure 5.18:** (a) Schematic of the antenna array and the target positions; (b) Correction factor  $20 \cdot \log_{10}(CF_H)$  in dB depending on the target position.

so in contrast to Bellizzi the normalization factor is independent of the channel-dependent path. Therefore, the transfer function of the MUT with respect to the dielectric properties

over the working frequency range is constant. In addition, Figure 5.17 (middle) depicts the absolute maximum of the estimated differential signal  $\Delta M_{m,n}$  as a function of the magnetic field intensity. Finally, the 3D correction matrix is computed by

$$CF_H(\mathbf{r}_0) = \frac{1}{\Delta M_{m,n}(\mathbf{r}_0)}, \quad \Delta M_{m,n} \neq 0 \quad (5.22)$$

whereby  $CF_H(\mathbf{r}_0)$  is the magnetic field dependent correction factor, which is illustrated on the right column in Figure 5.17 exemplarily for three different planes.

In order to analyze the effect of the correction approach, the correction factor is investigated at different target positions as shown in Figure 5.18. The correction factor  $CF_H$  shows the highest values along the A- and B-axes where the tumor is located close to the wall of the examination mold. This is in accordance with the magnetic field measurements, because the magnetic field intensities are low along these axes. The correction amplitude decreases with increasing depth towards the center of the mold. In contrast, the correction of the target along the C-axis shows the lowest values due to the high magnetic field intensity close to the magnetic pole. Here, the correction amplitude increases with growing distance between the target and the magnetic pole. In terms of MNP imaging, Equation (5.16) can be extended by the correction factor

$$\begin{aligned} I_{CF_H}(\mathbf{r}_0) &= CF_H(\mathbf{r}_0) \cdot \sum_{ch=1}^{N_{ch}} |\Delta y_{ch}(\tau_{ch}(\mathbf{r}_0), \Delta H_{m,n}(\mathbf{r}_0))| \\ &= CF_H(\mathbf{r}_0) \cdot I(\mathbf{r}_0) \end{aligned} \quad (5.23)$$

to compensate the inhomogeneity of the magnetic field distribution. Without taking the other influencing factors (e.g. path-dependent attenuation) into account, such a correction leads to the same intensity of an MNP-loaded target in the UWB image independent of its position and the magnetic field intensity distribution, respectively. Furthermore, the compensation approach can be combined with PMF correction introduced by Equation 5.19.

#### 5.4.5 MNP Imaging Depending on the PMF Modulation

In this section, two different types of PMF modulation and their influence on MNP detection and imaging are investigated. Compared to the ON/OFF modulation, a periodic PMF modulation offers the possibility to separate system drift effects (caused e.g. by weak temperature variations) and spurious effects (caused e.g. by interactions between the PMF and the imaging system) from the desired MNP response as shown by Ley et al. [2021]. Therefore, the MNP response for both modulation types is analyzed for a 2 mL target with an MNP concentration of 25 mg/mL, which was placed at the posi-

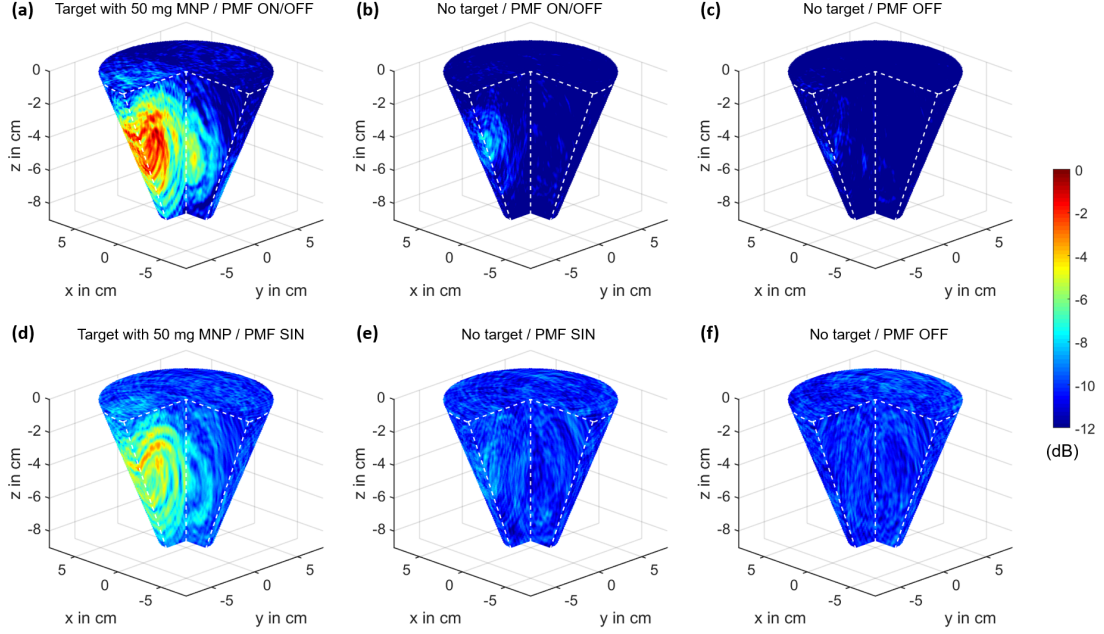


**Figure 5.19:** 3D UWB images based on ON/OFF and SIN modulation of the PMF as well as no presence of a PMF corresponding to Equations (5.16) and (5.17); DAS beam-forming with the DC component (a,b)  $|\Delta Y_{ch,ON/OFF}(t, \nu = 0 \text{ Hz}, \Delta H_{m,0})|$  and (c)  $|\Delta Y_{ch,OFF}(t, \nu = 0 \text{ Hz}, \Delta H_{0,0})|$  as input signal as well as the second harmonic (d,e)  $|\Delta Y_{ch,SIN}(t, \nu = 1 \text{ Hz}, \Delta H_{m,0})|$  and (f)  $|\Delta Y_{ch,OFF}(t, \nu = 1 \text{ Hz}, \Delta H_{0,0})|$  as input signal; (a,d) 2 mL target with a concentration of 25 mg/mL at position  $[x,y,z]=[0; -3; -3.5]$  cm; (b,e) ON/OFF and SIN modulation, respectively without a target; (c,f) no presence of a PMF and no target. The images are normalized to the maximum intensity of Subplot (a).

tion  $[x,y,z]=[0; -3; -3.5]$  cm. The magnetic field intensity at the target position is set to the same RMS value ( $H_{RMS} = 27 \text{ kA/m}$ ) for both modulations to ensure the comparability between both approaches. The sampling rate is approximately 6 IRFs per second and the 3D UWB images are calculated in dB according to Equations (5.16) and (5.17) with  $\Delta y_{ch}(t, \Delta H_{m,n}) = |\Delta Y_{ch,MOD}(t, \nu, \Delta H_{m,0})|$  for  $\nu = 0 \text{ Hz}$  or  $\nu = 1 \text{ Hz}$  as DAS input signal. Figure 5.19(a,d) shows the imaging results for the two-state modulation and the sinusoidal modulation of the PMF with the MNP-loaded target. In addition, the disruptive influence of the PMF on the imaging results is investigated for both types of modulation. Therefore, reference images without a target, but with the presence of the external PMF (see Figure 5.19(b,e)) and without the presence of an external PMF (see Figure 5.19(c,f)) are computed. The images with the MNP-loaded target clearly show the response caused by the modulated MNPs, with the ON/OFF modulation showing the highest intensity. However, the image of the ON/OFF modulation without a target shows different intensities compared to the corresponding image without the presence of a PMF, which indicates

**Table 5.1:**  $S/C$  ratios for ON/OFF and SIN modulation as well as for the scenario without the presence of an external PMF.

PMF	ON/OFF		SIN ( $\nu_{SIN} = 0.5$ Hz)		OFF
Target	50 mg (2 mL)	No target	50 mg (2 mL)	No target	No target
$\nu = 0$ Hz	5.7 dB	1.8 dB	4.9 dB	2.7 dB	0.9 dB
$\nu = 1$ Hz	-0.4 dB	-0.3 dB	3.4 dB	0.1 dB	0 dB

a slight disturbing influence of the PMF on the measurements. In contrast, the image with the SIN modulation without a target shows the same intensities compared to the corresponding image without the external PMF. Based on the images shown in Figure 5.19, the  $S/C$  ratio as introduced in Section 5.4.2 is calculated to compare both approaches. The results are summarized in Table 5.1. Considering the ON/OFF modulation it is obvious that the  $S/C$  ratio shows the highest value for the scenario with MNPs at the DC component (5.7 dB). However, it also indicates spurious effects of the PMF on the measurements, because the  $S/C$  ratios differ between the scenarios (no target) with and without the presence of the external PMF (1.8 dB resp. 0.9 dB). For the sake of completeness, the  $S/C$  ratios at the second harmonic are also computed. As expected, the ratios show low values (-0.4 dB resp. -0.3 dB), indicating no MNP response as well as no disturbing influences. Concerning the SIN modulation, the  $S/C$  ratio also shows the highest value for the scenario with MNPs at the DC component (4.9 dB), but a slight spurious influence is also present as shown by the difference in the  $S/C$  ratios between the SIN modulation without a target and the OFF measurement without a target (2.7 dB resp. 0.9 dB). In addition, the SIN modulation shows an MNP response at the second harmonic (3.4 dB). In contrast to the DC component analysis, the  $S/C$  ratios at this harmonic do not differ between the SIN modulation without a target and the OFF measurement without target (0.1 dB resp. 0 dB) providing an efficient detection of the desired MNP response at this frequency.

## 5.5 Discussion

This chapter presented different aspects of MNP detection and imaging by means of UWB pseudo-noise sensing. The experiments show that it is possible to detect weak permeability changes of MNPs induced by an external PMF. In the first experiments, the influence of the PMF on different amounts of MNPs diluted in distilled water was measured by means of M-sequence UWB technology. The results show a linear dependence between the measured MNP response and the magnetite mass, which is also confirmed by Bellizzi and Bucci

[2013]. In a modified test setup, the MNPs were embedded in a solid surrounding medium to suppress a movement of the MNPs into the direction of the magnetic field. In this case, only the MNP response related to the change of the magnetic properties was measured and the results also show a linear behavior between the MNP response and MNP mass.

In a second experiment the influence of the magnetic field intensity and the viscosity of different targets on the MNP response were analyzed. Bellizzi et al. [2018] figured out that there is a nonlinear dependence between the magnetic field intensity of the PMF and the MNP response with respect to the bandwidth of the UWB radar system. In addition, they determined the optimal magnetic field intensities of  $H_m = 80$  kA/m and  $H_n = 0$  kA/m in terms of the ON/OFF modulation based on the complex magnetic susceptibility of the MNPs dissolved in phosphate buffer saline. These findings are consistent with the results for the MNPs diluted in distilled water as shown in Figure 5.9. Moreover, the nonlinear dependence of the MNP response on magnetic field strength is valid even when the MNPs are embedded in a solid medium. All targets with MNPs show a similar curve shape with the maximum amplitude of the MNP response at approximately  $\Delta H_{m,0} = 80$  kA/m. However, the plots show differences in their amplitudes, which is confirmed by the results of a further experiment as depicted in Figure 5.10. While the targets with MNPs diluted in distilled water and embedded in agar show no significant differences as presented by Ley et al. [2020a, 2021], the targets with MNPs embedded in gelatin and oil-gelatin show a lower response as presented by Ley et al. [2021]. Embedding the MNPs in such a surrounding material leads to an immobilization of the particles, which means that the Brownian relaxation is suppressed. Since the Brownian relaxation influences the susceptibility in the lower frequency range as described in Section 2.5, this cannot be the reason for different amplitudes of the MNP responses. Rather, the dielectric properties of the targets influence the results, because the different complex permittivities of distilled water, agar, gelatin and oil-gelatin result in different reflection coefficients at the boundary between the MNP-loaded target and the surrounding medium as described in Section 5.1. A further aspect could be the low amount of n-propanol in the oil-gelatin targets corresponding to the mixtures presented by Lazebnik et al. [2005]. Mixing the MNPs with pure n-propanol results in a clumping of the particles. It might be possible that the low amount of n-propanol of the 0 % and 40 % oil-gelatin materials leads to small MNP clusters, which influence their susceptibility and lower the MNP response. In summary, immobilized MNPs can be detected by UWB sensing and the measured MNP response shows a linear dependence on magnetite mass. Both findings are crucial for MNP detection and imaging by means of UWB technology, since the MNPs are immobilized in tumor tissue as shown by the study of Dutz et al. [2011].

The second part of this chapter dealt with detecting and imaging of MNPs by means of an MWI system, which was implemented in recent years. The investigations are limited to phantom measurements, but the setup was developed with regard to a practical clinical use. In addition, the phantom materials were chosen with respect to the dielectric properties of biological tissue. Therefore, the tumor imitate consisted of 10 % gelatin, which is a more suitable substitute compared to distilled water due to its lower permittivity and due to the binding of the MNPs to gelatin in terms of their immobilization as demonstrated by Dutz et al. [2011].

Section 5.4.3 presented the results of the imaging procedure for a 2 mL tumor imitate with an MNP concentration of 25 mg/mL depending on the target position. Figure 5.15 shows that the intensity of the tumor decreases with increasing target depth, whereby it is still detectable at the depth of 4.3 cm as shown by the  $S/C$  ratio. At greater depths, the ratio approaches or falls below zero, indicating that the MNP response does not stand out from the clutter as depicted in Figure 5.16. The detectable depth is valid for the presented measurement scenario. Since the phantom materials were used with respect to the dielectric properties of biological tissue, it can be concluded that such amounts of MNPs can also be detected in *in vivo* measurements up to a depth of approximately 4 cm.

The imaging results are investigated for a tumor imitate with a constant volume and magnetite concentration at different positions and it is obvious that the  $S/C$  ratio depends on both the target depth and the investigated axes (A,B,C). These results offer some challenges related to MNP imaging, because the differences make it difficult to extract more information from the UWB images (e.g. amount of MNPs or the target size).

The main reason that the MNP response decreases with increasing target depth is the path-dependent attenuation of the electromagnetic wave, which is caused by the surrounding medium (cream). Furthermore, the antennas cannot be arranged uniformly due to the limited space at the magnetic poles. This results in an inhomogeneous illumination of the MUT by the antennas, which complicates the detection of the MNPs at certain locations, especially if they are close to the magnetic pole (e.g. see axis C in Figure 5.16(a)).

The MNP responses and the imaging results are also influenced by the inhomogeneity of the magnetic field. To compensate this influence, a correction factor was introduced. This factor is based on the magnetic field intensity in the air gap of the electromagnet measured by a gaussmeter (see Section 5.4.1) and the magnetic susceptibility of the MNPs as a function of the external magnetic field intensity in the microwave frequency range with the goal to image a target with the same intensity independently of the magnetic field distribution. Moreover, the derived correction factor can be combined with the imaging procedure as presented in Section 5.4.4.

Such a compensation only makes sense if an MNP response can be detected reliably.



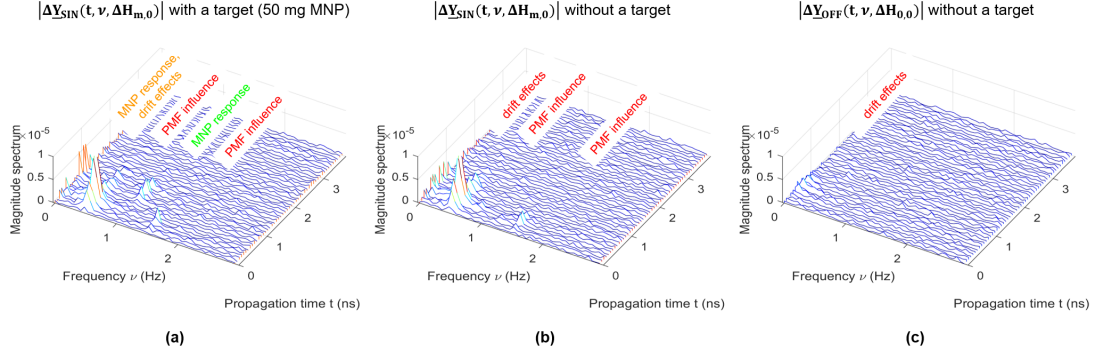


**Figure 5.20:** Fourier Transform over observation time of the clutter removed radargrams according to Equation (5.13) of one channel for different scenarios; (a) SIN modulation with the modulation frequency ( $\nu_{SIN} = 0.5$  Hz) and a 2 mL target with an MNP concentration of 25 mg/mL; (b) SIN modulation ( $\nu_{SIN} = 0.5$  Hz) without a target; (c) Without a target and no presence of an external PMF.

Considering a practical measurement scenario, the disruptive influence of the PMF on the MWI system has a negative effect on a robust MNP detection and imaging, respectively, as shown exemplarily in Figure 5.13. With regard to a reliable detection it is necessary to suppress or to separate the disruptive influence. Otherwise it becomes difficult to distinguish whether a change is caused by the spurious effects of the PMF or by the MNPs. Therefore, the disruptive influence in terms of the ON/OFF modulation is estimated by a differential imaging without MNPs, but with the presence of the PMF. In terms of a practical measurement scenario, a reference differential image has to be recorded before injecting the MNPs intravenously. Afterwards, the MNPs are injected and a second measurement is performed after a sufficient amount of MNPs have bound to the tumor. Since there are two UWB difference images (with and without MNPs), the disturbing influence of PMF should be comparable in both cases, even after the breast has been repositioned. Thus, the interfering influence can be reduced by subtracting both images according to Equation (5.19).

Due to the fact that differential imaging including breast repositioning will be affected by repositioning errors, a further promising approach is the periodic modulation of the PMF as described in Section 5.4.5. The sinusoidal modulation of the PMF enables a separation of the disturbing influence of the PMF from the MNP response. Figure 5.20(a) illustrates the different signal components in detail, showing the Fourier Transform of the clutter removed radargram in observation time corresponding to Equation (5.13) of one channel with an MNP-loaded target. The radargram has different signal components, whereby the MNP response corresponds to the second harmonic ( $\nu = 1$  Hz) and the DC component ( $\nu = 0$  Hz). However, the latter component is overlapped by a disturbing influence caused

by drift effects. This is evident due to the results of Figure 5.20(b,c), where a low signal component occurs at the DC value ( $\nu = 0$  Hz) even though there is no MNP-loaded target. Considering Figure 5.20(a) and Figure 5.20(b), the spurious effects occur at the modulation frequency ( $\nu_{SIN} = 0.5$  Hz) and at the third harmonic ( $\nu = 1.5$  Hz) in both scenarios, with and without a target. Bucci et al. [2021] investigated the spurious effects by means of different strip lines including typical components of an MWI system (e.g. sma connectors). They summarize that no detectable spurious harmonics arise from the PMF modulation (at least up to a magnetic field intensity of 80 kA/m) of the conduction currents due to the force exerted on the charge carriers by the PMF. However, all their experiments showed a harmonic in the spectrum of the measured scattering parameters at the modulation frequency of the PMF, possibly due to the interaction of the PMF with the inner electronics of the microwave measurement system. Moreover, the studies showed that the PMF exerts the strongest influence on the strip line with a sma connector, as can be deduced from the harmonics (1st - 3rd) that occur in the measured spectrum. For further details and explanations to their experiments, please refer to Bucci et al. [2021]. Finally, they figured out that spurious effects which occur at the second harmonic are associated with hidden magnetic materials in the measurement setup (see Bucci et al. [2018, 2021]). Since the cables and connectors in the measurement systems presented in Section 5.4.1 are nonmagnetic, such disturbing signal components are suppressed in the measurements as illustrated in Figure 5.20(b). In addition, Figure 5.20(c) shows the radargram without a target and no presence of a PMF where only minor drift effects occur in the low frequency range. These effects are related to weak and slow temperature variations of the measurement hardware and can be separated from the MNP response with a suitably high modulation frequency of the PMF. If the MNP response at the second harmonic is used as input signal for the imaging process, the difference between the reference measurement (no target and no PMF) and the PMF measurement (no target and SIN-modulation) will be quite low as illustrated in Figure 5.19(e,f) and confirmed by the  $S/C$  ratio as shown in Table 5.1. In this case, the MNPs can be detected reliably.

In comparison, the ON/OFF modulation shows higher intensities compared to the SIN modulation as depicted in Figure 5.19(a,d) and the PMF can be chosen with respect to the optimal magnetic field intensities of  $H_m = 80$  kA/m and  $H_n = 0$  kA/m. This means that lower amounts of MNPs can be detected with the ON/OFF modulation than with the SIN modulation. However, the two-state modulation exhibits a slight disruptive influence caused by the PMF, which can be also interpreted as MNP response (see Figure 5.19(b)). Therefore, an additional measurement (before MNP injection) is necessary in order to estimate this influence, which is not the case in terms of the sinusoidal modulation technique due to the separation of the different signal components.

In order to evaluate the detection results with respect to a clinical application, it is necessary to consider the possible amount of MNPs that can be delivered to the tumor by means of active targeting. Thereby, two factors must be considered. On the one hand the amount of MNPs that can be safely administered to a patient and on the other hand the delivery efficiency, i.e. the percentage amount of the injected dose of MNPs that reaches the tumor. Regarding the first aspect, commercially available MNPs are used for contrast enhancement in MRI, with allowable injection doses of 2.6 mg iron per kg body weight as described by Triantafyllou et al. [2013]. Based on this, Bucci et al. [2018] determined a potential MNP dose of approximately 250 mg for a 70 kg patient, assuming that iron accounts for approximately 70 % of the MNP (core) mass. The delivery efficiency depends on a variety of parameters and the results given by literature for *in vivo* measurements vary widely. Wilhelm et al. [2016] give a comprehensive overview based on 117 reports published between 2005 and 2015. They analyzed 232 data sets and calculated a mean delivery efficiency of 0.7 %, which means that 0.7 % of the administered nanoparticles are delivered to a tumor. With respect to active targeting of breast cancer, the upper quartile of the distribution of delivery efficiency spans the interval from 1.4 % to 4.5 % as described by Bucci et al. [2018]. Furthermore, they mentioned that it should be possible to deliver at least 3.5 mg of MNPs to a tumor of the size of a mouse model (8 mm in diameter).

Considering the MNP detection results presented in Section 5.3.1, such amounts are detectable by the differential approach presented in this work. Regarding MNP imaging (see Section 5.4), these small amounts still pose a challenge, especially for tumors at greater depths. However, Li et al. [2008] demonstrated that a delivery efficiency between 70 % and 80 % have been achieved by intravenous administration. If such an efficiency is realized in practice for active breast cancer targeting, it will be possible to detect small tumors at even greater depth, which is crucial in terms of contrast enhanced MWI for early breast cancer detection.

## 6 Summary

The aim of this thesis was to investigate two medical applications of UWB differential measurements. The first application is noninvasive temperature monitoring during thermal treatments (e.g. hyperthermia). This approach requires knowledge of the temperature-dependent dielectric properties of tissue in the microwave range. These properties were recorded using a measurement setup developed for this purpose. Based on these findings, it was investigated whether it is possible to detect temperature changes noninvasively using differential UWB pseudo-noise technology.

The second application is contrast enhanced microwave breast cancer detection and imaging using MNPs. For this purpose, various aspects and influences of MNP detection such as the mass dependence of MNPs, the influence of the viscosity of the MNP-loaded target, and the influence of the magnetic field intensity of the external PMF were investigated. Following these investigations, an MNP microwave imaging setup for contrast enhanced breast cancer detection was developed.

The first part of this thesis dealt with the noninvasive temperature monitoring. For this purpose a setup for accurate and reliable measurements of the temperature-dependent dielectric properties of tissue, tissue mimicking phantoms as well as liquids was implemented. In this context, evaluation measurements were performed to investigate different influences, e.g. storage time of the tissue, differences between heating and cooling of the samples, and the contact pressure between the tissue samples and the probe. Based on these findings, a reliable measurement procedure was derived. With this procedure, the temperature-dependent relative permittivity and effective conductivity of liver, muscle, fat, and blood were measured in the temperature range between 30 °C and 50 °C and in the frequency range from 0.5 GHz to 7 GHz. The measurements of the dielectric properties of liver, muscle and blood show a clear temperature dependence in the considered frequency range, which is fundamental for the detection of temperature changes in tissues by UWB sensing. The dielectric properties of blood show the highest temperature dependence, which means that a comparatively high sensitivity of the measured UWB signal can be expected due to the increased blood flow in the tumor tissue and the effective accumulation of heat. In contrast, fat shows a lower temperature dependence of the dielectric properties. Therefore, only slight differences are expected in the measured

radar signal during heating. The relative permittivity of liver, muscle and blood has the highest temperature dependence in the frequency range between 1-4 GHz. This range fits well with the -10 dB bandwidth of the currently applied active dipole antennas, which is in the range of 1-3 GHz as shown by Helbig et al. [2012a]. These results can be directly incorporated into future developments as well as in finding optimal system parameters of UWB microwave temperature monitoring systems.

Based on the DSP measurements, a temperature-dependent two-pole Cole-Cole model combined with a second order polynomial fit was derived to model the temperature-dependent dielectric properties of liver, muscle, fat and blood. The results of the fitting procedure agree well with the obtained data, as demonstrated by the small differences between the modeled and measured dielectric properties. The determined tissue-specific, temperature-dependent Cole-Cole models enable realistic numerical simulations of wave propagation in these tissues during hyperthermia treatments and are essential for the development of algorithms to estimate the tissue temperature based on measured UWB signals.

In order to prove the results of the temperature-dependent DSP measurements, an experimental measurement setup was developed to detect temperature changes of a target by means of UWB sensing. The results indicate that temperature changes of 1 °C cause detectable differential signals. Moreover, the results show a linear dependence of the amplitude of the signals on the temperature change of the target object. From this, an initial modeling approach for estimating temperature changes was postulated, which should be extended in future work.

In the second part of the thesis, various aspects of contrast enhanced microwave breast cancer detection and imaging by means of MNPs were investigated. In this context it was shown that the magnetic modulation of MNPs generates a diagnostically relevant differential signal, that is technically and clinically detectable by means of UWB pseudo-noise sensing. Further, the experimental measurements show that the amplitude of the MNP response signal is proportional to the amount of accumulated iron oxide and thus can provide information about the tumor size. In addition, the amplitude of the MNP signal also depends on the magnetic field intensity, which means that the optimal choice of the magnetic field strength with respect to the working frequency range of the UWB radar system increases the detectability of the MNPs. A further *in vitro* measurement showed that MNPs embedded in a solid medium can also be detected by the differential measurement approach. This becomes important regarding to a practical measurement scenario, where the MNPs are immobilized within the tumor.

Based on these findings, an MNP microwave imaging system was implemented. The

phantom materials were chosen with respect to the dielectric properties of tissue to obtain realistic conditions. The 3D imaging results show that the MWI system is able to image successfully a 2 mL target with an MNP concentration of 25 mg/mL up to a depth of 4.3 cm. To detect MNPs at greater depth, the contrast can be enhanced by increasing the magnetic field strength in the air gap up to the optimal magnetic field strength of 80 kA/m. In addition, a longer measurement time leads to a higher number of measured IRFs, which can be used to reduce noise due to averaging. Both methods (higher magnetic field strength and longer measurement time) lead to an increased heating of the electromagnet's coil. Therefore, appropriate measures must be taken to counteract this heating.

Furthermore, the magnetic field intensity distribution in the air gap was measured. Combined with the magnetic properties of the MNPs, the results were used to compensate the inhomogeneity of the magnetic field. In future work, the approach should be extended in terms of compensating the influence of dielectric properties (e.g. path-dependent attenuation) to obtain the MNP response of a target regardless of its position and the surrounding tissue.

The ON/OFF measurements indicated a slight disruptive influence of the external PMF on the MWI system. In order to reduce such an influence, two approaches were presented. In case of an ON/OFF modulation, the disturbing influence can be estimated by a differential measurement before contrast agent administration, with repositioning errors being taken into account. In addition to the ON/OFF modulation of the PMF, a sinusoidal modulation was applied, which indicated an efficient separation of both the spurious effects and the drift effects from the desired MNP response without the need for breast repositioning. In contrast to the sinusoidal PMF approach, the magnetic field intensities during ON/OFF modulation can be selected according to the optimal magnetic field intensities  $\Delta H_{m,n}$  and thus, the highest sensitivity can be expected with respect to MNP detectability.

Finally, both approaches are able to successfully image the MNPs in a realistic measurement setup. In terms of practical and clinical applications, further investigations are needed, in which both the spurious effects on the MWI system are minimized and the detectability of MNPs is improved to detect and image even smaller amounts of them.

# Bibliography

- R. M. Arthur, W. L. Straube, J. W. Trobaugh, and E. G. Moros. Non-invasive estimation of hyperthermia temperatures with ultrasound. *International Journal of Hyperthermia*, 21(6):589–600, 2005. doi: 10.1080/02656730500159103. URL <https://doi.org/10.1080/02656730500159103>. 22
- K. Arunachalam, P. R. Stauffer, P. F. Maccarini, S. Jacobsen, and F. Sterzer. Characterization of a digital microwave radiometry system for noninvasive thermometry using a temperature-controlled homogeneous test load. *Physics in Medicine and Biology*, 53(14):3883–3901, 2008. doi: 10.1088/0031-9155/53/14/011. URL <http://dx.doi.org/10.1088/0031-9155/53/14/011>. 22
- Y. Bao, T. Wen, A. C. S. Samia, A. Khandhar, and K. M. Krishnan. Magnetic nanoparticles: material engineering and emerging applications in lithography and biomedicine. *Journal of Materials Science*, 51(1):513–553, 2016. doi: 10.1007/s10853-015-9324-2. URL <https://doi.org/10.1007/s10853-015-9324-2>. 24
- G. Bellizzi and O. Bucci. A Novel Measurement Technique for the Broadband Characterization of Diluted Water Ferrofluids for Biomedical Applications. *Magnetics, IEEE Transactions on*, 49(6):2903–2912, 2013. URL [http://ieeexplore.ieee.org/xpls/abs\\_all.jsp?arnumber=6389778](http://ieeexplore.ieee.org/xpls/abs_all.jsp?arnumber=6389778). 16, 17, 79
- G. Bellizzi, O. M. Bucci, and I. Catapano. Microwave Cancer Imaging Exploiting Magnetic Nanoparticles as Contrast Agent. *IEEE Transactions on Biomedical Engineering*, 58(9):2528–2536, 2011. doi: 10.1109/TBME.2011.2158544. 25
- G. Bellizzi, G. G. Bellizzi, O. M. Bucci, L. Crocco, M. Helbig, S. Ley, and J. Sachs. Optimization of the Working Conditions for Magnetic Nanoparticle-Enhanced Microwave Diagnostics of Breast Cancer. *IEEE Transactions on Biomedical Engineering*, 65(7):1607–1616, 2018. ISSN 15582531. doi: 10.1109/TBME.2017.2753846. 2, 75, 76, 80
- M. Bertero, M. Miyakawa, P. Boccacci, F. Conte, K. Orikasa, and M. Furutani. Image restoration in chirp-pulse microwave CT (CP-MCT). *IEEE Transactions on Biomedical Engineering*, 47(5):690–699, 2000. ISSN 00189294. doi: 10.1109/10.841341. 23

- S. Brovoll, T. Berger, Y. Paichard, O. Aardal, T. S. Lande, and S. E. Hamran. Time-lapse imaging of human heart motion with switched array UWB radar. *IEEE Transactions on Biomedical Circuits and Systems*, 8(5):704–715, 2014. ISSN 19324545. doi: 10.1109/TBCAS.2014.2359995. 5
- O. M. Bucci, L. Crocco, and R. Scapaticci. On the Optimal Measurement Configuration for Magnetic Nanoparticles-Enhanced Breast Cancer Microwave Imaging. *IEEE Transactions on Biomedical Engineering*, 62(February 2015):407–414, 2014. 2, 25
- O. M. Bucci, G. Bellizzi, and G. G. Bellizzi. Microwave Broadband Characterization of a Diluted Water-Based Ferrofluid in Presence of a Polarizing Magnetic Field. *IEEE Transactions on Magnetics*, 53(3), 2017. ISSN 00189464. doi: 10.1109/TMAG.2016.2633239. 19, 20, 75
- O. M. Bucci, G. Bellizzi, S. Costanzo, L. Crocco, G. Di Massa, and R. Scapaticci. Assessing detection limits in magnetic nanoparticle enhanced microwave imaging. *IEEE Access*, 6 (August):43192–43202, 2018. ISSN 21693536. doi: 10.1109/ACCESS.2018.2861461. 25, 62, 83, 84
- O. M. Bucci, G. Bellizzi, S. Costanzo, L. Crocco, G. Di Massa, and R. Scapaticci. Experimental characterization of spurious signals in magnetic nanoparticles enhanced microwave imaging of cancer. *Sensors*, 21(8):1–19, 2021. ISSN 14248220. doi: 10.3390/s21082820. 25, 72, 83
- R. Campanile, E. Scardapane, A. Forente, C. Granata, R. Germano, R. Di Girolamo, A. Minopoli, R. Velotta, B. D. Ventura, and V. Iannotti. Core-shell magnetic nanoparticles for highly sensitive magnetoelastic immunosensor. *Nanomaterials*, 10(8):1–18, 2020. ISSN 20794991. doi: 10.3390/nano10081526. 24
- A. Casper, D. Liu, and E. S. Ebbini. Realtime control of multiple-focus phased array heating patterns based on noninvasive ultrasound thermography. *IEEE Transactions on Biomedical Engineering*, 59(1):95–105, 2012. ISSN 00189294. doi: 10.1109/TBME.2011.2162105. 22
- G. Chen, J. Stang, M. Haynes, E. Leuthardt, and M. Moghaddam. Real-Time Three-Dimensional Microwave Monitoring of Interstitial Thermal Therapy. *IEEE Transactions on Biomedical Engineering*, 65(3):528–538, 2018. ISSN 15582531. doi: 10.1109/TBME.2017.2702182. 23
- H.-W. Cheng, T. Hsin-Yi, C.-S. Chiang, and S.-Y. Chen. Magnetically Actuated Drug Delivery Helical Microrobot with Magnetic Nanoparticle Retrieval Ability. 13(17):19633–19647, 2021. 24



- W. T. Coffey, P. J. Cregg, and Y. U. P. Kalmykov. *On the Theory of Debye and Néel Relaxation of Single Domain Ferromagnetic Particles*. John Wiley & Sons, Inc, 1993a. ISBN 9780470141410. doi: 10.1002/9780470141410.ch5. 19
- W. T. Coffey, Y. P. Kalmykov, and E. S. Massawe. *The Effective Eigenvalue Method and Its Application to Stochastic Problems in Conjunction with the Nonlinear Langevin Equation*. John Wiley & Sons, Inc, 1993b. ISBN 0471575461. doi: 10.1002/9780470141441.ch10. 19
- L. Dubois. Temperature control and thermal dosimetry by microwave radiometry in hyperthermia. *IEEE Transactions on Microwave Theory and Techniques*, 44(10 PART 2): 1755–1761, 1996. ISSN 00189480. doi: 10.1109/22.539932. 22
- J. Dulińska-Litewka, A. Łazarczyk, P. Hałubiec, O. Szafrąński, K. Karnas, and A. Karewicz. Superparamagnetic Iron Oxide Nanoparticles—Current and Prospective Medical Applications. *Materials*, 12(4), 2019. doi: 10.3390/ma12040617. 24
- S. Dutz, M. Kettering, I. Hilger, and M. Robert. Magnetic multicore nanoparticles for hyperthermia — influence of particle immobilization in tumour tissue on. *Nanotechnology*, 22(26):265102 (7pp), 2011. doi: 10.1088/0957-4484/22/26/265102. 65, 80, 81
- W. J. Ellison. Permittivity of pure water, at standard atmospheric pressure, over the frequency range 0-25 THz and the temperature range 0-100 C. *Journal of Physical and Chemical Reference Data*, 36(1):1–18, 2007. ISSN 00472689. doi: 10.1063/1.2360986. 9, 45, 49, 52, 53
- P. C. Fannin. Magnetic spectroscopy as an aide in understanding magnetic fluids. *Journal of Magnetism and Magnetic Materials*, 252(1-3 SPEC. ISS.):59–64, 2002. ISSN 03048853. doi: 10.1016/S0304-8853(02)00600-5. 19
- P. C. Fannin, L. Kinsella, and S. W. Charles. On the influence of a uniform magnetic field on the Néel relaxation of a colloidal suspension of nanometre-sized particles. *Journal of Physics D: Applied Physics*, 30(16):2292–2297, 1997a. doi: 10.1088/0022-3727/30/16/006. URL <http://dx.doi.org/10.1088/0022-3727/30/16/006>. 16, 19
- P. C. Fannin, L. Kinsella, and S. W. Charles. The high-frequency complex susceptibility of ferrofluids deduced from fits to lower frequency measurements. *Journal of Physics D: Applied Physics*, 30(4):533–541, 1997b. ISSN 00223727. doi: 10.1088/0022-3727/30/4/006. 19
- P. C. Fannin, B. K. Scaife, A. T. Giannitsis, and S. W. Charles. Determination of the radius of nano-particles in a magnetic fluid by means of a constant frequency measure-

- ment technique. *Journal of Physics D: Applied Physics*, 35(12):1305–1310, 2002. ISSN 00223727. doi: 10.1088/0022-3727/35/12/304. 19
- P. C. Fannin, B. K. Scaife, A. T. Giannitsis, and C. Mac Oireachtaigh. High frequency ferromagnetic resonance measurements in magnetic fluids. *Journal of Magnetism and Magnetic Materials*, 289(January 2018):159–161, 2005. ISSN 03048853. doi: 10.1016/j.jmmm.2004.11.046. 19
- L. Farrugia, P. S. Wismayer, L. Z. Mangion, and C. V. Sammut. Accurate in vivo dielectric properties of liver from 500 MHz to 40 GHz and their correlation to ex vivo measurements. *Electromagnetic Biology and Medicine*, 35(4):365–373, 2016. ISSN 15368386. doi: 10.3109/15368378.2015.1120221. 13, 30
- E. C. Fear, X. Li, S. C. Hagness, and M. A. Stuchly. Confocal microwave imaging for breast cancer detection: Localization of tumors in three dimensions. *IEEE Transactions on Biomedical Engineering*, 49(8):812–822, 2002. ISSN 00189294. doi: 10.1109/TBME.2002.800759. 5, 12
- E. C. Fear, J. Bourqui, C. Curtis, D. Mew, B. Docktor, and C. Romano. Microwave breast imaging with a monostatic radar-based system: A study of application to patients. *IEEE Transactions on Microwave Theory and Techniques*, 61(5):2119–2128, 2013. ISSN 00189480. doi: 10.1109/TMTT.2013.2255884. 1
- T. V. Feddersen, J. A. Hernandez-Tamames, M. Franckena, G. C. van Rhoon, and M. M. Paulides. Clinical performance and future potential of magnetic resonance thermometry in hyperthermia, 2021. ISSN 20726694. 22
- O. Fiser. *Microwave Hyperthermia for Treatment of Head and Neck Tumors Controlled by Non-invasive Temperature Monitoring Based on UWB Radar*. PhD thesis, Czech Technical University in Prague, 2018. 23
- O. Fiser, I. Merunka, and J. Vrba. Waveguide applicator system for head and neck hyperthermia treatment. *Journal of Electrical Engineering and Technology*, 11(6):1744–1753, 2016. ISSN 20937423. doi: 10.5370/JEET.2016.11.6.1744. 23
- O. Fiser, M. Helbig, J. Sachs, S. Ley, I. Merunka, and J. Vrba. Microwave Non-invasive Temperature Monitoring Using UWB Radar for Cancer Treatment by Hyperthermia. *Progress In Electromagnetics Research*, 162:1–14, 2018. ISSN 15598985. 26
- J. Foiret and K. W. Ferrara. Spatial and Temporal Control of Hyperthermia Using Real Time Ultrasonic Thermal Strain Imaging with Motion Compensation, Phantom Study.

- PLOS ONE*, 10(8):e0134938, 2015. doi: 10.1371/journal.pone.0134938. URL <https://doi.org/10.1371/journal.pone.0134938>. 22
- A. Fornes-Leal, C. Garcia-Pardo, M. Frasson, V. Pons Beltrán, and N. Cardona. Dielectric characterization of healthy and malignant colon tissues in the 0.5-18 GHz frequency band. *Physics in Medicine and Biology*, 61(20):7334–7346, 2016. ISSN 13616560. doi: 10.1088/0031-9155/61/20/7334. 13
- K. R. Foster and H. P. Schwan. Dielectric Properties of Tissues. In C. Polk and P. Elliot, editors, *Biological Effects of Electromagnetic Fields*, chapter 1. CRC Press, 2 edition, 1996. 13, 14, 36
- C. Gabriel, S. Gabriel, and E. Corthout. The dielectric properties of biological tissues: I. Literature survey. *Physics in Medicine and Biology*, 41(11):2231–2249, 1996a. ISSN 00319155. doi: 10.1088/0031-9155/41/11/001. 13, 14
- S. Gabriel, R. W. Lau, and C. Gabriel. The dielectric properties of biological tissues: II. Measurements in the frequency range 10 Hz to 20 GHz. *Phys. Med. Biol. Phys. Med. Biol*, 41(41):2251–2269, 1996b. URL <http://iopscience.iop.org/article/10.1088/0031-9155/41/11/002/pdf>. 13
- S. Gabriel, R. W. Lau, and C. Gabriel. The dielectric properties of biological tissues: III. Parametric models for the dielectric spectrum of tissues. *Phys. Med. Biol.*, 41(41): 2251–2269, 1996c. URL <http://iopscience.iop.org/article/10.1088/0031-9155/41/11/002/pdf>. 13, 14, 15, 36, 37, 39, 40, 42, 43, 44, 45, 46, 53
- T. Gilbert. A Lagrangian Formulation of the Gyromagnetic Equation of the Magnetization Field. *Physical Review D*, 100:1243, 1955. 18
- B. Gleich and J. Weizenecker. Tomographic imaging using the nonlinear response of magnetic particles. *Nature*, 435(7046):1214–1217, 2005. doi: 10.1038/nature03808. URL <https://doi.org/10.1038/nature03808>. 25
- D. M. Hagl, D. Popovic, S. C. Hagness, J. H. Booske, and M. Okoniewski. Sensing volume of open-ended coaxial probes for dielectric characterization of breast tissue at microwave frequencies. *IEEE Transactions on Microwave Theory and Techniques*, 51(4 I):1194–1206, 2003. ISSN 00189480. doi: 10.1109/TMTT.2003.809626. 28
- M. Haynes, J. Stang, and M. Moghaddam. Real-time microwave imaging of differential temperature for thermal therapy monitoring. *IEEE Transactions on Biomedical Engineering*, 61(June):1787–1797, 2014. ISSN 15582531. doi: 10.1109/TBME.2014.2307072. 1, 23

- M. Helbig, K. Dahlke, I. Hilger, M. Kmec, and J. Sachs. Design and Test of an Imaging System for UWB Breast Cancer Detection. *Frequenz*, 66(11-12):387–394, 2012a. ISSN 2191-6349. doi: 10.1515/freq-2012-0103. URL <http://www.degruyter.com/view/j/freq.2012.66.issue-11-12/freq-2012-0103/freq-2012-0103.xml>. 1, 53, 73, 86
- M. Helbig, M. Kmec, J. Sachs, C. Geyer, I. Hilger, and G. Rinkus. Aspects of antenna array configuration for UWB breast imaging. *Proceedings of 6th European Conference on Antennas and Propagation, EuCAP 2012*, pages 1737–1741, 2012b. doi: 10.1109/EuCAP.2012.6206594. 72
- M. Helbig, J. H. Koch, S. Ley, R. Herrmann, M. Kmec, K. Schilling, and J. Sachs. Development and test of a massive MIMO system for fast medical UWB imaging. In *2017 International Conference on Electromagnetics in Advanced Applications (ICEAA)*, pages 1331–1334, 2017. 48
- I. Hilger. In vivo applications of magnetic nanoparticle hyperthermia. *International Journal of Hyperthermia*, 29(8):828–834, 2013. ISSN 14645157. doi: 10.3109/02656736.2013.832815. 1, 21
- I. Hilger, K. Dahlke, G. Rinkus, C. Geyer, F. Seifert, O. Kosch, F. Thiel, M. Hein, F. Scotto, U. Schwarz, M. Helbig, and J. Sachs. ultraMEDIS – Ultra-Wideband Sensing in Medicine. In *Ultra-wideband radio technologies for communications, localization and sensor applications*. 2013. 5
- F. Hoffmann. *Magnetic anisotropies of ( Ga , Mn ) As films and nanostructures*. PhD thesis, Universität Regensburg, 2010. 18
- F. Jaspard and M. Nadi. Dielectric properties of blood : an investigation of temperature dependence. *Physiological Measurement*, 23(3):547–554, 2002. URL <http://stacks.iop.org/0967-3334/23/i=3/a=306>. 15
- Y. Jin, C. Jia, S. W. Huang, M. O'Donnell, and X. Gao. Multifunctional nanoparticles as coupled contrast agents. *Nature Communications*, 1(4):1–8, 2010. ISSN 20411723. doi: 10.1038/ncomms1042. 24
- U. Kaatze. Complex permittivity of water as a function of frequency and temperature. *Journal of Chemical & Engineering Data*, 34(4):371–374, 1989. ISSN 0021-9568. doi: 10.1021/je00058a001. URL <http://pubs.acs.org/doi/abs/10.1021/je00058a001>. 9, 29, 45, 52, 53

- T. Kalla, A. Ringkamp, M. Seibel, and L. Wegert. Konzeption und Aufbau eines Messplatzes zur räumlichen Erfassung von Magnetfeldern für die medizinische UWB-Bildgebung. Technical report, Technische Universität Ilmenau, 2020. 71
- Ø. Klemetsen and S. Jacobsen. Improved Radiometric Performance Attained by an Elliptical Microwave Antenna With Suction. 59(1):263–271, 2012. 22
- M. Lazebnik, E. L. Madsen, G. R. Frank, and S. C. Hagness. Tissue-mimicking phantom materials for narrowband and ultrawideband microwave applications. *Physics in medicine and biology*, 50(18):4245–58, 2005. ISSN 0031-9155. doi: 10.1088/0031-9155/50/18/001. URL <http://www.ncbi.nlm.nih.gov/pubmed/16148391>. 63, 66, 67, 68, 80
- M. Lazebnik, M. C. Converse, J. H. Booske, and S. C. Hagness. Ultrawideband temperature-dependent dielectric properties of animal liver tissue in the microwave frequency range. *Phys Med Biol*, 51(7):1941–1955, 2006. doi: 10.1088/0031-9155/51/7/022. URL <https://www.ncbi.nlm.nih.gov/pubmed/16552116>. 15, 16, 30, 33, 37, 39, 40, 52
- M. Lazebnik, M. Okoniewski, J. H. Booske, and S. C. Hagness. Highly Accurate Debye Models for Normal and Malignant Breast Tissue Dielectric Properties at Microwave Frequencies. *IEEE Microwave and Wireless Components Letters*, 17(12):822–824, 2007a. doi: 10.1109/LMWC.2007.910465. 2, 13, 29
- M. Lazebnik, D. Popovic, L. McCartney, C. B. Watkins, M. J. Lindstrom, J. Harter, S. Sewall, T. Ogilvie, A. Magliocco, T. M. Breslin, W. Temple, D. Mew, J. H. Booske, M. Okoniewski, and S. C. Hagness. A large-scale study of the ultrawideband microwave dielectric properties of normal, benign and malignant breast tissues obtained from cancer surgeries. *Phys Med Biol*, 52(20):6093–6115, 2007b. doi: 10.1088/0031-9155/52/20/002. URL <https://www.ncbi.nlm.nih.gov/pubmed/17921574>. 58
- H. Lee, D. I. Kim, S. H. Kwon, and S. Park. Magnetically Actuated Drug Delivery Helical Microrobot with Magnetic Nanoparticle Retrieval Ability. *ACS Applied Materials and Interfaces*, 13(17):19633–19647, 2021. ISSN 19448252. doi: 10.1021/acsami.1c01742. 24
- S. Ley, M. Helbig, J. Sachs, S. Frick, and I. Hilger. First trials towards contrast enhanced microwave breast cancer detection by magnetic modulated nanoparticles. In *2015 9th European Conference on Antennas and Propagation (EuCAP)*, pages 1–4, 2015. ISBN 2164-3342. 3, 63
- S. Ley, M. Helbig, and J. Sachs. Contrast enhanced UWB microwave breast cancer detection by magnetic nanoparticles. In *2016 10th European Conference on Antennas and Propagation (EuCAP)*, pages 1–4, 2016. 4, 69

- S. Ley, J. Sachs, and M. Helbig. MNP enhanced microwave breast cancer imaging based on ultra-wideband pseudo-noise sensing. *2017 11th European Conference on Antennas and Propagation, EUCAP 2017*, pages 2754–2757, 2017. doi: 10.23919/EuCAP.2017.7928407. 4, 69
- S. Ley, O. Fiser, I. Merunka, J. Vrba, J. Sachs, and M. Helbig. Preliminary investigations for reliable temperature dependent UWB dielectric spectroscopy of tissues and tissue mimicking phantom materials. In *12th European Conference on Antennas and Propagation (EuCAP 2018)*, pages 1–5, 2018a. 3, 7
- S. Ley, O. Fiser, I. Merunka, J. Vrba, J. Sachs, and M. Helbig. Preliminary Investigations for Non-invasive Temperature Change Detection in Thermotherapy by Means of UWB Microwave Radar. *Proc. Annual International Conference of the IEEE Engineering in Medicine and Biology Society (EMBC)*, 2018:5386–5389, 2018b. ISSN 1557170X. doi: 10.1109/EMBC.2018.8513555. 1, 3, 26, 47, 48, 49, 53
- S. Ley, S. Schilling, O. Fiser, J. Vrba, J. Sachs, and M. Helbig. Ultra-Wideband Temperature Dependent Dielectric Spectroscopy of Porcine Tissue and Blood in the Microwave Frequency Range. *Sensors*, 19(7), 2019a. doi: 10.3390/s19071707. 3, 7, 27
- S. Ley, S. Schilling, O. Fiser, J. Vrba, J. Sachs, A. Prokhorova, and M. Helbig. Ultra-wideband temperature dependent dielectric spectroscopy of porcine muscle in the microwave frequency range. *Proceedings of European Microwave Conference in Central Europe, EuMCE 2019*, (EuCAP):554–557, 2019b. 3
- S. Ley, S. Schilling, O. Fiser, J. Vrba, J. Sachs, A. Prokhorova, and M. Helbig. Ultra-wideband temperature dependent dielectric spectroscopy of porcine muscle in the microwave frequency range. *Proceedings of European Microwave Conference in Central Europe, EuMCE 2019*, pages 554–557, 2019c. 3
- S. Ley, B. Faenger, I. Hilger, and M. Helbig. MNP Enhanced Microwave Imaging by Means of Pseudo-Noise Sensing with Different External Magnetic Field Modulations. *Proceedings of the Annual International Conference of the IEEE Engineering in Medicine and Biology Society, EMBS*, 2020-July:1795–1798, 2020a. ISSN 1557170X. doi: 10.1109/EMBC44109.2020.9175940. 4, 80
- S. Ley, B. Faenger, J. Sachs, I. Hilger, and M. Helbig. Investigation of Influences on the Detectability of Magnetic Nanoparticles by Means of Microwaves for Biomedical Applications. *14th European Conference on Antennas and Propagation, EuCAP 2020*, pages 1–4, 2020b. doi: 10.23919/EuCAP48036.2020.9135345. 3, 4, 65

- S. Ley, J. Sachs, B. Faenger, I. Hilger, and M. Helbig. MNP-Enhanced Microwave Medical Imaging by Means of Pseudo-Noise Sensing. *Sensors*, 21(19):1–23, 2021. doi: 10.3390/s21196613. URL <https://www.mdpi.com/1424-8220/21/19/6613>. 2, 4, 65, 69, 75, 77, 80
- S. D. Li, Y. C. Chen, M. J. Hackett, and L. Huang. Tumor-targeted delivery of siRNA by self-assembled nanoparticles. *Molecular Therapy*, 16(1):163–169, 2008. ISSN 15250024. doi: 10.1038/sj.mt.6300323. 84
- M. Liebl, F. Wiekhorst, D. Eberbeck, P. Radon, D. Gutkelch, D. Baumgarten, U. Steinhoff, and L. Trahms. Magnetorelaxometry procedures for quantitative imaging and characterization of magnetic nanoparticles in biomedical applications. *Biomedical Engineering / Biomedizinische Technik*, 60(5):427–443, 2015. doi: <https://doi.org/10.1515/bmt-2015-0055>. URL <https://www.degruyter.com/view/journals/bmte/60/5/article-p427.xml>. 25
- L. Lüdemann, W. Wlodarczyk, J. Nadobny, M. Weihrauch, J. Gellermann, and P. Wust. Non-invasive magnetic resonance thermography during regional hyperthermia. *International Journal of Hyperthermia*, 26(3):273–282, 2010. ISSN 14645157. doi: 10.3109/02656731003596242. 2, 21
- P. Ludewig, N. Gdaniec, J. Sedlacik, N. D. Forkert, P. Szwargulski, M. Graeser, G. Adam, M. G. Kaul, K. M. Krishnan, R. M. Ferguson, A. P. Khandhar, P. Walczak, J. Fiehler, G. Thomalla, C. Gerloff, T. Knopp, and T. Magnus. Magnetic Particle Imaging for Real-Time Perfusion Imaging in Acute Stroke. *ACS Nano*, 11(10):10480–10488, 2017. ISSN 1936086X. doi: 10.1021/acsnano.7b05784. 25
- F. J. Massey Jr. The Kolmogorov-Smirnov Test for Goodness of Fit. *Journal of the American Statistical Association*, 46(253):68–78, 1951. 67
- P. M. Meaney, T. Zhou, M. W. Fanning, S. D. Geimer, and K. D. Paulsen. Microwave thermal imaging of scanned focused ultrasound heating: Phantom results. *International Journal of Hyperthermia*, 24(7):523–536, 2008. ISSN 02656736. doi: 10.1080/02656730801944922. 1, 23
- P. M. Meaney, A. P. Gregory, J. Seppala, and T. Lahtinen. Open-Ended Coaxial Dielectric Probe Effective Penetration Depth Determination. *IEEE Transactions on Microwave Theory and Techniques*, 64(3):915–923, 2016. ISSN 00189480. doi: 10.1109/TMTT.2016.2519027. 28
- I. Merunka, A. Massa, D. Vrba, O. Fiser, M. Salucci, and J. Vrba. Microwave tomography system for methodical testing of human brain stroke detection approaches. *International*

- Journal of Antennas and Propagation*, 2019:9, 2019. ISSN 16875877. doi: 10.1155/2019/4074862. 1
- S. M. Michaelson and J. C. Lin. Radio and Microwave Dielectric Properties of Biological Materials. In S. M. Michaelson and J. C. Lin, editors, *Biological Effects and Health Implications of Radiofrequency Radiation*, chapter 4. Plenum Press, 1987. 13, 14
- M. Miyakawa. Tomographic measurement of temperature change in phantoms of the human body by chirp radar-type microwave computed tomography. *Medical & Biological Engineering & Computing*, 31:31–36, 1993. 23
- I. Neudecker. *Magnetization dynamics of confined ferromagnetic systems*. PhD thesis, Universität Regensburg, 2014. URL <http://epub.uni-regensburg.de/10440>. 17
- D. O’Loughlin, M. O’Halloran, B. M. Moloney, M. Glavin, E. Jones, and M. A. Elahi. Microwave breast imaging: Clinical advances and remaining challenges. *IEEE Transactions on Biomedical Engineering*, 65(11):2580–2590, 2018. ISSN 15582531. doi: 10.1109/TBME.2018.2809541. 1
- Q. A. Pankhurst, C. J. S. K. Jones, and J. Dobson. Applications of magnetic nanoparticles in biomedicine. *Journal of Physics D: Applied Physics*, 36(13):R167—R181, 2003. 24
- M. M. Paulides, J. F. Bakker, L. W. Hofstetter, W. C. Numan, R. Pellicer, E. W. Fiveland, M. Tarasek, G. C. Houston, G. C. Van Rhoon, D. T. Yeo, and G. Kotek. Laboratory prototype for experimental validation of MR-guided radiofrequency head and neck hyperthermia. *Physics in Medicine and Biology*, 59(9):2139–2154, 2014. ISSN 13616560. doi: 10.1088/0031-9155/59/9/2139. 1, 21
- R. Pethig and D. B. Kell. The passive electrical properties of biological systems: their significance in physiology. *Phys Med Biol*, 32(8):933–970, 1987. doi: 10.1002/prot.24544. 52
- A. Peyman, S. Holden, and C. Gabriel. Mobile Telecommunications and Health Research Programme: Dielectric Properties of Tissues at Microwave Frequencies. *Mobile Telecommunications and Health Research Programme*, 2005. URL [http://www.mthr.org.uk/research\\_projects/documents/Rum3FinalReport.pdf](http://www.mthr.org.uk/research_projects/documents/Rum3FinalReport.pdf). 30
- E. Porter, S. Salahuddin, A. La Gioia, M. A. Elahi, A. Shahzad, A. Kumar, D. Kilroy, and M. O’Halloran. Characterization of the Dielectric Properties of the Bladder Over the Microwave Range. *IEEE Journal of Electromagnetics, RF and Microwaves in Medicine and Biology*, 2(3):208–215, 2018. ISSN 2469-7249. doi: 10.1109/JERM.2018.2859584. URL <https://ieeexplore.ieee.org/document/8419244/>. 13



- A. W. Preece, I. Craddock, M. Shere, L. Jones, and H. L. Winton. MARIA M4: clinical evaluation of a prototype ultrawideband radar scanner for breast cancer detection. *Journal of Medical Imaging*, 3(3):033502, 2016. ISSN 1520510X. doi: 10.1021/ic50143a052. URL <http://medicalimaging.spiedigitallibrary.org/article.aspx?doi=10.1117/1.JMI.3.3.033502>. 1, 5
- A. Prokhorova, S. Ley, and M. Helbig. Quantitative interpretation of uwb radar images for non-invasive tissue temperature estimation during hyperthermia. *Diagnostics*, 11(5):16, 2021. ISSN 20754418. doi: 10.3390/diagnostics11050818. URL <https://www.mdpi.com/2075-4418/11/5/818>. 26
- V. Rieke and K. Butts Pauly. MR thermometry. *Journal of Magnetic Resonance Imaging*, 27(2):376–390, 2008. doi: 10.1002/jmri.21265. URL <https://doi.org/10.1002/jmri.21265>. 2, 22
- C. Rossmann and D. Haemmerich. Review of Temperature Dependence of Thermal Properties, Dielectric Properties, and Perfusion of Biological Tissues at Hyperthermic and Ablation Temperatures. *Critical Reviews in Biomedical Engineering*, 42(6):467–492, 2014. ISSN 0278-940X. doi: 10.1615/CritRevBiomedEng.2015012486. URL <http://www.dl.begellhouse.com/journals/4b27cbfc562e21b8,30efb37f17026d27,02f617f3357f0a4a.html>. 16
- J. Sachs. *Handbook of Ultra-Wideband Short-Range Sensing: Theory, Sensors, Applications*. Wiley-VCH Verlag GmbH & Co. KGaA, 2012. ISBN 9783527408535. doi: 10.1002/9783527651818. 5, 6, 7
- J. Sachs, P. Peyerl, S. Wöckel, M. Kmec, R. Herrmann, and R. Zetik. Liquid and moisture sensing by ultra-wideband pseudo-noise sequence signals. *Measurement Science and Technology*, 18(4):1074–1087, 2007. doi: 10.1088/0957-0233/18/4/016. URL <http://dx.doi.org/10.1088/0957-0233/18/4/016>. 7, 8
- J. Sachs, M. Helbig, R. Herrmann, and M. Kmec. Remote vital sign detection for rescue, security, and medical care by ultra-wideband pseudo-noise radar. *Ad Hoc Networks*, 13:42–53, 2014. URL <http://www.sciencedirect.com/science/article/pii/S1570870512001357>. 56
- J. Sachs, S. Ley, T. Just, S. Chamaani, and M. Helbig. Differential ultra-wideband microwave imaging: Principle application challenges. *Sensors (Switzerland)*, 18(7), 2018. ISSN 14248220. doi: 10.3390/s18072136. 5
- S. Salahuddin, M. O’Halloran, E. Porter, L. Farrugia, J. Bonello, C. V. Sammut, and P. S. Wismayer. Effects of standard coagulant agents on the dielectric properties of

- fresh human blood. *IEEE Transactions on Dielectrics and Electrical Insulation*, 24(5): 3283–3289, 2017. ISSN 10709878. doi: 10.1109/TDEI.2017.006582. 15
- R. Scapaticci, G. Bellizzi, I. Catapano, L. Crocco, and O. M. Bucci. An effective procedure for MNP-enhanced breast cancer microwave imaging. *IEEE transactions on bio-medical engineering*, 61(4):1071–9, 2014. ISSN 1558-2531. doi: 10.1109/TBME.2013.2293839. URL <http://www.ncbi.nlm.nih.gov/pubmed/24658232>. 1
- R. Scapaticci, G. G. Bellizzi, M. Cavagnaro, V. Lopresto, and L. Crocco. Exploiting Microwave Imaging Methods for Real-Time Monitoring of Thermal Ablation. *International Journal of Antennas and Propagation*, pages 1–13, 2017. ISSN 16875877. doi: 10.1155/2017/5231065. 1
- R. Scapaticci, J. Tobon, G. Bellizzi, F. Vipiana, and L. Crocco. Design and Numerical Characterization of a Low-Complexity Microwave Device for Brain Stroke Monitoring. *IEEE Transactions on Antennas and Propagation*, 66(12):7328–7338, 2018. ISSN 0018926X. doi: 10.1109/TAP.2018.2871266. 1
- E. Schena, D. Tosi, P. Saccomandi, E. Lewis, and T. Kim. Fiber optic sensors for temperature monitoring during thermal treatments: An overview. *Sensors (Switzerland)*, 16(7):1–20, 2016. ISSN 14248220. doi: 10.3390/s16071144. 1, 21
- P. Schier, M. Liebl, U. Steinhoff, M. Handler, F. Wiekhorst, and D. Baumgarten. Optimizing Excitation Coil Currents for Advanced Magnetorelaxometry Imaging. *Journal of Mathematical Imaging and Vision*, 62(2):238–252, 2020. doi: 10.1007/s10851-019-00934-8. URL <https://doi.org/10.1007/s10851-019-00934-8>. 25
- H. P. Schwan. Electrical properties of tissue and cell suspensions. *Advances in biological and medical physics*, 5:147–209, 1957. ISSN 00652245. doi: 10.1016/b978-1-4832-3111-2.50008-0. 13, 14
- J. Seo, S. K. Kim, Y.-s. Kim, K. Choi, D. G. Kong, and W.-c. Bang. Motion Compensation for Ultrasound Thermal Imaging Using Motion-Mapped Reference Model : An in vivo Mouse Study. *IEEE Transactions on Biomedical Engineering*, 61(11):2669–2678, 2014. 22
- G. V. Skrotskii and L. V. Kurbatov. Phenomenological Theory of Ferromagnetic Resonance. In *Ferromagnetic Resonance*, chapter II. Pergamon Press Ltd., 4 edition, 1966. 17, 18
- M. Triantafyllou, U. E. Studer, F. D. Birkhäuser, A. Fleischmann, L. J. Bains, G. Petralia, A. Christe, J. M. Froehlich, and H. C. Thoeny. Ultrasmall superparamagnetic particles

- of iron oxide allow for the detection of metastases in normal sized pelvic lymph nodes of patients with bladder and/or prostate cancer. *European Journal of Cancer*, 49(3): 616–624, 2013. ISSN 09598049. doi: 10.1016/j.ejca.2012.09.034. 84
- B. Vrbova and J. Vrba. Microwave thermotherapy in cancer treatment: evaluation of homogeneity of SAR distribution. 129:181–195, 2012. 1, 21
- J. Weizenecker, B. Gleich, J. Rahmer, H. Dahnke, and J. Borgert. Three-dimensional real-time in vivo magnetic particle imaging. *Physics in Medicine and Biology*, 54(5): L1–L10, 2009. doi: 10.1088/0031-9155/54/5/L01. URL <http://dx.doi.org/10.1088/0031-9155/54/5/L01>. 24
- J. Wells, D. Ortega, U. Steinhoff, S. Dutz, E. Garaio, O. Sandre, E. Natividad, M. M. Cruz, F. Brero, P. Southern, Q. A. Pankhurst, and S. Spassov. Challenges and recommendations for magnetic hyperthermia characterization measurements. *International Journal of Hyperthermia*, 38(1):447–460, 2021. ISSN 14645157. doi: 10.1080/02656736.2021.1892837. URL <https://doi.org/10.1080/02656736.2021.1892837>. 24
- F. Wiekhorst, U. Steinhoff, D. Eberbeck, and L. Trahms. Magnetorelaxometry Assisting Biomedical Applications of Magnetic Nanoparticles. *Pharmaceutical Research*, 29(5): 1189–1202, 2012. doi: 10.1007/s11095-011-0630-3. URL <https://doi.org/10.1007/s11095-011-0630-3>. 25
- S. Wilhelm, A. J. Tavares, Q. Dai, S. Ohta, J. Audet, H. F. Dvorak, and W. C. Chan. Analysis of nanoparticle delivery to tumours. *Nature Reviews Materials*, 1:1–12, 2016. ISSN 20588437. doi: 10.1038/natrevmats.2016.14. 84
- M. Wolf, R. Gulich, P. Lunkenheimer, and A. Loidl. Broadband dielectric spectroscopy on human blood. *Biochimica et Biophysica Acta - General Subjects*, 1810(8):727–740, 2011. ISSN 03044165. doi: 10.1016/j.bbagen.2011.05.012. 15, 45
- D. Wörtge, J. Moll, V. Krozer, B. Bazrafshan, F. Hübner, C. Park, and T. Vogl. Comparison of X-ray-Mammography and Planar UWB Microwave Imaging of the Breast: First Results from a Patient Study. *Diagnostics*, 8(3):1–8, 2018. ISSN 2075-4418. doi: 10.3390/diagnostics8030054. URL <http://www.mdpi.com/2075-4418/8/3/54>. 1
- X. L. Wu, X. Y. Zhang, X. G. Steinberg, X. H. Qu, X. S. Huang, X. M. Cheng, X. T. Bliss, X. F. Du, X. J. Rao, X. G. Song, X. L. Pisani, X. T. Doyle, X. S. Conolly, X. K. Krishnan, X. G. Grant, and X. M. Wintermark. A review of magnetic particle imaging and perspectives on neuroimaging. *American Journal of Neuroradiology*, 40(2):206–212, 2019. ISSN 1936959X. doi: 10.3174/ajnr.A5896. 25

- Y. Zhang, T. V. Samulski, W. T. Joines, J. Mattiello, R. L. Levin, and D. Lebihan. On the accuracy of noninvasive thermometry using molecular diffusion magnetic resonance imaging. *International Journal of Hyperthermia*, 8(2):263–274, 1992. ISSN 02656736. doi: 10.3109/02656739209021781. 21
- Y. Zhang, M. Ouyang, A. Ray, T. Liu, J. Kong, B. Bai, D. Kim, A. Guziak, Y. Luo, A. Feizi, K. Tsai, Z. Duan, X. Liu, D. Kim, C. Cheung, S. Yalcin, H. Ceylan Koydemir, O. B. Garner, D. Di Carlo, and A. Ozcan. Computational cytometer based on magnetically modulated coherent imaging and deep learning. *Light: Science and Applications*, 8(1): 1–15, 2019. ISSN 20477538. doi: 10.1038/s41377-019-0203-5. URL <http://dx.doi.org/10.1038/s41377-019-0203-5>. 24

# List of Figures

2.1	Example of a power spectrum of an UWB system . . . . .	5
2.2	Schematic diagram of the UWB M-sequence measurement . . . . .	6
2.3	Schematic diagram of the UWB M-sequence NWA . . . . .	7
2.4	Error model of a one-port measurement . . . . .	8
2.5	General scenario of microwave differential imaging . . . . .	10
2.6	Two-dimensional intensity plot via DAS beamforming . . . . .	12
2.7	Dielectric properties of muscle tissue with the three major dispersion regions	14
2.8	Relative permittivity and effective conductivity of various tissues in the microwave frequency range . . . . .	15
2.9	Temperature-dependent relative permittivity and effective conductivity of liver . . . . .	16
2.10	Néel rotation and Brownian rotation. . . . .	17
2.11	Precession of the magnetization around the effective magnetic field direction	18
2.12	Real part and opposite of the imaginary part of the magnetic susceptibility of iron oxide nanoparticles . . . . .	20
4.1	Principle of noninvasive temperature monitoring by means of UWB technology	26
4.2	Measurement setup for temperature-dependent UWB dielectric spectroscopy of tissues and blood . . . . .	28
4.3	Relative permittivity and effective conductivity of porcine liver, muscle, fat and blood for different storage times . . . . .	31
4.4	Relative permittivity and effective conductivity of porcine liver and blood at a constant temperature over a time period of 32 minutes . . . . .	32
4.5	Mean relative permittivity and mean effective conductivity of porcine liver during heating and cooling . . . . .	34
4.6	Mean relative permittivity and mean effective conductivity of porcine blood during heating and cooling . . . . .	35
4.7	Schematic of the fitting procedure . . . . .	36
4.8	Temperature-dependent Cole-Cole parameters of liver and the correspond- ing second order polynomial fit. . . . .	38

4.9	Relative permittivity and effective conductivity of porcine liver as a function of frequency at five different temperatures . . . . .	39
4.10	Difference between the measured data and the temperature-dependent two-pole Cole-Cole model of relative permittivity and effective conductivity of porcine liver. . . . .	40
4.11	Temperature-dependent Cole-Cole parameters of muscle and the corresponding second order polynomial fit. . . . .	41
4.12	Relative permittivity and effective conductivity of porcine muscle as a function of frequency at different temperatures. . . . .	42
4.13	Difference between the measured and the temperature-dependent two-pole Cole-Cole model of relative permittivity and effective conductivity of porcine muscle. . . . .	42
4.14	Temperature-dependent Cole-Cole parameters of fat and the corresponding second order polynomial fit . . . . .	43
4.15	Relative permittivity and effective conductivity of porcine fat as a function of frequency at different temperatures. . . . .	44
4.16	Difference between the measured data and the temperature-dependent two-pole Cole-Cole model of relative permittivity and effective conductivity of porcine fat. . . . .	44
4.17	Temperature-dependent Cole-Cole parameters of blood and the corresponding second order polynomial fit . . . . .	45
4.18	Relative permittivity and effective conductivity of porcine blood as a function of frequency at different temperatures . . . . .	46
4.19	Difference between the measured data and the temperature-dependent two-pole Cole-Cole model of relative permittivity and effective conductivity of porcine blood. . . . .	46
4.20	Measurement setup for temperature change detection by means of UWB pseudo-noise sensing . . . . .	47
4.21	Temperature change detection by means of UWB pseudo-noise sensing . . .	49
4.22	Temperature dependency of the differential reflection coefficient . . . . .	50
4.23	Temperature change validation . . . . .	51
4.24	Temperature-dependent model parameters of pure water . . . . .	52
5.1	Principle of contrast enhanced MWI and MNP detection . . . . .	56
5.2	Relative permittivity and relative dielectric loss of healthy and cancerous breast tissue . . . . .	58
5.3	Differential reflection coefficient as a function of frequency for various differential magnetic field intensities . . . . .	59

5.4	Clutter removal and signal processing for the ON/OFF modulation and the SIN modulation . . . . .	61
5.5	Experimental measurement setup for MNP detection depending on the MNP mass . . . . .	63
5.6	MNP responses depending on the MNP mass . . . . .	64
5.7	Experimental measurement setup for MNP detection depending on the MNP mass with a spherical target . . . . .	65
5.8	Experimental measurement setup for MNP detection depending on the viscosity and the magnetic field intensity of the PMF . . . . .	66
5.9	MNP responses depending on the viscosity and the magnetic field intensity of the PMF . . . . .	67
5.10	Results of the MNP response depending on the embedded medium . . . . .	68
5.11	UWB microwave MNP imaging setup . . . . .	69
5.12	Magnetic field measurement setup . . . . .	70
5.13	3D UWB images based on differential measurements . . . . .	72
5.14	Schematic of the UWB microwave MNP imaging setup with different target positions and differential IRFs of three channels . . . . .	73
5.15	MNP imaging results of a 2 mL target for different target depths . . . . .	74
5.16	Schematic of the antenna array with the different target positions and the corresponding $S/C$ ratio . . . . .	75
5.17	Compensation of the magnetic field inhomogeneity . . . . .	76
5.18	Correction factor $CF_H$ depending on the target position . . . . .	76
5.19	3D UWB images based on ON/OFF and SIN modulation . . . . .	78
5.20	PMF influence of SIN modulation on the MNP response . . . . .	82

# List of Tables

4.1	Tissue-dependent coefficients of the second order polynomial fit of liver. . .	39
4.2	Tissue-dependent coefficients of the second order polynomial fit of muscle. .	41
4.3	Tissue-dependent coefficients of the second order polynomial fit of fat. . .	43
4.4	Tissue-dependent coefficients of the second order polynomial fit of blood. .	45
5.1	$S/C$ ratios for ON/OFF and SIN modulation as well as for the scenario without the presence of an external PMF. . . . .	79



# List of Symbols, Operators and Abbreviations

## Symbols

$\underline{A}_m(f)$	Measured reference signal (incident wave)
$\underline{A}(f)$	Reference signal (incident wave)
$A(t, r_{pq})$	Path-dependent attenuation
$A_k$	Tissue-dependent coefficient of the second order polynomial fit
$a(t)$	Stimulus signal (M-sequence)
$B$	Magnetic field
$B_k$	Tissue-dependent coefficient of the second order polynomial fit
$B_x, B_y, B_z$	Magnetic field components
$\underline{B}(f)$	Receiving signal (reflected wave)
$\underline{B}_m(f)$	Measured receiving signal (reflected wave)
$b(t)$	Measured radar signal (uncorrelated)
$b_a$	Absolute bandwidth
$b_f$	Fractional bandwidth
$b_w$	Working frequency range
$C_{aa}(t)$	Autocorrelation of the stimulus signal $a(t)$
$C_{ab}(t)$	Cross-correlation of the stimulus signal (M-sequence) $a(t)$ and the measured signal $b(t)$
$CF_H(\mathbf{r}_0)$	Correction factor dependent on the magnetic field intensity
$C_k$	Tissue-dependent coefficient of the second order polynomial fit
$C_p$	Probe capacity
$c$	Propagation velocity of the electromagnetic wave in the medium
$ch$	Channel index
$\underline{E}_{11}, \underline{E}_{12},$ $\underline{E}_{21}, \underline{E}_{22}$	Error terms
$f$	Frequency
$f_A$	Sampling frequency

$f_c$	Sampling rate of the RF-clock
$f_l$	Lower cut-off frequency
$f_m$	Center frequency
$f_{res}$	Resonance frequency
$f_s$	Reduced sampling rate (after sub-sampling)
$f_u$	Upper cut-off frequency
$i$	Imaginary part
$g(t)$	Impulse response of the medium under test
$H, H_m, H_n$	External magnetic field intensity
$H_A$	Internal magnetic field
$H_{Ani}$	Anisotropy field
$H_{Demag}$	Demagnetizing field
$H_{eff}$	Effective magnetic field
$h$	Microwave driving field
$I(\mathbf{r}_0)$	UWB image (intensity of a pixel or voxel based on the absolute value of the input signal)
$I_0(\mathbf{r}_0)$	UWB image
$I_{CFPMF}(\mathbf{r}_0)$	PMF corrected UWB image (intensity of a pixel or voxel based on the absolute value of the input signal)
$I_{dB}(\mathbf{r}_0)$	UWB image in dB (intensity of a pixel or voxel based on the absolute value of the input signal)
$I_{PMF}(\mathbf{r}_0)$	UWB reference image containing the spurious effects caused by the PMF (intensity of a pixel or voxel based on the absolute value of the input signal)
$K_a$	Anisotropy factor
$k$	Index of the Tissue-dependent coefficients of the second order polynomial fit
$k_b$	Boltzmann constant
$N_{ch}$	Number of channels
$N_s$	Length of the M-sequence
$n$	Order of the Cole-Cole model
$n_s$	Order of the M-sequence
$M$	Magnetization
$M_s$	Saturation magnetization
$p$	Transmitting antenna index
$q$	Receiving antenna index
$R(t)$	Impulse response function of the receiving antenna

$r_{p,q}$	Distance from the transmitting antenna to the target and back to the receiving antenna
$\mathbf{r}_0$	Coordinates of the focal point
$S/C$	Signal-to-cutter ratio
$\underline{S}_{11}$	Corrected reflection coefficient
$\underline{S}_{11m}$	Measured reflection coefficient
$T$	Observation time (measurement time)
$T(t)$	Impulse response function of the transmitting antenna
$T_{OFF}$	Time period without the presence of an external polarizing magnetic field
$T_{ON}$	Time period with the presence of an external polarizing magnetic field
$t$	Propagation time
$t_R$	Propagation time corresponding to the expected magnetic nanoparticles response
$V_{breast}$	Volume of the breast
$V_h$	Hydrodynamic volume of a magnetic particle
$V_p$	Core volume of a magnetic particle
$V_{target}$	Volume of the target
$x$	Coordinate in Cartesian coordinate system
$x(t)$	Stimulus signal
$\underline{Y}_M$	Admittance (MATCH)
$\underline{Y}_O$	Admittance (OPEN)
$Y_P$	Probe admittance (LOAD)
$\underline{Y}_S$	Admittance (SHORT)
$Y_0(f)$	static components of the target response
$y$	Coordinate in Cartesian coordinate system
$y(t)$	Measured impulse response function (Cross-correlation of the stimulus signal (M-sequence) $a(t)$ and the measured signal $b(t)$ )
$y_{cl}(t)$	static clutter
$y_{tar}(t)$	target response
$y_0(t)$	static components of the target response
$\underline{Z}(f)$	Complex impedance of the medium under test
$Z_p$	Probe impedance
$z$	Coordinate in Cartesian coordinate system
$\alpha_n$	Distribution parameter describing the broadening of the dispersion corresponding to the n-th order of the Cole-Cole model
$\alpha_a, \alpha_d$	Dimensionless damping parameters

$\underline{\chi}(f)$	Complex susceptibility
$\underline{\chi}_{\perp}(f)$	Perpendicular (transversal) susceptibility
$\chi_{\perp 0}$	Static transverse susceptibility
$\underline{\chi}_{\parallel}(f)$	Parallel (longitudinal) susceptibility
$\chi_{\parallel 0}$	Static parallel susceptibility
$\Delta\varepsilon$	Dispersion amplitudes
$\Delta M_{m,n}$	Magnetic field intensity-dependent normalization factor
$\Delta\Gamma_H$	Differential magnetic field intensity-dependent reflection coefficient
$\Delta\Gamma_{\vartheta}$	Differential temperature-dependent reflection coefficient
$\Delta\Gamma_{\zeta}$	Differential contrast-dependent reflection coefficient
$\Delta\underline{Y}(f, \Delta\zeta_{1,2})$	Measured differential signal in frequency domain
$\Delta y(t, \Delta\zeta_{1,2})$	Measured differential signal in time domain
$\delta(t)$	Dirac delta
$\underline{\varepsilon}(f)$	Complex relative permittivity
$\varepsilon'$	Real part of the complex relative permittivity
$\varepsilon''$	Relative dielectric loss
$\underline{\varepsilon}_M$	Complex relative permittivity of the matching liquid (MATCH)
$\varepsilon_s$	Static permittivity
$\varepsilon_0$	Permittivity of free space
$\varepsilon_{\infty}$	Permittivity at high frequencies
$\Gamma_H$	Magnetic field intensity-dependent reflection coefficient
$\Gamma_{\vartheta}$	Temperature-dependent reflection coefficient
$\Gamma_{\zeta}$	Contrast-dependent reflection coefficient
$\gamma$	Gyromagnetic ratio
$\underline{\mu}(f)$	Complex relative permeability
$\mu_0$	Permeability constant in free space
$\nu$	Frequency due to the Fourier transform in observation time
$\nu_{SIN}$	Modulation frequency of the PMF
$\eta$	Effective viscosity
$\pi$	Mathematical constant $\pi \approx 3.14159$
$\sigma(f)$	Effective conductivity
$\sigma_E$	Ratio of anisotropy energy to thermal energy
$\sigma_s$	Static conductivity
$\tau$	Relaxation time
$\tau_B$	Brownian relaxation time
$\tau_{ch}(\mathbf{r}_0)$	Focal point-dependent time delay
$\tau_N$	Néel relaxation time

$\tau_n$	Relaxation times corresponding to the n-th order of the Cole-Cole model
$\tau_s$	Time shift
$\tau_0$	Characteristic time
$\tau_{02}$	Second effective relaxation time
$\tau_{\perp}$	Transverse magnetic relaxation time
$\tau_{\perp eff}$	Effective transverse magnetic relaxation time including the effects of Brownian relaxation
$\tau_{\parallel}$	Effective relaxation time
$\vartheta, \vartheta_m, \vartheta_n$	Absolute temperature
$\zeta$	Induced contrast

## Operators

$ \cdot $	Absolute value
$(\cdot)$	Complex value
$(\cdot)^*$	Conjugation
$\overline{(\cdot)}$	Mean value
$[\cdot]^{-1}$	Inverse of a matrix
$*$	Convolution
$\det$	Determinant
$\mathcal{F}\{\cdot\}$	Fourier Transform

## Abbreviations

2D	Two-dimensional
3D	Three-dimensional
ADC	Analog-to-digital converter
DAS	Delay-and-sum
dB	Decibels
DC	Direct current
DSP	Dielectric spectroscopy
FFP	Field free point in space
IRF	Impulse response function
MIMO	Multiple-in and multiple-out
MNPs	Magnetic nanoparticles
MPI	Magnetic particle imaging
MRI	Magnetic resonance imaging

MRT	Magnetic resonance thermometry
MRX	Magnetorelaxometry
MUT	Medium under test
MWI	Microwave imaging
NWA	Network analyzer
OG	Oil-gelatin
OSM	OPEN, SHORT, MATCH
PMF	Polarizing magnetic field
Rx	Receiving port
T1	Spin-lattice relaxation time
T2	Spin-spin relaxation time
Tx	Transmitting port
SPIONs	Superparamagnetic iron oxide nanoparticles
UWB	Ultra-wideband

# Erklärung

Ich versichere, dass ich die vorliegende Arbeit ohne unzulässige Hilfe Dritter und ohne Benutzung anderer als der angegebenen Hilfsmittel angefertigt habe. Die aus anderen Quellen direkt oder indirekt übernommenen Daten und Konzepte sind unter Angabe der Quelle gekennzeichnet. Bei der Auswahl und Auswertung des folgenden Materials haben mir die nachstehend aufgeführten Personen in der jeweils beschriebenen Weise unentgeltlich geholfen:

1. *Unterstützung bei der Interpretation der Ergebnisse in der gesamten Arbeit:*

Dr.-Ing. Marko Helbig, Technische Universität Ilmenau, Fakultät für Informatik und Automatisierung, Deutschland

2. *Unterstützung bei der Fertigung des Elektromagneten für den Messaufbau zur MNP Bildgebung:*

Achim Danner, Technische Universität Ilmenau, Fakultät für Elektrotechnik und Informationstechnik

Dr.-Ing. Marko Helbig, Technische Universität Ilmenau, Fakultät für Informatik und Automatisierung, Deutschland

Weitere Personen waren an der inhaltlich-materiellen Erstellung der vorliegenden Arbeit nicht beteiligt. Insbesondere habe ich hierfür nicht die entgeltliche Hilfe von Vermittlungs- bzw. Beratungsdiensten (Promotionsberater oder anderer Personen) in Anspruch genommen. Niemand hat von mir unmittelbar oder mittelbar geldwerte Leistungen für die Arbeiten erhalten, die in Zusammenhang mit dem Inhalt der vorgelegten Dissertation stehen.

Die Arbeit wurde bisher weder im In- noch im Ausland in gleicher oder ähnlicher Form einer Prüfungsbehörde vorgelegt.

Ich bin darauf hingewiesen worden, dass die Unrichtigkeit der vorstehenden Erklärung als Täuschungsversuch bewertet wird und gemäß §7 Abs. 10 der Promotionsordnung den Abbruch des Promotionsverfahrens zur Folge hat.

Ilmenau, 19. April 2022

Sebastian Ley